Universiteit
Leiden
The Netherlands

The innate immune response against mycobacterial infection : analysis by a combination of light and electron microscopy

Hosseini, R.

Citation
Hosseini, R. (2015, October 20). *The innate immune response against mycobacterial infection : analysis by a combination of light and electron microscopy*. Retrieved from https://hdl.handle.net/1887/35954

Version:	Not Applicable (or Unknown)
License:	Licence agreement concerning inclusion of doctoral thesis in the Institutional Repository of the University of Leiden
Downloaded from:	https://hdl.handle.net/1887/35954

Note: To cite this publication please use the final published version (if applicable).

Cover Page

Universiteit Leiden

The handle http://hdl.handle.net/1887/35954 holds various files of this Leiden University dissertation.

Author: Hosseini, Rohola
Title: The innate immune response against mycobacterial infection : analysis by a combination of light and electron microscopy
Issue Date: 2015-10-20

The innate immune response against mycobacterial infection

Analysis by a combination of light and electron microscopy

Rohola Hosseini

© Rohola Hosseini

Cover, layout design: Rohola Hosseini

Printing of this thesis was supported by the Nederlandse Vereniging voor Microscopie.

Printed by Wohrmann Print Services

ISBN:978-94-6203-936-0

The innate immune response against mycobacterial infection

Analysis by a combination of light and electron microscopy

Proefschrift

ter verkrijging van
de graad van Doctor aan de Universiteit Leiden,
op gezag van Rector Magnificus prof.mr. C.J.J.M. Stolker,
volgens besluit van het College voor Promoties
te verdedigen op dinsdag 20 oktober
klokke 16:15 uur

door

Rohola Hosseini
geboren te Qandahar, Afghanistan
in 1983

Promotoren:	Prof. Dr. H.P. Spaink
	Prof. Dr. P.C.W. Hogendoorn
Copromotor:	Dr. M.J.M. Schaaf
Promotiecommisie:	Prof. Dr. A.H. Meijer
	Prof. Dr. G.P. van Wezel
	Prof. Dr. J.H. de Winde
	Prof. Dr. Ir. A. J. Koster
	Prof. Dr. G. W. Griffiths

Voor mijn ouders

Contents

Chapter 1 General introduction and outline of the thesis 9

Chapter 2 Correlative light and electron microscopy imaging of autophagy in a zebrafish infection model 25

Chapter 3 Dynamic interaction between leukocytes determines the progression of infection during early mycobacterial pathogenesis 55

Chapter 4 Ultrastructural analysis of the effect of Myd88 deficiency on granuloma development during Mycobacterium marinum infection 83

Chapter 5 Summary and Discussion 101

Appendix Samenvatting 115

Curriculum vitae 121

List of publications 123

CHAPTER 1

GENERAL INTRODUCTION AND OUTLINE OF THE THESIS

Pulmonary tuberculosis

Pulmonary tuberculosis (TB) is a bacterial infection caused by *Mycobacterium tuberculosis* that in humans commonly enters the lung and preferably resides there inside cells of the host. In most cases the infection remains in the lungs or in the local lymphatics (primary complex). Alternatively, it can also disseminate via lymphatics and blood vessels to other organs (military tuberculosis). The pathogen is spread to other individuals by droplets through the air, when people who have an active TB infection cough, sneeze, or otherwise transmit respiratory fluids. Upon infection often no symptoms are observed, and this condition is known as latent tuberculosis. It is estimated that one third of the world population has a latent TB infection, that progresses to active TB in 5-10% of cases. TB has been responsible for a high mortality in human populations and is still a major health issue in the third world. Since the late 19th century, mortality rates declined in Europe and the United States. However, worldwide new cases of TB are diagnosed every second and one TB patient does not survive the infection every 20 seconds (WHO, 2013: http://www.who.int/tb/publications/en/).

During *Mtb* infection, the bacterium is taken up by host phagocytes that are present in the lung and it replicates within these cells (Eum et al., 2010; Repasy et al., 2013). As infection progresses, macrophages and other immune cell types are recruited to sites of infection, creating a structured aggregate of infected and uninfected cells which is called a granuloma (Philips and Ernst, 2012; Berg and Ramakrishnan, 2012). These granulomas consist of a tightly interdigitated inner core of macrophages termed 'epithelioid' macrophages, surrounded by additional immune cells, including T-cells, B-cells, dendritic cells and neutrophils (Philips and Ernst, 2012; Berg and Ramakrishnan, 2012; Ramakrishnan, 2012). The granuloma is the hallmark structure of tuberculosis and constitutes a crucial niche in which bacteria persist. Eventual rupture of granulomas is crucial for bacterial release into the lung and transmission of the disease to other individuals.

Mtb is believed to have existed for more than 70.000 years and seems to have co-evolved together with humans before the migration out of Africa (Comas et al., 2013). This indicates that *Mtb* had considerable time and opportunity to develop mechanisms for the manipulation of its host's immune response. *Mtb* caused more deaths in industrialized countries than any other disease during the 19th century. At that time, the majority of the urban populations of Europe and North America were infected with *Mtb*, and ~80% of patients who developed active TB did not survive this infection (Harvard University Library, open collections: http://ocp.hul.harvard.edu/contagion/tuberculosis.html).

Nowadays, TB is a major risk for immunosuppressed individuals like HIV-infected people and patients using TNF-alpha inhibitors or immunosuppressive

drugs. Although effective therapies declined the incidence of TB in recent years, the increase of drug-resistant forms of TB are of concern and several problems regarding the clinical treatment of TB still exist. The first successful antibiotic, streptomycin (purified from *Streptomyces griseus*), became available in the 1940s. It restricted *Mtb* growth in humans, but although the effects of this drug were astonishing at the start, within a few months resistant mutant strains began to appear. The last decades the intensive use of antibiotics and inefficient drug treatment have increased the occurrence of multi-drug resistant *Mtb* strains (Ottenhof, 2012). Currently, combinations of antibiotics are used and efficient therapy requires intensive long-term (over 6 months) treatment. In addition, the widely used TB vaccine is an attenuated strain of *Mycobacterium bovis*, bacillus Calmette–Guérin (BCG), which is highly effective against disseminated TB in children but has a low efficiency in adult populations (Ottenhoff and Kaufmann, 2012). Finally, in areas and countries with a poorly developed healthcare system, access to treatment remains challenging (Lienhardt et al., 2012). The desired development of novel therapeutic strategies requires a better understanding of the host-pathogen interactions during *Mtb* pathogenesis (Goldberg et.al., 2012; Ottenhoff, 2012).

Phagocytic cells and mycobacterial infection

The cells comprising our immune system are equipped with a large set of pattern recognition receptors (PRRs), including Toll-like receptors (TLRs), NOD like receptors, mannose receptors and complement receptors. For example, macrophages use PRRs to recognize invading pathogens by pathogen-associated molecular patterns (PAMPs) on the surface of bacteria. Subsequently, the bacteria are internalized using one PRR or a combination of PRRs and an appropriate immune response is initiated dependent on the type of receptors that have recognized the pathogen (Medzhitov and Janeway, 2000; Kawai and Akira, 2005).

Toll-like receptors (TLR), especially TLR4 are associated with recognition of mycobacteria and play an important role in mycobacterial infection (Tjärnlund et al., 2006; Corr and O'Neill, 2009). Along with the recognition of pathogens, these receptors initiate a signalling cascade through several intracellular adaptor molecules, including Myeloid differentiation factor 88 (MyD88), to induce intracellular effectors and the initiation of an inflammatory response (Medzhitov and Janeway, 2000; van der Vaart et al., 2013). MyD88 is a key adaptor protein in the TLR signalling pathway since it is used by all TLRs (except TLR3) to initiate an inflammatory response (Takeda and Akira, 2004). The C-terminal part of MyD88 consists of a toll/interleukin-1 receptor (TIR) homology domain that enables interaction with TLRs. Its N-terminal death domain enables formation of a 'Myddosome' signalling complex. This complex consisting of interleukin-1 receptor

associated kinases (IRAK) plays a central role in inflammation and the host defense by activating nuclear factor κB (NF-κB) and mitogen-activated protein kinase (MAPK) signalling (Lin et al., 2010; Gay et al., 2011). The TLR and MyD88 signalling pathways are well conserved between human and the zebrafish (van der Sar et al., 2006).

Once macrophages have ingested mycobacteria, they encapsulate the bacteria in phagosomes and activate an array of intracellular effector mechanisms. These mechanisms are aimed at elimination of bacteria inside the phagosomes or upon fusion with lysosomes, and include acidification of compartments, and production of oxidants, nitrosylating agents, antimicrobials and proteases (MacMicking, 2014; Torraca et al., 2014). In response to the capability of the host cells to eliminate bacteria, pathogenic mycobacteria have evolved mechanisms for the manipulation of its host's immune response by secretion of virulence factors via specialized secretion systems (Baxt et al., 2013; Houben et al., 2014). They are able to prevent lysosomal fusion and acidification of phagosomal compartments (Armstrong and Hart, 1971; Tan and Russell, 2015). While a fraction of *Mtb* within a host cell is kept inside phagosomes, another fraction is able to escape from the phagosomes into the cytoplasm (van der Wel et al., 2007; Simeone et al., 2015).

Mtb has been shown to be sensitive to low pH, resulting in growth arrest at pH 5.0 and lower (Chapman and Bernard, 1962; Tan et al., 2010). Therefore lysosomal fusion with phagosomes has always been considered to be the sole mechanism in the host defence against mycobacterial pathogenesis. However, recent studies demonstrate additional mechanisms restricting mycobacterial proliferation. These include phagocytosis of dead cells containing pathogens (a process called efferocytosis), antimicrobial peptides as a part of the autophagic response and sequestration by autophagic vacuoles of escaped bacteria in the cytoplasm (Mostowy, 2013; Deretic, 2012; Weiss and Schaible, 2015).

Another classical view concerning the *Mtb* pathogenesis has recently been revised. A role for other phagocytic cells than only macrophages has been suggested during TB infection. In particular, neutrophils have been found to be infected in *in vivo* studies (Eum et al., 2010; Repasy et al., 2013), and it has been suggested that neutrophils play a protective role for the host during *Mtb* infection (Perskvist et al., 2000; Lowe et al., 2012).

The zebrafish as a model for mycobacterial infection

The zebrafish, and fish in general, are naturally susceptible to tuberculosis, caused by *Mycobacterium marinum* (*Mm*), which is genetically related to *Mtb*

and shows a similar pathogenesis to the human disease, including the formation of granulomatous lesions (Davis et al., 2002; Swaim et al., 2006). The high level of homology between the zebrafish and human immune system, which consist of comparable cell types, makes the zebrafish a suitable animal model to study host-pathogen interactions (Renshaw and Trede, 2012). Although fish (obviously) do not have lungs, the zebrafish model can be employed to understand the basic mechanisms of respiratory infectious diseases (Martin and Renshaw, 2009). The first advantage of using *Mm* as a tool in tuberculosis studies is its relatively short generation time. The generation time of *Mtb* is about twenty hours, while for *Mm* this takes about four hours, which enables faster and more productive studies. The second advantage is the fact that *Mm* is less harmful to humans, since its growth is restricted in human body temperatures. In case of *Mm* infection in humans, the infection tends to stay in the extremities of the body. As a result, the bacteria can be handled at a relatively low biosafety level.

The larval stage of the zebrafish provides additional advantages for mycobacterial research. First, during the first weeks of development, from embryonic to larval development, they are transparent enabling detailed *in vivo* imaging of the infection process in real time (Davis et al., 2002). Second, during this stage of development only the innate immune cells are present, i.e. macrophages and neutrophils, that have been demonstrated to be sufficient for the formation of early granuloma structures during mycobacterial infection (Davis et al., 2002). These cell types are the first line of defence against invading pathogens, and the cell-type-specific interactions with the bacteria can be studied by imaging in real time. Third, in addition to imaging the immune cell interactions with the bacteria, transcriptome profiles of specific cell types can be studied as well (Rougeot et al., 2014). Fourth, in zebrafish effective gene knockdowns using antisense morpholino oligonucleotides and relatively simple methods for generating specific gene knockouts lines using CRISPR/Cas9 are well established. (Bedell et al., 2011; Hwang et al., 2013).

The zebrafish model for TB has increased our understanding of mycobacterial pathogenesis (van der Vaart et al., 2012; Ramakrishnan, 2013; Cronan and Tobin, 2014). In the classical view of the granuloma structures, it was assumed to be a protective static structure that was driven by the host. However, studies in zebrafish have shown that the secretion of virulence factors is required for the efficient formation of granulomas (Volkman et al., 2004; Stoop et al., 2011). Thus, mycobacteria also benefit from these granuloma structures, which are required for their dissemination within the host as well as for the spread from human to human (Flynn and Chan, 2005; Davis and Ramakrishnan, 2009).

During mycobacterial infection the formation of granuloma structures and the recruitment of phagocytic cells by the host are a highly balanced processes.

Zebrafish larvae with a deficient or a hyperactive immune system are both more susceptible to mycobacterial infection (van der Vaart et al., 2013; Kanwal et al., 2013). A balanced expression of tumor necrosis factor (TNF) plays an important role in maintaining an optimal state. (Clay et al., 2008; Roca and Ramakrishnan, 2013). Therefore, modulating the TNF expression appeared to increase the resistance towards mycobacterial infection (Roca and Ramakrishnan, 2013).

Recent findings in zebrafish larvae suggest a crucial role for TLR-MyD88 signalling pathway in the response to mycobacterial infections. The mycobacterial cell-wall component phthiocerol dimycoceroserate (PDIM) suppresses its recognition by TLRs and thereby inhibits MyD88-mediated pro-inflammatory signalling (Cambier et al., 2014). The activation of TLR-Myd88 signalling has been shown to play a crucial role in host defence against mycobacterial infection, including the induction of autophagic response mediated by DRAM1 (van der Vaart et al., 2014).

The role of neutrophils in mycobacterial pathogenesis is still not well known. In the zebrafish model, neutrophils were observed to have a direct interaction with mycobacteria (Meijer et al., 2008), and inhibition of neutrophil recruitment to the infection site resulted in an enhanced mycobacterial burden (Yang et al., 2012). Neutrophils have been shown to become infected upon recruitment to established granulomas and were able to actively eliminate the mycobacteria by means of oxidative mechanisms (Yang et al., 2012). Enhanced production of reactive nitrogen species (RNS) by neutrophils through the transcription factor hypoxia-inducible factor 1-alpha (Hif-1α) plays an important role in mycobacterial elimination (Elks et al., 2013). These results indicate that innate immune cell types other than macrophages also contribute to host defence against mycobacterial infections.

Recent advances in microscopy techniques

The immune response towards mycobacterial infection consists of complex intracellular signalling for the activation of effectors molecules to eliminate the pathogen, and intercellular signalling that alerts other immune cells of an organism to the presence of infectious agents. Both of these responses can be studied using the zebrafish model. Although the dynamic behavior of cells and intercellular interactions can be visualized using (fluorescence) light microscopy, often higher resolution (electron microscopy) imaging is required for the visualization of intracellular structures, such as the double membrane of autophagic compartments. In the following paragraphs the possibilities of these microscopy techniques will be discussed.

Light microscopy

Light microscopy has been extensively used in biology since the discovery of microorganisms by Antoni van Leeuwenhoek in the 16th century. Innovations in the 20th century have led to phase contrast and differential interference contrast (DIC) microscopy that allow detailed imaging of living cells or even entire organisms without any staining , due to the enhanced contrast provided by these techniques. The successful imaging of tissue or entire organisms using these techniques is mainly dependent on transparency (or translucency), which makes the zebrafish an ideal animal model for light microscopy studies. In zebrafish embryos and larvae, even individual phagocytic cells and pathogens have been visualized using light microscopy techniques (Herbomel et al., 1999; Davis et al., 2002).

Fluorescence microscopy adds the ability to visualize structures with molecular specificity using fluorescently labeled antibodies or fluorescent proteins, such as green fluorescent protein (GFP) (Taylor and Salmon, 1989). Fluorescent proteins can be fused with a protein of interest, which enables the observation of its localization and dynamics. In addition, fluorescent proteins can be fused to a promoter/enhancer region of a gene of interest to generate a reporter construct for the activity of this promoter/enhancer. Promoter fusions are often used to label specific tissues or cell types when promoters are used that are specifically active in a certain cell type. In zebrafish, promoter fusions are often used to generate transgenic lines in which specific cell types are fluorescently labelled, including neutrophils and macrophages (Renshaw et al., 2006; Hall et al., 2007; Ellett et al., 2011).

The availability of fluorescent proteins has spurred the development and improvement of more advanced imaging modalities, including confocal laser scanning microscopy (CLSM) or in short confocal microscopy. Confocal microscopes have a more complicated design compared to traditional fluorescent microscopes. Excitation of fluorophores occurs using an intense spot of laser light which is moved over the specimen. Detection of the emission light is performed by electronic detectors, so-called photomultiplier tubes (PMTs). Finally, a pinhole is introduced in the light path to eliminate out-of-focus signals, which results in fluorescent images from an optical section instead of an entire specimen. By acquiring and combining images from different focal planes, a 3-dimensional reconstruction of the specimen can be realized (Claxton and Fellers, 2006).

Besides confocal microscopy, more recent high-resolution fluorescence microscopy techniques have been developed that improve spatial resolution bypassing Abbe's diffraction limit of 0.2 micrometers (Egner et al., 2002; Hell, 2007). Eric Betzig, Stefan W. Hell and William E. Moerner were awarded the Nobel Prize in Chemistry in 2014 for achieving nanometer scale resolution using fluorescence

microscopy, thereby bypassing Abbe's diffraction limit of 0.2 micrometers. One of these techniques is called stochastic optical reconstruction microscopy (STORM), which relies on the use of blinking fluorophores, that can be detected at the single-molecule level and subsequently localized with a high positional accuracy (Rust et al., 2006). The second technique is stimulated emission-depletion (STED) that uses a laser exciting all the fluorescent molecules, while another light source quenches fluorescence from all molecules except those in a nanometer-sized volume in the middle (Hell and Wichmann, 1994).

Electron microscopy

The curiosity to observe objects that could not be visualized with light microscopy led to the development of electron microscopy, which is an imaging technique that uses accelerated electrons, instead of light waves, as a source of illumination. Since the wavelength of an electron is much shorter than that of visible light, the structure of smaller objects can be determined using an electron microscope. However, the better resolution of EM is compromised by time resolution, since the specimen in EM is always required to be fixed and the imaging is performed in vacuum, so visualization of dynamic processes is impossible. Currently, two main forms of electron microscopes exist. The original form is the transmission electron microscope (TEM), whereas the second form is the scanning electron microscope (SEM).

A TEM, which was invented by Ernst Ruska in 1933, can achieve a resolution of ~1 nm for biological samples, whereas most light microscopes are limited by the diffraction limit of Abbe of 0.2 micrometers. The transmission electron microscope uses electrostatic and electromagnetic lenses to control the electron beam and focus it to form an image. These electron optical lenses are analogous to the glass lenses of an optical light microscope. The electron beam is accelerated by an anode and transmitted through the specimen that is partly transparent to electrons and partly scatters electrons out of the beam. The non-scattered electrons transmitted through the specimen carry the information and after magnification by the objective lens the projection of a specimen can be visualized as an image. The projection can be visualized onto a fluorescent screen and recorded onto a photographic film or a charge-coupled device (CCD) camera.

Transmission electron microscopes are used to investigate the ultrastructure of a wide range of biological and inorganic specimens. Using accelerated electrons requires a vacuum, and therefore a biological specimen typically needs to be chemically fixed and dehydrated, which introduces artefacts in the images acquired from the specimen compared to their natural appearance. A second disadvantage of the TEM for biological samples is the need for extremely thin (~ 100 nm) sections of the specimens, in order for the electrons to be transmitted through the specimen. The ultrathin sectioning also requires embedding of the biological specimens in a polymer resin for stabilization, in addition to the fixation and dehydration. Finally,

these thin sections require treatment with heavy atoms to label lipids and proteins in order to achieve a sufficient contrast in the images.

The SEM generates images of the surface of a specimen and uses a focused electron beam instead of an accelerated electron beam. The focused electron beam probes an area of the specimen by scanning as a raster to produces images. Upon interaction of the electron beam with the specimen, it loses energy by a variety of mechanisms. Subsequently, the lost energy is converted to alternative forms that can be observed as emission of heat, light, x-rays, low energy secondary electrons and high-energy backscattered electrons. These emitted signals provide the information about the properties of the specimen surface. Typically, images are constructed from signals detected by a conventional secondary electron detector, providing a characteristic 3-dimensional appearance of the structures on the surface of a specimen. Similar to TEM, images can be produced from sections using the signals from back-scattered electrons, still by probing the surface of the sections.

Recent innovations have equipped a SEM with an ultramicrotome inside the SEM chamber. Ultramicrotomes are traditionally used to produce ultra-thin sections of biological specimen for TEM imaging. The modified ultramicrotome inside the SEM is able to remove material from the surface of the specimen, revealing a fresh surface for imaging using the focused electron beam. Serial subsequent imaging and sectioning inside the microscope allows high-resolution 3-dimensional imaging of biological samples. This imaging technique is called serial block-face scanning electron microscopy (SBF-SEM) (Denk and Horstmann, 2004; Peddie and Collinson, 2014). Complementary methods have been developed using similar technology, such as Focused ion beam (FIB) SEM, which uses a focused ion beam to remove a thin layer of material from the surface of specimen instead of an ultramicrotome.

Generally, the TEM produces images of biological specimens with much higher resolution compared to the images acquired using a SEM. This difference in resolution is at least an order of magnitude. Although recent advances have enabled acquiring images from a large field of view in TEM (Faas et al., 2012), SEM was already able to produce images from a large field of view since it scans the surface of a specimen point-by-point. Next to the difference in resolution, the main difference between a TEM and a SEM for imaging biological specimen is the ability of acquisition high-resolution images from large volumes. In TEM, the volume is reconstructed after imaging the ultra-thin sections separately and requires intensive image processing afterwards. In contrast, in SBF-SEM and FIB-SEM the images for volume reconstruction are acquired automatically, sometimes by imaging for weeks without interruptions (Peddie and Collinson, 2014).

Outline of the thesis

This thesis focuses on studies on mycobacterial infection in zebrafish using a combination of light and electron microscopy observations . The complex interaction between the intracellular architecture of the host cell and the bacteria, and the dynamics of the intercellular interactions between infected cells are investigated. In order to provide a quantitative analysis of these complex interactions during *Mm* infection *in vivo*, a tail fin infection model of zebrafish larvae was developed, as described in **chapter 2**. In this chapter, the tail fin infection model was used to visualize the autophagic engulfment of *Mm* in host cells. The GFP-Lc3 transgenic zebrafish line, *Tg(CMV:EGFP-map1lc3b)* enabled the visualization of autophagosomal structures using light microscopy. In order to confirm the autophagic nature of these structures, correlative light and electron microscopy (CLEM) was performed on *Mm* infected GFP-Lc3 transgenic zebrafish larvae. We were able to show that the GFP-Lc3-positive structures observed surrounding the bacteria are indeed autophagic in nature and that the smaller (~1 um) GFP-Lc3-positive compartments in the vicinity of *Mm* are autophagosomes. In addition, we quantified in early granulomas the presence of intracellular bacteria in different intracellular compartments, which showed that the majority of bacteria were present as large aggregates and approximately 5% of bacteria were engulfed in autophagic vacuoles.

The role of different phagocytic cells and their contribution to the mycobacterial infection is to a large extent unknown. In **chapter 3,** transgenic zebrafish lines with fluorescently labeled neutrophil and macrophages were used to explore the intercellular dynamics and the fate of infected macrophages and neutrophils during the course of *Mm* infection using the tail fin infection model. The macrophages and neutrophils seem to have distinct functions during infection. The macrophages are mainly responsible for efferocytosis, while the infected neutrophils show reverse migration away from the infection site. Extrusion of epithelial cells after efferocytosis of dead infected immune cells appears to contribute in restriction of bacterial burden, while burst of highly infected macrophages contributes to bacterial growth and dissemination of *Mm*.

The MyD88-mediated signalling plays a major role in mycobacterial infection. MyD88 deficient zebrafish and mice have been shown to be more susceptible to infection by bacteria. In **chapter 4**, the infection progression and the early granulomas were investigated in MyD88-deficient zebrafish larvae. These larvae have an altered immune response against *Mm*, since after phagocytosis of a pathogen the intracellular signalling cascade is blocked. The recruitment of other

phagocytic cells was reduced as well, probably because the MyD88 deficiency also blocks the efficient activation of NF-κB-induced pro-inflammatory signals. Transmission electron microscopy images show that the increase of the bacterial infection is mainly associated with extracellular growth. The quantification of the intracellular compartments containing *Mm* show that probably efferocytosis by macrophages plays an important role in restricting bacterial growth in the mutant larvae.

Finally, the findings in this thesis are discussed and perspectives are proposed for further research on the host-pathogen interactions using the zebrafish as an animal model in **chapter 5.**

References

Armstrong, J.A., and P.D. Hart. 1971. Response of cultured macrophages to Mycobacterium tuberculosis, with observations on fusion of lysosomes with phagosomes. *J. Exp. Med.* 134:713–740. doi:10.1084/jem.134.3.713.

Baxt, L.A., A.C. Garza-Mayers, and M.B. Goldberg. 2013. Bacterial subversion of host innate immune pathways. *Science*. 340:697–701. doi:10.1126/science.1235771.

Bedell, V.M., S.E. Westcot, and S.C. Ekker. 2011. Lessons from morpholino-based screening in zebrafish. *Brief Funct Genomics*. 10:181–188. doi:10.1093/bfgp/elr021.

Berg, R.D., and L. Ramakrishnan. 2012. Insights into tuberculosis from the zebrafish model. *Trends in Molecular Medicine*. 18:689–690. doi:10.1016/j.molmed.2012.10.002.

Cambier, C.J., K.K. Takaki, R.P. Larson, R.E. Hernandez, D.M. Tobin, K.B. Urdahl, C.L. Cosma, and L. Ramakrishnan. 2014. Mycobacteria manipulate macrophage recruitment through coordinated use of membrane lipids. *Nature*. 505:218–222. doi:10.1038/nature12799.

Chapman, J.S., and J.S. Bernard. 1962. The tolerances of unclassified mycobacteria. I. Limits of pH tolerance. *Am. Rev. Respir. Dis.* 86:582–583.

Clay, H., H.E. Volkman, and L. Ramakrishnan. 2008. Tumor necrosis factor signaling mediates resistance to mycobacteria by inhibiting bacterial growth and macrophage death. *Immunity*. 29:283–294. doi:10.1016/j.immuni.2008.06.011.

Comas, I., M. Coscolla, T. Luo, S. Borrell, K.E. Holt, M. Kato-Maeda, J. Parkhill, B. Malla, S. Berg, G. Thwaites, D. Yeboah-Manu, G. Bothamley, J. Mei, L. Wei, S. Bentley, S.R. Harris, S. Niemann, R. Diel, A. Aseffa, Q. Gao, D. Young, and S. Gagneux. 2013. Out-of-Africa migration and Neolithic coexpansion of Mycobacterium tuberculosis with modern humans. *Nat Genet*. 45:1176–1182. doi:10.1038/ng.2744.

Corr, S.C., and L.A.J. O'Neill. 2009. Genetic variation in Toll-like receptor signalling and the risk of inflammatory and immune diseases. *J Innate Immun*. 1:350–357. doi:10.1159/000200774.

Cronan, M.R., and D.M. Tobin. 2014. Fit for consumption: zebrafish as a model for tuberculosis. *Dis Model Mech*. 7:777–784. doi:10.1242/dmm.016089.

Davis, J.M., and L. Ramakrishnan. 2009. The role of the granuloma in expansion and dissemination of early tuberculous infection. *Cell*. 136:37–49. doi:10.1016/j.cell.2008.11.014.

Davis, J.M., H. Clay, J.L. Lewis, N. Ghori, P. Herbomel, and L. Ramakrishnan. 2002. Real-time visualization of mycobacterium-macrophage interactions leading to initiation of granuloma formation in zebrafish embryos. *Immunity*. 17:693–702.

Denk, W., and H. Horstmann. 2004. Serial block-face scanning electron microscopy to reconstruct three-dimensional tissue nanostructure. *Plos Biol*. 2:e329. doi:10.1371/journal.pbio.0020329.

Deretic, V. 2012. Autophagy: An Emerging Immunological Paradigm. *The Journal of Immunology*.

Egner, A., S. Jakobs, and S.W. Hell. 2002. Fast 100-nm resolution three-dimensional microscope reveals structural plasticity of mitochondria in live yeast. *Proc. Natl. Acad. Sci. U.S.A.* 99:3370–3375. doi:10.1073/pnas.052545099.

Elks, P.M., S. Brizee, M. van der Vaart, S.R. Walmsley, F.J. van Eeden, S.A. Renshaw, and A.H. Meijer. 2013. Hypoxia inducible factor signaling modulates susceptibility to mycobacterial infection via a nitric oxide dependent mechanism. *PLoS Pathog*. 9:e1003789. doi:10.1371/journal.ppat.1003789.

Eum, S.-Y., J.-H. Kong, M.-S. Hong, Y.-J. Lee, J.-H. Kim, S.-H. Hwang, S.-N. Cho, L.E. Via, and C.E. Barry. 2010. Neutrophils are the predominant infected phagocytic cells in the airways of patients with active pulmonary TB. *Chest*. 137:122–128. doi:10.1378/chest.09-0903.

Faas, F.G.A., M.C. Avramut, B.M. van den Berg, A.M. Mommaas, A.J. Koster, and R.B.G. Ravelli. 2012. Virtual nanoscopy: generation of ultra-large high resolution electron microscopy maps. *The Journal of Cell Biology*. 198:457–469. doi:10.1083/jcb.201201140.

Flynn, J.L., and J. Chan. 2005. What's good for the host is good for the bug. *Trends Microbiol.* 13:98–102. doi:10.1016/j.tim.2005.01.005.

Gay, N.J., M. Gangloff, and L.A.J. O'Neill. 2011. What the Myddosome structure tells us about the initiation of innate immunity. *Trends in Immunology*. 32:104–109. doi:10.1016/j.it.2010.12.005.

Goldberg, D.E., R.F. Siliciano, and W.R. Jacobs. 2012. Outwitting evolution: fighting drug-resistant TB, malaria, and HIV. *Cell*. 148:1271–1283. doi:10.1016/j.cell.2012.02.021.

Hell, S.W. 2007. Far-field optical nanoscopy. *Science*. 316:1153–1158. doi:10.1126/science.1137395.

Hell, S.W., and J. Wichmann. 1994. Breaking the diffraction resolution limit by stimulated emission: stimulated-emission-depletion fluorescence microscopy. *Opt Lett*. 19:780–782.

Herbomel, P., B. Thisse, and C. Thisse. 1999. Ontogeny and behaviour of early macrophages in the zebrafish embryo. *Development*. 126:3735–3745.

Houben, E.N.G., K.V. Korotkov, and W. Bitter. 2014. Take five - Type VII secretion systems of Mycobacteria. *Biochim. Biophys. Acta*. 1843:1707–1716. doi:10.1016/j.bbamcr.2013.11.003.

Hwang, W.Y., Y. Fu, D. Reyon, M.L. Maeder, S.Q. Tsai, J.D. Sander, R.T. Peterson, J.-R.J. Yeh, and J.K. Joung. 2013. Efficient genome editing in zebrafish using a CRISPR-Cas system. *Nat. Biotechnol.* 31:227–229. doi:10.1038/nbt.2501.

Kanwal, Z., A. Zakrzewska, J. den Hertog, H.P. Spaink, M.J.M. Schaaf, and A.H. Meijer. 2013. Deficiency in hematopoietic phosphatase ptpn6/Shp1 hyperactivates the innate immune system and impairs control of bacterial infections in zebrafish embryos. *The Journal of Immunology*. 190:1631–1645. doi:10.4049/jimmunol.1200551.

Kawai, T., and S. Akira. 2005. Pathogen recognition with Toll-like receptors. *Current Opinion in Immunology*. 17:338–344. doi:10.1016/j.coi.2005.02.007.

Lienhardt, C., M. Raviglione, M. Spigelman, R. Hafner, E. Jaramillo, M. Hoelscher, A. Zumla, and J. Gheuens. 2012. New drugs for the treatment of tuberculosis: needs, challenges, promise, and prospects for the future. *J. Infect. Dis.* 205 Suppl 2:S241–9. doi:10.1093/infdis/jis034.

Lin, S.-C., Y.-C. Lo, and H. Wu. 2010. Helical assembly in the MyD88-IRAK4-IRAK2 complex in TLR/IL-1R signalling. *Nature*. 465:885–890. doi:10.1038/nature09121.

Lowe, D.M., P.S. Redford, R.J. Wilkinson, and A. O'Garra. 2012. Neutrophils in tuberculosis: friend or foe? *Trends in ….*

MacMicking, J.D. 2014. Cell-autonomous effector mechanisms against mycobacterium tuberculosis. *Cold Spring Harb Perspect Med*. 4. doi:10.1101/cshperspect.a018507.

Martin, J.S., and S.A. Renshaw. 2009. Using in vivo zebrafish models to understand the biochemical basis of neutrophilic respiratory. *Biochem. Soc. Trans.*

Medzhitov, R., and C. Janeway. 2000. The Toll receptor family and microbial recognition. *Trends Microbiol.* 8:452–456.

Meijer, A.H., A.M. van der Sar, C. Cunha, G.E.M. Lamers, M.A. Laplante, H. Kikuta, W. Bitter, T.S. Becker, and H.P. Spaink. 2008. Identification and real-time imaging of a myc-expressing neutrophil population involved in inflammation and mycobacterial granuloma formation in zebrafish. *Developmental & Comparative Immunology*. 32:36–49. doi:10.1016/j.dci.2007.04.003.

Mostowy, S. 2013. Autophagy and bacterial clearance: a not so clear picture. *Cellular Microbiology*. 15:395–402. doi:10.1111/cmi.12063.

Ottenhoff, T.H.M. 2012. New pathways of protective and pathological host defense to mycobacteria. *Trends Microbiol.* 20:419–428. doi:10.1016/j.tim.2012.06.002.

Ottenhoff, T.H.M., and S.H.E. Kaufmann. 2012. Vaccines against tuberculosis: where are we and where do we need to go? *PLoS Pathog*. 8:e1002607. doi:10.1371/journal.ppat.1002607.

Peddie, C.J., and L.M. Collinson. 2014. Exploring the third dimension: volume electron microscopy comes of age. *Micron*. 61:9–19. doi:10.1016/j.micron.2014.01.009.

Perskvist, N., L. Zheng, and O. Stendahl. 2000. Activation of human neutrophils by Mycobacterium tuberculosis H37Ra involves phospholipase C gamma 2, Shc adapter protein, and p38 mitogen-activated protein kinase. *J Immunol*. 164:959–965.

Philips, J.A., and J.D. Ernst. 2012. Tuberculosis pathogenesis and immunity. *Annu Rev Pathol*. 7:353–384. doi:10.1146/annurev-pathol-011811-132458.

Ramakrishnan, L. 2012. Revisiting the role of the granuloma in tuberculosis. *Nat Rev Immunol*.

Ramakrishnan, L. 2013. Looking within the zebrafish to understand the tuberculous granuloma. *Adv. Exp. Med. Biol.* 783:251–266. doi:10.1007/978-1-4614-6111-1_13.

Renshaw, S.A., and N.S. Trede. 2012. A model 450 million years in the making: zebrafish and vertebrate immunity. *Dis Model Mech*. 5:38–47. doi:10.1242/dmm.007138.

Repasy, T., J. Lee, S. Marino, N. Martinez, D.E. Kirschner, G. Hendricks, S. Baker, A.A. Wilson, D.N. Kotton, and H. Kornfeld. 2013. Intracellular bacillary burden reflects a burst size for Mycobacterium tuberculosis in vivo. *PLoS Pathog*. 9:e1003190. doi:10.1371/journal.ppat.1003190.

Roca, F.J., and L. Ramakrishnan. 2013. TNF dually mediates resistance and susceptibility to mycobacteria via mitochondrial reactive oxygen species. *Cell*. 153:521–534. doi:10.1016/j.cell.2013.03.022.

Rougeot, J., A. Zakrzewska, Z. Kanwal, H.J. Jansen, H.P. Spaink, and A.H. Meijer. 2014. RNA sequencing of FACS-sorted immune cell populations from zebrafish infection models to identify cell specific responses to intracellular pathogens. *Methods Mol. Biol.* 1197:261–274. doi:10.1007/978-1-4939-1261-2_15.

Rust, M.J., M. Bates, and X. Zhuang. 2006. Sub-diffraction-limit imaging by stochastic optical reconstruction microscopy (STORM). *Nat Meth*. 3:793–795. doi:10.1038/nmeth929.

Simeone, R., F. Sayes, O. Song, M.I. Gröschel, P. Brodin, R. Brosch, and L. Majlessi. 2015. Cytosolic access of Mycobacterium tuberculosis: critical impact of phagosomal acidification control and demonstration of occurrence in vivo. *PLoS Pathog*. 11:e1004650. doi:10.1371/journal.ppat.1004650.

Stoop, E., T. Schipper, and S. Huber. 2011. Zebrafish embryo screen for mycobacterial genes involved in the initiation of granuloma formation reveals a newly identified ESX-1 component. *Disease models & …*.

Swaim, L.E., L.E. Connolly, H.E. Volkman, O. Humbert, D.E. Born, and L. Ramakrishnan. 2006. Mycobacterium marinum infection of adult zebrafish causes caseating granulomatous tuberculosis and is moderated by adaptive immunity. *Infect. Immun.* 74:6108–6117. doi:10.1128/IAI.00887-06.

Takeda, K., and S. Akira. 2004. Microbial recognition by Toll-like receptors. *J. Dermatol. Sci.* 34:73–82. doi:10.1016/j.jdermsci.2003.10.002.

Tan, M.P., P. Sequeira, W.W. Lin, W.Y. Phong, P. Cliff, S.H. Ng, B.H. Lee, L. Camacho, D. Schnappinger, S. Ehrt, T. Dick, K. Pethe, and S. Alonso. 2010. Nitrate respiration protects hypoxic Mycobacterium tuberculosis against acid- and reactive nitrogen species stresses. *PLoS ONE*. 5:e13356. doi:10.1371/journal.pone.0013356.

Tan, S., and D.G. Russell. 2015. Trans-species communication in the Mycobacterium tuberculosis-infected macrophage. *Immunological Reviews*. 264:233–248. doi:10.1111/imr.12254.

Taylor, D.L., and E.D. Salmon. 1989. Basic fluorescence microscopy. *Methods Cell Biol.* 29:207–237.

Tjärnlund, A., E. Guirado, E. Julián, P.-J. Cardona, and C. Fernández. 2006. Determinant role for Toll-like receptor signalling in acute mycobacterial infection in the respiratory tract. *Microbes Infect.* 8:1790–1800. doi:10.1016/j.micinf.2006.02.017.

Torraca, V., S. Masud, H.P. Spaink, and A.H. Meijer. 2014. Macrophage-pathogen interactions in infectious diseases: new therapeutic insights from the zebrafish host model. *Dis Model Mech*. 7:785–797. doi:10.1242/dmm.015594.

van der Sar, A.M., O.W. Stockhammer, C. van der Laan, H.P. Spaink, W. Bitter, and A.H. Meijer. 2006. MyD88 innate immune function in a zebrafish embryo infection model. *Infect. Immun.* 74:2436–2441. doi:10.1128/IAI.74.4.2436-2441.2006.

van der Vaart, M., C.J. Korbee, G.E.M. Lamers, A.C. Tengeler, R. Hosseini, M.C. Haks, T.H.M. Ottenhoff, H.P. Spaink, and A.H. Meijer. 2014. The DNA damage-regulated autophagy modulator DRAM1 links mycobacterial recognition via TLP-MYD88 to authophagic defense. *Cell Host and Microbe*. 15:753–767. doi:10.1016/j.chom.2014.05.005.

van der Vaart, M., H.P. Spaink, and A.H. Meijer. 2012. Pathogen recognition and activation of the innate immune response in zebrafish. *Adv Hematol*. 2012:159807. doi:10.1155/2012/159807.

van der Vaart, M., J.J. van Soest, H.P. Spaink, and A.H. Meijer. 2013. Functional analysis of a zebrafish myd88 mutant identifies key transcriptional components of the innate immune system. *Dis Model Mech*. 6:841–854. doi:10.1242/dmm.010843.

van der Wel, N., D. Hava, D. Houben, D. Fluitsma, M. van Zon, J. Pierson, M. Brenner, and P.J. Peters. 2007. M. tuberculosis and M. leprae Translocate from the Phagolysosome to the Cytosol in Myeloid Cells. *Cell*. 129:1287–1298. doi:10.1016/j.cell.2007.05.059.

Volkman, H.E., H. Clay, D. Beery, J.C.W. Chang, D.R. Sherman, and L. Ramakrishnan. 2004. Tuberculous granuloma formation is enhanced by a mycobacterium virulence determinant. *Plos Biol*. 2:e367. doi:10.1371/journal.pbio.0020367.

Weiss, G., and U.E. Schaible. 2015. Macrophage defense mechanisms against intracellular bacteria. *Immunological Reviews*. 264:182–203. doi:10.1111/imr.12266.

Yang, C.-T., C.J. Cambier, J.M. Davis, C.J. Hall, P.S. Crosier, and L. Ramakrishnan. 2012. Neutrophils exert protection in the early tuberculous granuloma by oxidative killing of mycobacteria phagocytosed from infected macrophages. *Cell Host and Microbe*. 12:301–312. doi:10.1016/j.chom.2012.07.009.

CHAPTER 2

CORRELATIVE LIGHT AND ELECTRON MICROSCOPY IMAGING OF AUTOPHAGY IN A ZEBRAFISH INFECTION MODEL

Rohola Hosseini, Gerda E. M. Lamers, Zlatan Hodzic, Annemarie H. Meijer, Marcel J. M. Schaaf, Herman P. Spaink

Autophagy, 2014

Abstract

High resolution imaging of autophagy has been used intensively in cell culture studies, but so far it has been difficult to visualize this process in detail in whole animal models. In this study we present a versatile method for high resolution imaging of microbial infection in zebrafish larvae by injecting pathogens into the tail fin. This allows visualization of autophagic compartments by light and electron microscopy, which makes it possible to correlate images acquired by the 2 techniques. Using this method we have studied the autophagy response against *Mycobacterium marinum* infection. We show that mycobacteria during the progress of infection are frequently associated with GFP-Lc3-positive vesicles, and that 2 types of GFP-Lc3-positive vesicles were observed. The majority of these vesicles were approximately 1 μm in size and in close vicinity of bacteria, and a smaller number of GFP-Lc3-positive vesicles was larger in size and were observed to contain bacteria. Quantitative data showed that these larger vesicles occurred significantly more in leukocytes than in other cell types, and that approximately 70% of these vesicles were positive for a lysosomal marker. Using electron microscopy, it was found that approximately 5% of intracellular bacteria were present in autophagic vacuoles and that the remaining intracellular bacteria were present in phagosomes, lysosomes, free inside the cytoplasm or occurred as large aggregates. Based on correlation of light and electron microscopy images, it was shown that GFP-Lc3-positive vesicles displayed autophagic morphology. This study provides a new approach for injection of pathogens into the tail fin, which allows combined light and electron microscopy imaging *in vivo* and opens new research directions for studying autophagy process related to infectious diseases.

Introduction

Macroautophagy (hereafter referred to as autophagy) is a well-conserved cellular process that is aimed at targeting cytosolic components for lysosomal degradation. This process plays an important role in the maintenance of cellular homeostasis, inducing degradation of protein aggregates and damaged organelles.(Mizushima et al., 2008) Upon initiation of autophagy, a phagophore is expanded around cytosolic material to form double-membrane vesicles that are called autophagosomes, or initial autophagic vacuoles. After fusion with lysosomes, autolysosomes, also called degradative autophagic vacuoles are formed and their content is degraded, which can be as large as mitochondria.(Dunn, 1990a; Dunn, 1990b; Eskelinen, 2008; Yang and Klionsky, 2010) Substrates can be targeted selectively for autophagic degradation by a molecular tag, like polyubiquitin. Subsequently, these tags are recognized by SQSTM1/p62-like receptors (SLRs), which link the ubiquitinated targets to autophagosome-associated proteins.(Kraft et al., 2010) One of these proteins, microtubule-associated protein 1 light chain 3 (MAP1LC3, abbreviated as LC3), is involved in cargo recruitment and biogenesis of autophagosomes and has successfully been used as a marker for autophagic structures.(Kabeya, 2000; Klionsky et al., 2012; Mizushima et al., 2004)

In addition to its role in cytosolic homeostasis, autophagy is involved in the defense against intracellular microbes.(Gutierrez et al., 2004b; Nakagawa, 2004) Certain types of pathogenic bacterial species are able to escape from phagosomal compartments or inhibit the maturation of phagosomes by manipulating the cell's molecular machinery. It has been shown that the autophagic mechanism can act as a secondary defense line against microbes that evade phagocytotic destruction. (Levine et al., 2011) Besides its role in microbial degradation, autophagy plays a role in the antibacterial defense mechanism by contributing to cytokine secretion and regulation of the immune response, and it may be involved in the clearance of cellular components that have been damaged as a result of the bacterial infection. (Deretic, 2009; Kuballa et al., 2012)

Perhaps the most notorious of intracellular pathogens that can manipulate the host phagocytic process is *Mycobacterium tuberculosis* (*Mtb*), which is estimated to have infected a third of the world population and currently causes nearly one and a half million deaths per year. In macrophages, *Mtb* prevents phagosome-lysosome fusion resulting in immature phagosomes, in which *Mtb* can survive and replicate. (Armstrong, 1971; Russell, 2007a) In some studies *Mtb* has been shown to escape from phagosomes into the cytoplasm.(van der Wel et al., 2007) This translocation requires the early secretory antigenic target 6 system 1 ESX-1, a type VII secretion

system involved in general virulence of pathogenic mycobacterial species.(Houben et al., 2012) ESX-1 permeabilizes phagosomes triggering LC3 recruitment to *Mtb*-containing phagosomes and this secretion system is required for recognition of *Mtb* DNA by the host's DNA sensing pathway initiating autophagy, which leads to degradation of *Mtb* in autolysosomes.(Watson et al., 2012) Induction of autophagy by starvation, inhibition of MTOR or interferon-gamma treatment can stimulate phagosomal maturation and restrict mycobacterial replication.(Bradfute et al., 2013b; Fabri et al., 2011; Gutierrez et al., 2004b) In additional mechanistic studies, autophagy has been shown to produce autolysosomes containing antimicrobial peptides from specific ribosomal and ubiquitinated proteins capable of killing *Mtb*. (Alonso et al., 2007; Ponpuak et al., 2010)

Microscopy data on autophagy has mainly been generated using cell culture studies, and fewer studies have been performed on whole animal model systems. Besides the obvious increased validity of vertebrate animal models, these systems enable studying the autophagic response in different cell types and the interactions between these cell types. Ultimately, this may facilitate the development of novel therapies against autophagy-related disorders.(Boglev et al., 2013; Dowling et al., 2010; Fleming and Rubinsztein, 2011) In the present study, we have used the zebrafish animal model for high resolution imaging of autophagy during bacterial infection. Zebrafish embryos and larvae are extensively used because of their visual transparency, allowing fluorescent imaging of a wide variety of disease processes. (Meeker and Trede, 2008) The zebrafish is currently being used as a model system to study autophagy different fields, such as development,(Benato et al., 2013; Hu et al., 2011) neurodegeneration(Fleming and Rubinsztein, 2011; Wager and Russell, 2013) and infection(Mostowy et al., 2013). An important tool is the GFP-Lc3 transgenic zebrafish line, *Tg(CMV:EGFP-map1lc3b)*, which enables the visualization of autophagosomal structures.(He et al., 2009) This line has previously been used to show the autophagy response against bacterial infection.(Mostowy et al., 2013; van der Vaart et al., 2012)

The exact role of LC3 and its homologs in intracellular processes has not entirely been elucidated yet. It is clear that LC3 is not exclusively involved in biogenesis of autophagosomes, but is also involved in membrane expansion of other organelles.(Hanson et al., 2010; Lai and Devenish, 2012) In innate immunity, it has been reported that the Toll-like receptor signaling pathway triggers the recruitment of LC3 to phagosomal membranes. (Sanjuan et al., 2007) In addition, LC3 is recruited to phagosome-enclosed apoptotic cells.(Florey et al., 2011; Sanjuan et al., 2007) In order to study autophagy in zebrafish, it is important to visualize this process by electron microscopy and to be able to correlate the obtained images to the images of GFP-Lc3 structures observed with light microscopy. This is especially important due to the current lack of antibodies that can be used as specific autophagy markers

in the zebrafish model.

Zebrafish are a natural host for infection by *M. marinum* with similar phenotypes as *Mtb* infection in human tissues.(Stamm and Brown, 2004; Tobin and Ramakrishnan, 2008) Similar to *Mtb*, *M. marinum* can propagate in macrophages by preventing phagosome-lysosome fusion. The infected leukocytes subsequently attract other immune cells, leading to the formation of organized cellular aggregates called granulomas.(Berg and Ramakrishnan, 2012) *M. marinum* can escape from the phagosome into the cytosol and develop actin-based motility.(Stamm et al., 2003b) Different procedures have been established to induce systemic *M. marinum* infection in zebrafish embryos and larvae, of which injection of bacteria into the caudal vein is most widely used.(Benard et al., 2012) However, high resolution imaging of cellular processes during these systemic infections, such as autophagy, is complicated. Using light microscopy, the applicability of high numerical aperture (NA) lenses is limited when infected tissues are located deeper inside the organism, and out of focus interference greatly limits the resolution and contrast. Using electron microscopy, which is required to visualize cellular ultrastructures such as autophagic vacuoles, it is extremely labor-intensive to localize infected cells that are scattered throughout the body of the zebrafish larvae.

In this study we present a novel infection model for pathogens in zebrafish larvae. Microinjection of *M. marinum* directly into the tail fin of zebrafish larvae results in a highly localized infection. This enables studying intracellular processes during the entire course of the infection process, from the infection of a few cells until formation of a granuloma. In particular, the role of autophagy during this process can be investigated using visualization of the autophagosomal structures by high-resolution light and electron microscopy. Using this approach we show that autophagy is induced during the course of infection by *M. marinum*. Using light microscopy, a large number of small GFP-Lc3-positive structures (~1 μm) and a small number (±6 per granuloma) of larger (~3 μm) GFP-Lc3-positive structures (containing bacteria) were observed in the infected tissue. These larger GFP-Lc3-positive structures containing bacteria were significantly more common in leukocytes than in the remaining cell types and mostly positive for the acidicity marker LysoTracker Red (LyTR). Using electron microscopy it was shown that about 5% of intracellular bacteria were present in autophagic vacuoles, and that the majority of these compartments had degradative autophagic vacuole morphology. Correlation of light and electron microscopy images showed that the small GFP-Lc3-positive vesicles in the vicinity of bacteria, as well as the larger GFP-Lc3 structure containing sequestered bacteria have autophagic vacuole morphology. Thus, our results show that by using the presented tail fin infection method, the autophagy process during the course of infection can be studied by direct observations *in vivo.*

Results

The tail fin infection model

In the present study a model was set up which enabled studying autophagy during bacterial infection in zebrafish by visualizing intracellular structures using both light and electron microscopy. For this purpose a local infection was established using microinjection of bacteria into the tail fin of zebrafish larvae at 3 days post fertilization (dpf). At this stage the tail fin is approximately 20- to 50-micrometers thick. It consists of a thin layer containing mesenchymal cells, extracellular matrix, collagenous fibers (called actinotrichia), and an epidermis that consists of 2 cell layers covering the tail fin on both sides.(Kimmel et al., 1995) Several hours after injection of fluorescently labeled *M. marinum* in the tail fin (~500 colony-forming units), by confocal laser scanning microscopy (CLSM) a small number of bacteria can be visualized in the tail fins, which reside in epithelial cell layers and in the extracellular matrix. An overview of this model system is presented in Figure 1, showing tail fin infection of E2-Crimson labeled *M. marinum* in transgenic zebrafish larvae expressing membrane-bound GFP.(Cooper et al., 2005) In order to visualize the ultrastructure of the infected tail fin, the infected larvae can subsequently be processed for transmission electron microscopy.

Injection of *M. marinum* in zebrafish larvae results in an innate immune response represented by recruitment of leukocytes to the site of infection and subsequent formation of granulomas.(Berg and Ramakrishnan, 2012; Meijer and Spaink, 2011) In order to study the course of infection and leukocyte recruitment in the tail fin infection model, we injected E2-Crimson labeled *M. marinum* into the tail fin of 3 dpf zebrafish larvae and visualized neutrophils and macrophages. This visualization of neutrophils was performed using a transgenic zebrafish line *Tg(mpx:GFP),* in which GFP is expressed in neutrophils.(Renshaw et al., 2006) Lcp1/L-plastin immunostaining was performed for visualization of all leukocytes, and Lcp1-positive cells without GFP expression were considered to be macrophages.(Mathias et al., 2009) The course of infection was imaged using CLSM at 4 h postinfection (hpi) and 1, 3, and 5 days postinfection (dpi) (Fig. 2). At 4 hpi, small numbers of fluorescently labeled bacteria (<50) were detected at and around the site of injection. At this time point a few neutrophils and macrophages (<5) were already recruited to the infection site. Some of the bacteria were taken up by leukocytes (Fig. 2A). The bacteria that did not show colocalization with leukocytes could be extracellular or reside in other cell types. After this time point the bacteria proliferate and most of them appeared to grow in aggregates, which are at least 5 μm in size. In addition, increasing numbers of both neutrophils and macrophages were attracted. At 4 to 5 dpi the infection in the tail fin resulted in formation of

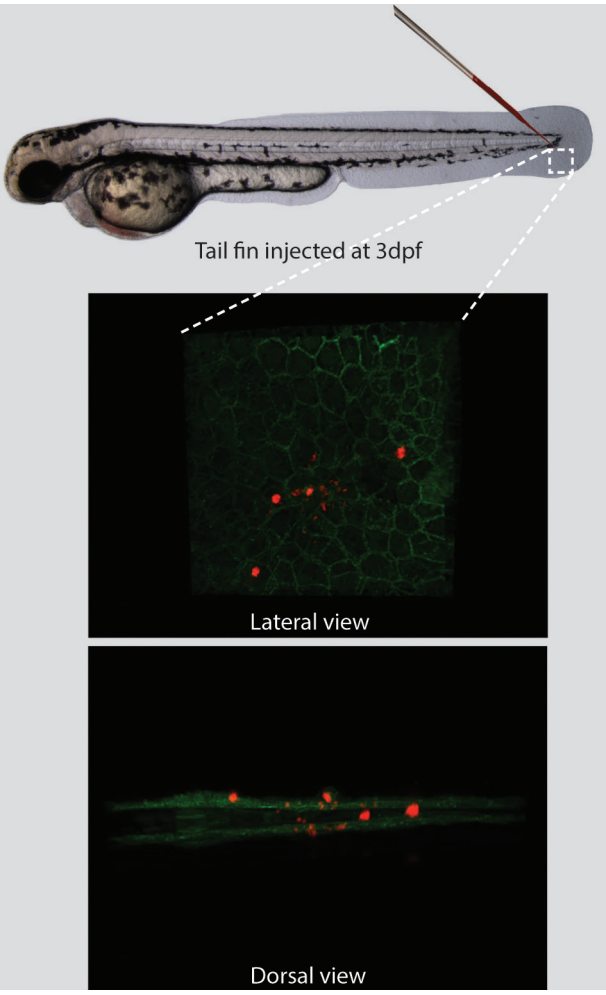

Figure 1. The tail fin injection model, enabling the induction of a localized infection in zebrafish larvae. The needle indicates the location for injection in the tail fin of 3 dpf zebrafish larvae. The inset represents the region imaged by CLSM. The transgenic larva expressing membrane-bound GFP was injected with fluorescently labeled *M. marinum* (shown in red). The larva is imaged and presented from a lateral and dorsal perspective, showing the epithelial cell layers and the bacteria residing in these layers and in the extracellular space between these layers.

an initial stage granuloma, which we observed as a large local accumulation of macrophages (20 to 30) and neutrophils (20 to 30) at the site of the infection, close to the site of injection. At this stage in the center of the granuloma a pore in the tail fin had been formed representing the necrotic (caseous) center of a granuloma, which has been reported previously in the granulomas of human lungs and adult zebrafish.(Pozos et al., 2004; Russell, 2007b) Due to the thin tissue of the tail fin this center was extruded, resulting in a pore at late stages of infection (see also Fig. 3D). The development of these granulomas appeared to be dependent on an ESX-1 secretion system, since the *M. marinum* Delta RD1 mutant strain,(McLaughlin et al., 2007) which is deficient in this system, was cleared within 4 dpi (data not shown).

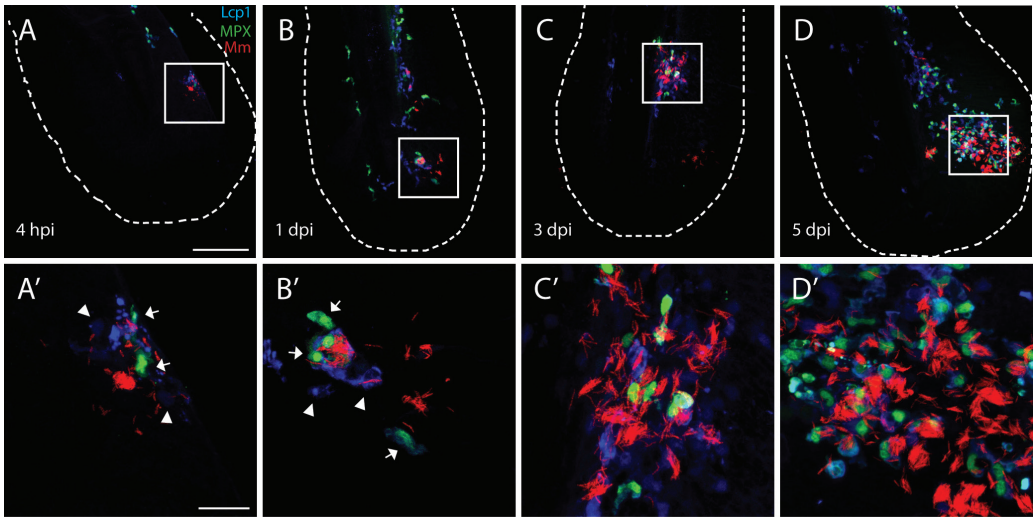

Figure 2. *M. marinum* infection attracts leukocytes forming an initial stage granuloma. The course of *M. marinum* (red) infection is shown in *Tg(mpx:GFP)* larvae. Larvae have been stained using Lcp1 immunohistochemistry for leukocytes. Recruitment of neutrophils (green) and leukocytes (blue) was observed in the tail fin. In the top panels (**A to D**) an overview image of the entire tail fin at the indicated time point is presented. In the lower panels (**A' to D'**) higher magnification images of the indicated regions are shown. The scale bars represent 100 µm for the images on the top panels and 20 µm for the bottom panels. For each time point approximately 20 larvae were imaged and representative images for each time point are shown.

Autophagy during *M. marinum* infection: confocal laser scanning microscopy

In order to study whether the *Tg(CMV:EGFP-map1lc3b)* fish line(He et al., 2009) can be used in our infection model to study autophagy, we injected 3 dpf larvae from this line with fluorescently labeled *M. marinum* in the tail fin. At 4 hpi and 1, 3, and 5 dpi the GFP-Lc3 signal and the fluorescent bacteria were imaged using CLSM (Fig. 3).

At 4 hpi the response to *M. marinum* infection was observed as small (<1 µm) GFP-Lc3-positive vesicles, not containing bacteria, in cells close to the site of injection. These vesicles were not specific to the antibacterial response since in a control experiment a similar GFP-Lc3 response was observed after injection of polystyrene beads (Fig. S1). In this control experiment the GFP-Lc3 response was no longer observed from 1 dpi onward, indicating that any GFP-Lc3 response after this time point is specific for the bacterial infection (Fig. 3A). One day after bacterial injection, more bacteria were present and the increased infection results in more small GFP-Lc3-positive vesicles in infected cells. The vast majority of these vesicles was ~1 µm in diameter and did not contain bacteria (Fig. 3B). This pattern was also

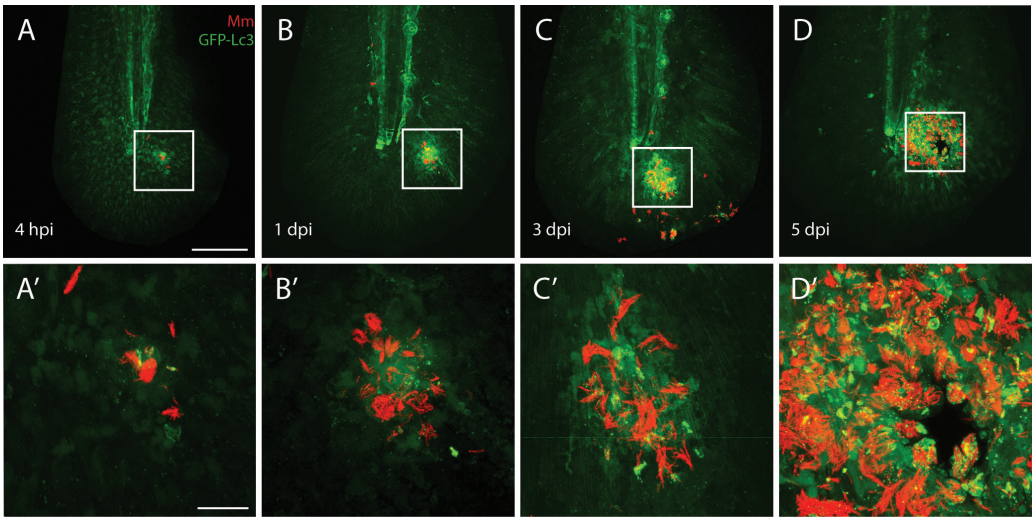

Figure 3. Autophagy is induced during *M. marinum* infection. *M. marinum* infected *Tg(CMV:EGFP-map1lc3b)* larvae were imaged at different time points after infection. GFP-Lc3-positive (green) vesicles were observed at the site of infection from 4 hpi to 5 dpi in the vicinity of the pathogens (red) by CLSM. In the top panels (**A to D**) an overview of the entire tail fin imaged at low magnification is shown. In the bottom panels (**A' to D'**) the indicated region imaged at higher magnification is presented. A necrotic center is formed at the center of the initial stage granuloma at 5 dpi. The scale bars represent 100 μm for the images in the top panels and 20 μm for images in the bottom panels. For each time point approximately 20 larvae were imaged and representative images for each time point are shown.

observed at 3 dpi (Fig. 3C). At 5 dpi in most larvae an initial stage granuloma had been formed, which could be observed as a large local accumulation of bacterial aggregates and GFP-Lc3-positive vesicles.

Different types of interaction between GFP-Lc3 structures and bacteria were observed at 5 dpi, and this is shown in more detail in Fig. 4. The vast majority of bacterial aggregates did not colocalize with any GFP-Lc3 signal, however in some cells accumulation of GFP-Lc3 vesicles occurred associated with these aggregates (i.e. the fluorescent signals from the bacteria and the vesicles are (partially) overlapping; Fig. 4B). Few cells contained larger GFP-Lc3-positive vesicles (~3 μm, ~6 per granuloma), which contained sequestered bacteria (Fig. 4C to F). A large number (a few thousand) of small (~1 μm) GFP-Lc3-positive vesicles were present, which did not contain bacteria, although they could be observed in the vicinity of bacteria (Fig. 4G and H). These small vesicles were able to fuse with the other compartments that contain bacteria. This process was monitored in a separate experiment, in which infected *Tg(CMV:EGFP-map1lc3b)* larvae were imaged alive (Movie S1). In addition, GFP-Lc3-positive vesicles were observed in the vicinity of *M. marinum* without fusion with compartments containing bacteria (Movie S2).

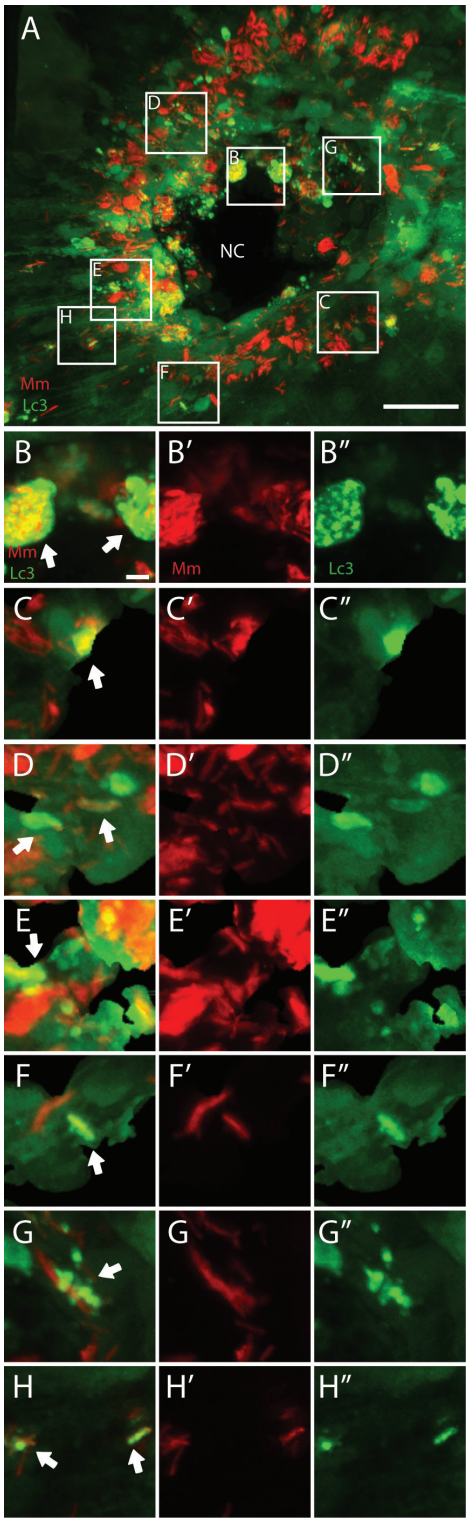

Figure 4. The GFP-Lc3 response observed during *M. marinum* infection. *Tg(CMV:EGFP-map1lc3b)* larvae infected with *M. marinum* at 5 dpi were imaged with CLSM. (**A**) Representative image of a granuloma in the infected tail fin. The GFP-Lc3 signal (green) and fluorescently labeled bacteria (red) are shown. (**B to H**) Magnified images of regions indicated in (**A**). (**B**) In highly infected cells near the necrotic center (NC) accumulation of GFP-Lc3-positive vesicles was observed (indicated by arrow). (**C to F**) In cells shown in these images larger GFP-Lc3-positive vesicles were observed, which entirely surround the bacteria (indicated by arrows). (**G and H**) In lowly infected cells GFP-Lc3-positive vesicles were observed in the vicinity of bacteria (indicated by arrows). Red and green signals from (**B to H**) are presented separately in (**B' to H'**) and (**B'' to H''**), respectively. Scale bar: A, 30 μm and B to H, 3 μm.

In order to differentiate between the GFP-Lc3 signal in leukocytes and the remaining cell types, infected *Tg(CMV:EGFP-map1lc3b)* larvae were immuno-stained using an antibody against Lcp1, a pan-leukocytic marker (Fig. 5). By segmentation, based on the Lcp1 signal, of the 3D rendered images 2 images were generated. One image showed the bacteria and GFP-Lc3-positive structures inside Lcp1-positive cells (Fig. 5C) and the other image showed this in the remaining cell types (Fig. 5D). Quantitative analysis of 13 granulomas (1 per larva) showed that the majority of larger GFP-Lc3-positive vesicles containing bacteria were located inside leukocytes (Fig. 5B). Each granuloma contained on average 5.4 (± 1.0) of these large vesicles containing bacteria. Of these vesicles, 3.9 (± 0.6) were located inside leukocytes and 1.5 (± 0.4) were located outside Lcp1-positive cells. No statistically significant difference in the number of small (~1 μm) GFP-Lc3-positive vesicles was observed between leukocytes and the remaining cell types (data not shown).

The lysosomal marker LyTR was used to study which fraction of the GFP-Lc3-positive vesicles had undergone fusion with lysosomal compartments (Fig. 6). The number of GFP-Lc3 vesicles positive for this marker was quantified, and approximately 30% of the small GFP-Lc3 vesicles were shown to be LyTR positive (Fig. 6D). Approximately 70% of the larger GFP-Lc3 vesicles containing bacteria were positive for this lysosomal marker, indicating that the majority of these vesicles had undergone fusion with a lysosomal compartment (Fig. 6C).

Autophagy during *M. marinum* infection: transmission electron microscopy

Transmission electron microscopy (TEM) was performed at 5 dpi of *M. marinum* infection in the tail fin of wild type larvae, in order to study the autophagy response and ultrastructure in more detail (Fig. 7). The tail fin infection model is very suitable for TEM analyses because the localization of infected cells is facilitated by the limited amount of tissue that needs to be analyzed in this local infection model. As described above, at 5 dpi a granuloma has been formed and a representative TEM image of such a granuloma is shown in Figure 7. At the left side of the image a part of the necrotic center of the granuloma is visible. This center is surrounded by a large number of cells infected with bacteria, which represent a variety of cell-bacteria interactions.

Four regions of this image are presented at higher magnification illustrating different cell-bacteria interactions (Fig. 7B to E). The images show that some cells contain bacteria that are encapsulated by a double-membrane vesicle. Such an initial autophagic vacuole inside a macrophage is presented in Figure 7B'. Other bacteria residing in the cytoplasm of the same macrophage were not enclosed by

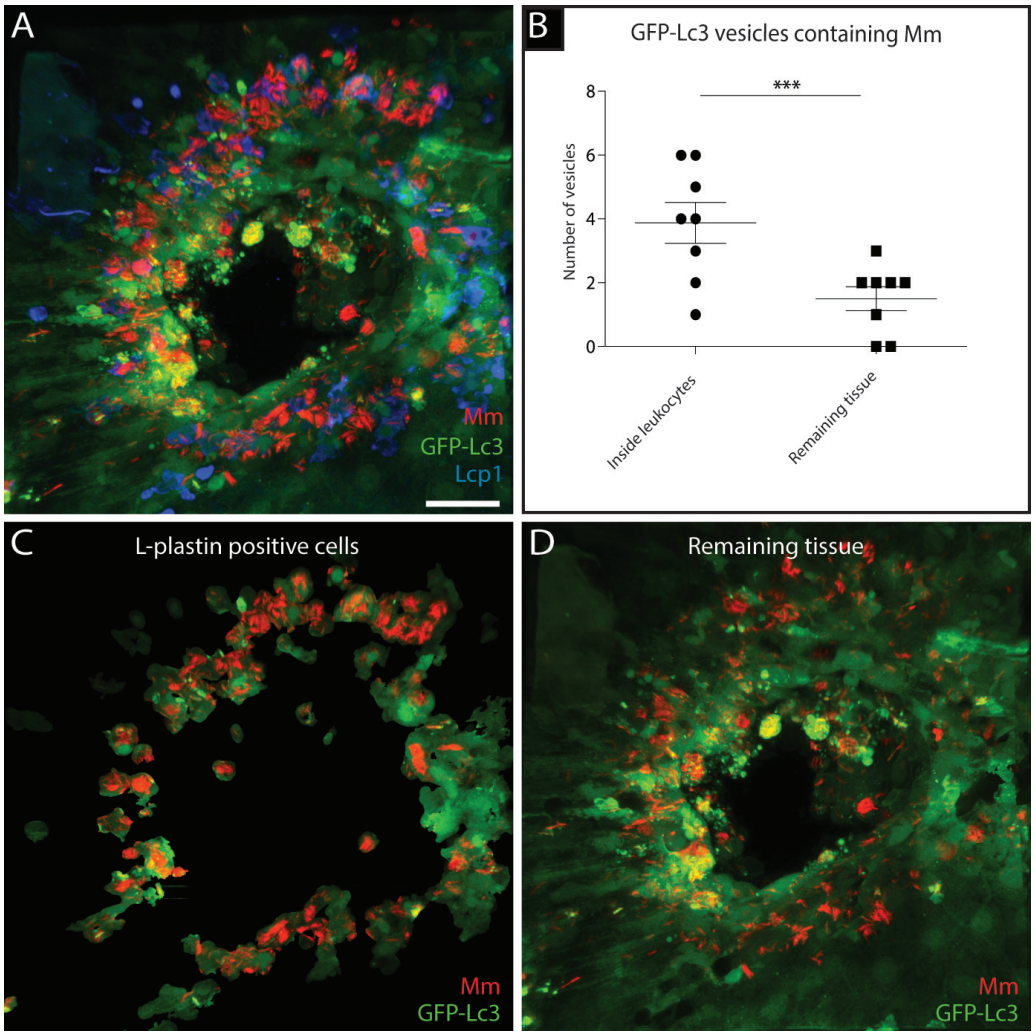

Figure 5. *M. marinum* containing GFP-Lc3-positive vesicles differ between leukocytes and other cell types. *Tg(CMV:EGFP-map1lc3b)* larvae infected with *M. marinum* at 5 dpi were immunostained for Lcp1, and their tail fins were imaged using CLSM. (**A**) Representative image of a granuloma in the infected tail fin. The GFP-Lc3 signal (green), Lcp1 immunostaining (blue) and fluorescently labeled bacteria (red) are shown. (**B**) Quantification of GFP-Lc3-positive vesicles for 13 granulomas (1 per tail fin) having sequestered *M. marinum* inside and outside Lcp1-positive leukocytes. The data (mean ± SEM) were analyzed using a paired two-tailed student t test (n=13). *** indicates $P<0.001$. (**C**) The GFP-Lc3 signal (green) and bacteria (red) in Lcp1-positive cells. (**D**) The GFP-Lc3 signal (green) and bacteria (red) outside Lcp1-positive cells. Scale bar: 30 μm.

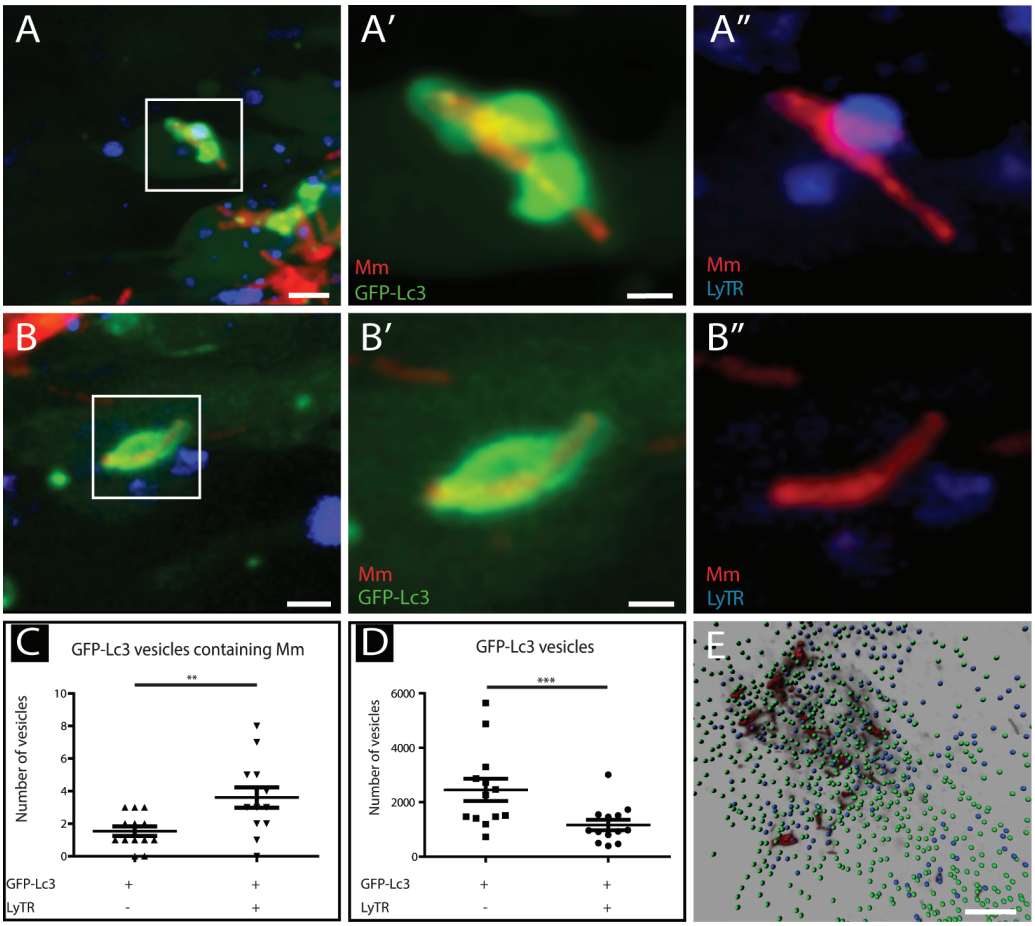

Figure 6. The majority of GFP-Lc3-positive vesicles having sequestered *M. marinum* are LyTR-positive. *Tg(CMV:EGFP-map1lc3b)* larvae infected with *M. marinum* at 5 dpi were stained with LyTR and their tail fins were imaged using CLSM. (**A and B**) Representative images of *M. marinum* in GFP-Lc3-positive vesicles that were positive (**A**) or negative (**B**) for LyTR. Magnified images of the regions indicated in (**A and B**) are presented separately for *M. marinum* (red) and GFP-Lc3 (green) in (**A' and B'**), and for *M. marinum* (red) and LyTR (blue) in (**A" and B"**). (**C**) Quantification of *M. marinum* containing GFP-Lc3-positive vesicles, positive or negative for LyTR. The data (mean ± SEM) were analyzed using a paired two-tailed student t test (n=13). *** indicates $P<0.001$ and ** $P<0.01$. (**D**) Quantification of small GFP-Lc3 vesicles positive and negative for LyTR. The data (mean ± SEM) were analyzed using a paired two-tailed student t test (n=13). (**E**) Representative image of a 3D-rendered representation of small (~1µm) GFP-Lc3 vesicles, negative (green) or positive (blue) for LyTR. Scale bar: A and B 5 µm, A' and B' 1 µm and E 25 µm.

any membrane (Fig. 7B). Some bacteria were encapsulated by single membrane structures with degradative autophagic vacuole morphology. An example is presented in Figure 7C, which shows a cell, most probably a macrophage, with an autophagic vacuole containing a bacterium and the remains of partially degraded cytoplasmic material. Many other macrophages contained larger aggregates of bacteria enclosed by a single membrane. Examples of these bacteria containing phagosomes in macrophages are shown in Figure 7D. Moreover, infected epithelial cells with bacteria were observed, and an example is shown in Figure 7E.

In order to determine the frequency of different cell-bacteria interactions we quantified the occurrence of 7 different types of interaction. This quantitative analysis and representative images of each type of interaction are presented in Fig. 8. The majority (~57%) of intracellular bacteria was found in aggregates, and approximately half of these aggregates had lysosomal morphology with uniform electron dense content in the compartment (~32%) (Fig. 8 A and B). Individual bacteria occurred in phagosomal compartments characterized by a single membrane with an electron-transparent zone or tightly surrounding the bacteria without any cytoplasmic material (~11%, Fig.8C). In addition bacteria were found in the cytoplasm not enclosed by any membrane (~13%, Fig. 8A). Approximately 5% of bacteria were found in autophagic compartments, either in a typical double membrane compartment also enclosing cytoplasmic content such as ribosomes (~0.4%, Fig. 8D) or in a compartment with late autophagic morphology (~4.5%). These compartments were characterized by partially degraded cytoplasmic content and organelles (Fig. 8E). Finally, ~12% of bacteria were located inside lysosomal compartment with regular electron dense content (Fig8F).

Correlating light and electron microscopy images

Since we could obtain both CLSM and TEM images of the same specimen, the tail fin infection model provided the opportunity to correlate images generated by these 2 types of microscopy. For this purpose, infected larvae were first imaged alive using CLSM, and directly after imaging chemically fixed and prepared for electron microscopy (Fig. 9). This approach enabled the visualization of the ultrastructure of the GFP-Lc3-positive and negative structures containing bacteria that first had been identified by CLSM.

The tail fin of a *Tg(CMV:EGFP-map1lc3b)* larva infected with E2-crimson labeled bacteria (3 dpi) was first imaged using low magnification CLSM (Fig. 9A), followed by higher magnification imaging of the region of interest and 3D rendering (Fig. 9B). In this image (like in the images shown in Figure 3 and 4), the majority of bacteria was not sequestered by GFP-Lc3-positive membranes. However, some

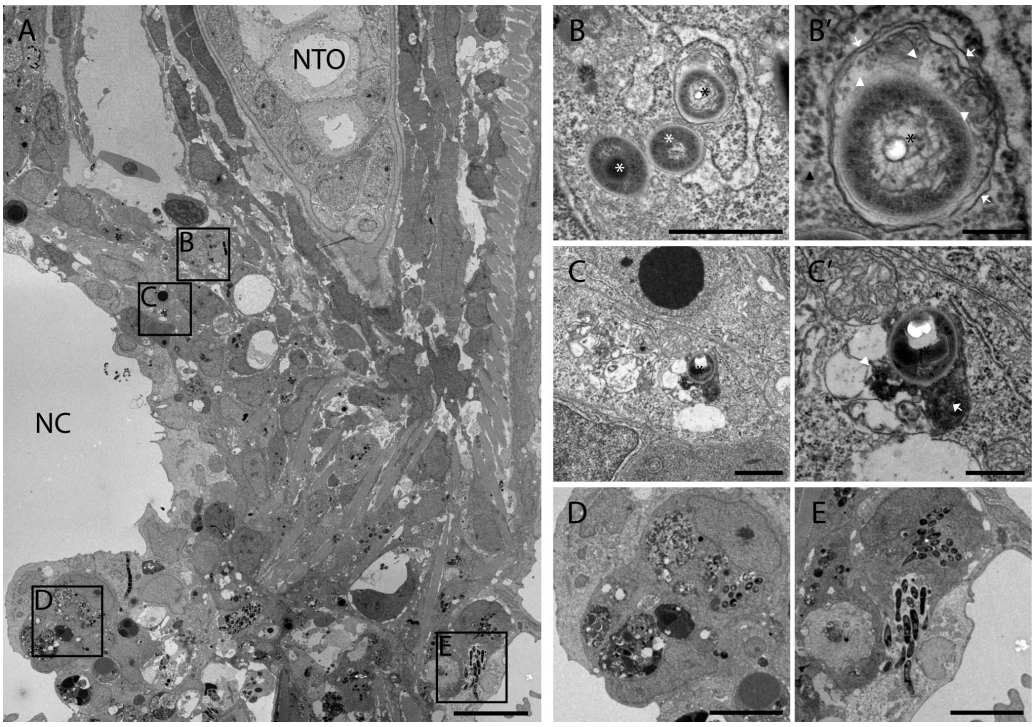

Figure 7. TEM images of tail fin of zebrafish larva infected with M. marinum. **(A)** Overview image of a granuloma with necrotic center (NC) in the tail fin at 5 dpi. The tail fin is oriented anterior to the top and ventral to the left and the position of the notochord (NTO) is indicated. (**B**) Higher magnification of the region indicated in (**A**), showing part of a macrophage with bacteria of which one in a double-membrane autophagic vacuole (black asterisk) and 2 were cytoplasmic (white asterisk). (**B'**) Higher magnification of bacteria in an initial autophagic vacuole in (**B**), with arrows indicating the typical double membrane with electron-lucent cleft and arrowheads indicating ribosomes inside (white) and outside (black) of the vacuole. The ruffled appearance of the double membrane could be a fixation or sectioning artefact. (**C**) Higher magnification of region indicated in (**A**), showing a single bacterium (asterisk) in a degradative autophagic vacuole. (**C'**) Higher magnification of the degradative autophagic vacuole containing bacteria in (**C**), showing a lysosome fused with this vacuole (arrow), which contains partially degraded cytoplasmic material (arrowhead). (**D**) Higher magnification of indicated region, showing a macrophage with several phagosomal compartments containing bacteria. (**E**) Higher magnification of indicated region, showing infected epithelial cells. Scale bars: A 5 μm, B and C 1 μm, B' 250 nm, C' 500 nm, and D and E 10 μm.

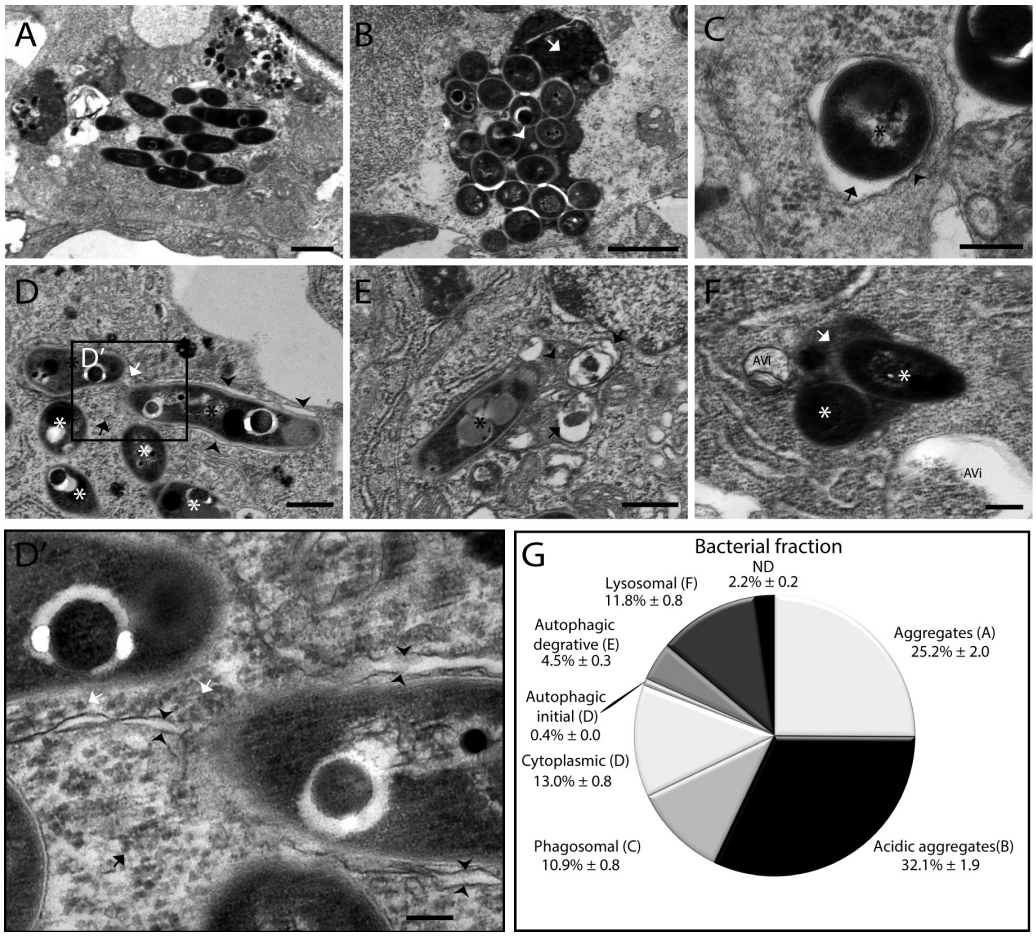

Figure 8. Quantification of intracellular *M. marinum* shows the distribution of bacteria in different compartments. (**A to F**) Representative TEM images of M. marinum in different compartments. (**A**) Aggregates were observed as a compact cluster of bacteria (<5) without any electron dense areas. (**B**) Acidic aggregates were observed as a compact number of bacteria in a compartment having a uniform electron density between the bacteria (arrowhead) and/or electron dense regions (arrow). (**C**) Phagosomal compartment containing bacteria surrounded by a single membrane (arrowhead) with an electron-transparent zone (arrow), without any cytoplasmic material in the compartment. (**D**) Initial autophagic vacuoles containing bacteria (black asterisk), with the typical double membrane with electron-lucent cleft (arrowheads) and arrows indicating ribosomes inside (white) and outside (black) of the vacuole. In this image also cytoplasmic bacteria are shown not enclosed by any membrane, indicated by a white asterisk. (**D'**) Higher magnification of the region indicated in (**D)**, showing part of the bacteria and the vacuole in more detail. (**E**) Degradative autophagic vacuoles with partially degraded content (arrowhead) and other fused vacuoles (arrows). (**F**) Lysosomal compartment containing bacteria (asterisk) with uniform electron dense content (arrow). Near this compartment 2 autophagic vacuoles were observed indicated by AVi. (**G**) The fractions of intracellular *M. marinum* found in

different compartments and free cytoplasmic *M. marinum* are presented in a pie chart. The bacteria for which their compartment could not be determined are indicated as ND. For this experiment 3 larvae with initial stage granulomas were used, with 3 regions for each larva at ~10 μm distance in order to prevent double counting of bacteria. In total 9 sections were analyzed containing over 2400 intracellular bacteria. Data shown are mean ± SEM. The scale bar represents 500 nm in A and B, 250 nm in C and D and 1 μm in E and F.

bacteria were observed in close proximity to GFP-Lc3-positive vesicles and a small number of bacteria were inside a GFP-Lc3-positive structure. Subsequently, samples were sectioned and 2 adjacent sections were imaged by TEM (Fig. 9C). The TEM images showed that in this region all bacteria were located inside epithelial cells. The 2 TEM images were aligned and the surface area covered by the bacteria was segmented (Fig. 9D). This surface area was fitted into the 3D rendered image of the bacteria created from the CLSM images (Fig. 9E and F).

Using this approach, different cell-bacteria interactions were observed. Firstly, bacteria inside a GFP-Lc3-positive structure were observed using CLSM (Fig. 9G). In the correlated TEM image these bacteria were present in a degradative autophagic vacuole that also contained partially degraded cytoplasmic material (Fig. 9H). Secondly, in the same CLSM image other bacteria were observed which were not inside a GFP-Lc3-positive structure. However, they were observed to be associated with small GFP-Lc3-positive vesicles (Fig. 9I). In the correlated TEM image this vesicle correlates with an autophagic vacuole containing cytoplasmic material and having a double membrane (Fig. 9J).

Discussion

In this paper we provide a novel infection method that enables visualization of autophagic structures by both light and electron microscopy *in vivo* using a vertebrate infectious disease model. We show that this opens up the possibility to correlate light and electron microscopic images. In our method the pathogens are injected into the tail fin of zebrafish larvae, which results in a localized infection in this thin part of the body. We utilized this model for the study of infection by *M. marinum* showing that injection of this pathogen in the tail fin results in a local infection, which leads to the formation of single granuloma-like structure. The tail fin is very suitable for high-resolution light microscopy imaging, because the tissue consists of only a few cell layers and the infected cells are therefore located at a relatively short distance from the objective. This provides the opportunity to use high NA lenses, which are generally designed with a short free working distance.

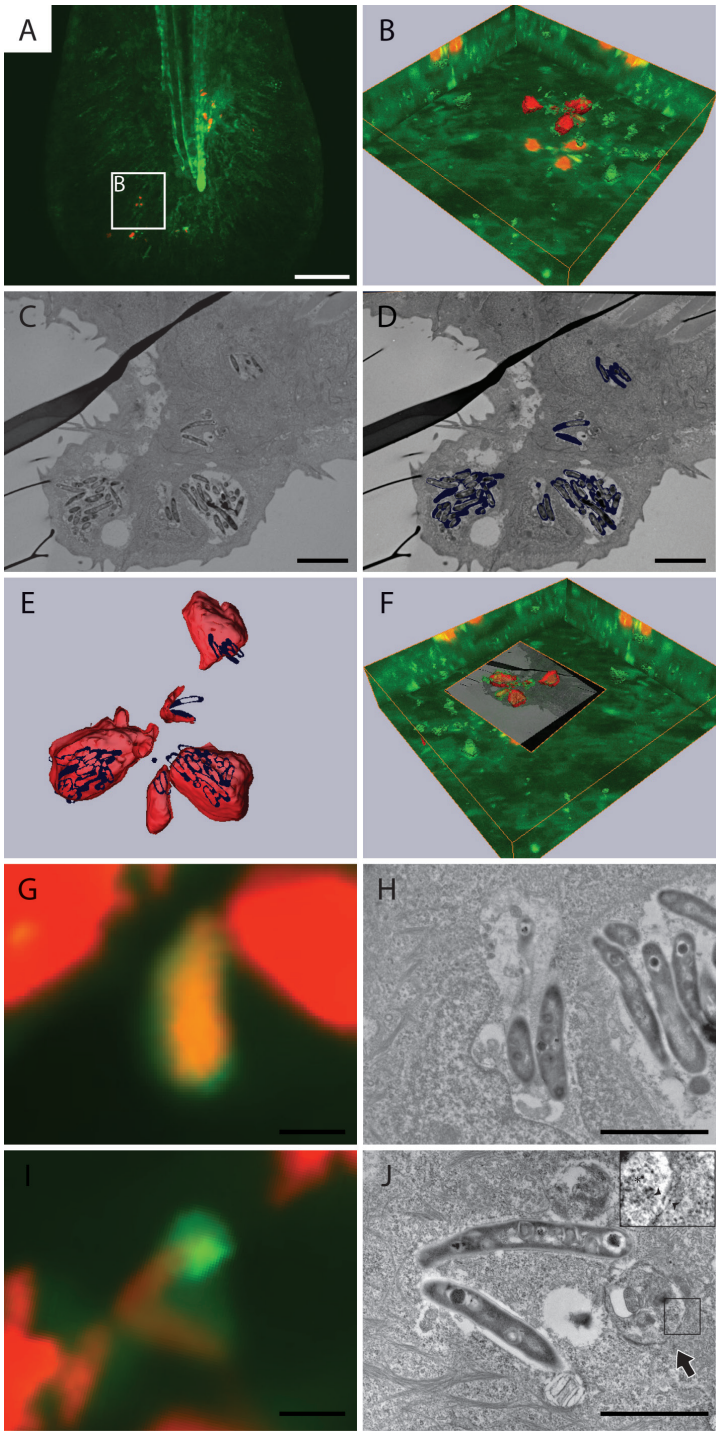

Figure 9. Correlative light and electron microscopy shows the ultrastructure of GFP-Lc3-positive structures. (**A**) CLSM image of infected *Tg(CMV:EGFP-map1lc3b)* zebrafish tail fin at 3 dpi. (**B**) Higher magnification of region indicated in (**A**), showing the projection view and the surface of the bacteria in red and of the GFP-Lc3 signal in green. (**C**) TEM image of the same area shown in (**B**). (**D**) Segmentation of adjacent TEM images showing the surface area of bacteria in blue. (**E**) Alignment of bacterial surfaces. The fluorescent signal (imaged by CLSM) is shown in red and the segmented surface (imaged by TEM) in blue. (**F**) 3D representation of CLSM and TEM images based on alignment shown in (**E**). (**G**) Magnified image of GFP-Lc3-positive structure enclosed 2 bacteria. (**H**) TEM image of the GFP-Lc3-positive compartment with bacteria shown in (**G**). (**I**) Magnified image with GFP-Lc3 signal in vicinity of bacteria. (**J**) TEM image of the same region, showing an initial autophagic vacuole, (indicated by arrow), at the tip of bacteria at same position as GFP-Lc3 signal in (**H**). The magnified inset shows the double membrane (arrowheads) and the ribosomes (asterisk) inside this vacuole. Scale bars: A 20 µm, B to F 5 µm, and G and H 1 µm.

The relative absence of out of focus light enhances the contrast and the resolution of images of this tissue. For transmission electron microscopy this localized infection model has the major advantage that the site of infection can easily be found and subsequently imaged, due to the small tissue volume that needs to be investigated. When this tissue is imaged in live larvae using light microscopy before TEM imaging, the images obtained by these 2 different techniques can be correlated. This was performed based on the localization of the bacteria, which can be easily recognized in TEM images and were fluorescently labeled for detection in light microscopy. This model will be very valuable for high resolution *in vivo* imaging of autophagy, which until now has mainly been performed in cell cultures.

The applicability of studying autophagy in the tail fin infection model was demonstrated using *M. marinum* infection. Using the *Tg(CMV:EGFP-map1lc3b)* line, we showed highly active mobilization of GFP-Lc3-positive vesicles upon infection of *M. marinum* in the tail fin. Two types of GFP-Lc3-positive structures were distinguished. First, numerous relatively small vesicles (~1 μm) were observed that did not contain bacteria. These small vesicles are highly dynamic and can fuse with other compartments containing bacteria. Correlation of light and electron microscopy images showed that the presented small GFP-Lc3-positive vesicle in the vicinity of bacteria indeed has the appearance of an initial autophagic vacuole (Fig. 9J). Second, larger structures (~3 μm) were present that often contained sequestered bacteria. The GFP-Lc3 signal of these larger structures could either originate from an autophagosome, which has taken up cytosolic bacteria, or from an autophagosome/autolysosome after fusion with a phagosomal compartment containing bacteria as has been shown in cell culture studies.(Bradfute et al., 2013a; Gutierrez et al., 2004a; Lerena and Colombo, 2011) It has also been shown in cell cultures that GFP-LC3 can be associated with early phagosomes and phagosomes that have taken up bacteria of apoptotic bodies.(Florey et al., 2011; Sanjuan et al., 2009) In our system the majority of larger bacteria containing GFP-Lc3 vesicles were stained positive with LyTR indicating that they had undergone fusion with a lysosomal compartment. These vesicles are most probably GFP-Lc3-containing autolysosomes that have emerged through the autophagic pathway, although it could not be excluded that they are fused with lysosomes as part of LC3-associated phagocytosis. The autophagosomal nature of these vesicles was supported by correlative light and electron microscopy data showing that the larger GFP-Lc3 vesicle containing bacteria had the morphology of a degradative autophagic vacuole.

The presented observations of larger and small GFP-Lc3-positive vesicles reflect the occurrence of different pathways of autophagy induced during infection. The larger GFP-Lc3 vesicles containing bacteria may correspond to bacterial autophagy, whereas the smaller vesicles in the vicinity of bacteria may correspond to non-bacterial autophagy, reviewed in refs. 12 and 53. The latter process may

be involved in the clearance of membranes that have been damaged during phagosomal escapes of *M. marinum*. Alternatively, these vesicles may fuse with other autophagic or heterophagic compartments containing bacteria.(Bradfute et al., 2013a; Mostowy, 2013; Ponpuak and Deretic, 2011) Furthermore, the presented data show that during *M. marinum* infection the larger bacteria-containing GFP-Lc3 vesicles occur more often in leukocytes than in other cell types (mainly epithelial cells in the tail fin). This suggest that different cell types show different autophagic responses, illustrating the advantages of studying the infection process in a whole animal model, in which multiple cell types and their interactions can be studied at the same time. In future studies these experiments can be performed in other transgenic fish lines, expressing GFP-Lc3 in specific cell types, or using the line ubiquitously expressing GFP-Lc3 in combination with other cell-specific fluorescent markers. In addition, in future research it will be important to determine which fraction of GFP-Lc3-positive vesicles without bacteria are autophagosomes.

The suitability of the tail fin infection model for electron microscopy was demonstrated by analysis of granuloma structures. It was confirmed that at this stage the bacteria resided in different cell types and that they could occur in the extracellular matrix. We quantified the number of intracellular bacteria residing individually in phagosomes, the cytoplasm, autophagic vacuoles, or lysosomes, or being present in aggregates or acidic aggregates. Only a very small fraction (~0.4%) of bacteria was found inside an initial autophagic vacuole with a double membrane, which is most likely due to the highly transient nature of these structures. (Pfeifer, 1978; Schworer et al., 1981) These autophagosomes generally contain a single bacterium. The fraction of bacteria in degradative autophagic vacuoles is considerably larger (~4.5%). Another population of bacteria resides in phagosomal compartments and this fraction of bacteria (~11%) has been taken up most recently or has succeeded in blocking lysosomal fusion. For *M. marinum* it has been shown in cell cultures that they are able to escape the phagosomal compartment,(Stamm et al., 2003a) which was shown in our model to result in ~13% of bacteria residing freely in the cytoplasm. This fraction of bacteria is an obvious target for autophagy. (Bradfute et al., 2013a; Lerena and Colombo, 2011)

In summary, our model offers new possibilities for future studies on the role of autophagy during infection *in vivo*. Recently, Mostowy et al., have studied the response of zebrafish larvae towards another pathogen, *Shigella flexneri*, showing that escape of this pathogen into the cytosol induces septin caging and targeting to autophagy.(Mostowy et al., 2013) It would be highly interesting to compare the infection process by different pathogens in the model we have developed. The zebrafish has many advantages for genetic studies that make it highly suitable to provide new insights into the relation between cellular structures and the molecular mechanisms of autophagy. With the advancement of medical translational studies

in zebrafish disease models this will provide new opportunities to develop possible therapies against autophagy-related disorders.(Rubinsztein et al., 2012; Wager and Russell, 2013)

Materials and Methods

Zebrafish strains and maintenance

Zebrafish were handled in compliance with the local animal welfare regulations and maintained according to standard protocols (www.zfin.org). The ABTL wild type zebrafish strain and the transgenic lines, *Tg(Ola.Actb:Hsa.HRAS-EGFP),*(Cooper et al., 2005) *Tg(mpx:GFP),*(Renshaw et al., 2006) *Tg(CMV:EGFP-map1lc3b),*(He et al., 2009) strains were used for this study. All fish were raised and grown at 28.5 °C on a 14 h light : 10 h dark cycle. Embryos were obtained from natural spawning at the beginning of the light period and kept in egg water (60 μg/ml Instant Ocean sea salts). At 1 dpf 0.003% *N*-phenylthiourea (PTU; Sigma-Aldrich, P7629) was added in order to prevent pigmentation.

Zebrafish tail fin infection

The *M. marinum* M strain fluorescently labeled with E2-crimson(Strack et al., 2009) was used and prepared at ~500 colony-forming units per 1 nl as previously described. (Benard et al., 2012) Borosilicate glass microcapillaries (Harvard Apparatus, 300038) were used with a micropipette puller device (Sutter Instruments Inc.) for preparing microinjection needles. Zebrafish larvae were injected in the tail fin at 3 dpf using the Eppendorf microinjection system with a fine (~5 to 10 micron) needle tip broken off with tweezers and mounted at a 30-degree angle. Larvae were anesthetized in egg water with 200 μg/mL 3-aminobenzoic acid (Tricaine; Sigma-Aldrich, E10521) and injected between the 2 epidermal layers at the ventral part of the tail fin (Fig. 1). Larvae were fixed at desired time points after infection with 4% paraformaldehyde in PBS-T (phosphate-buffered saline; NaCl 150 mM, K_2HPO_4 15 mM, KH_2PO_4 5 mM) with 0.05% Tween 20 (Merck Millipore, 8221840500) with gentle agitation for 18 h at 4 °C. The larvae were washed the next day with PBS-T and stored at 4 °C for further staining or until imaging.

Immunohistochemistry

Lcp1 immunostaining was performed for at least 20 larvae from each time point after fixation. The larvae were rinsed in PBS-DTx (phosphate-buffered saline with 0.5% DMSO and 0.3% Triton X-100) and treated with proteinase K (10 μg/ml in

PBS-DTx; Roche, 03115879001) for 10 min at 37 °C. The larvae were blocked in 5% normal sheep serum (Sigma-Aldrich, S2263) in PBS-DTx for 2 h at room temperature, incubated with Lcp1/L-Plastin antibody (a gift from Anna Huttenlocher, University of Wisconsin, USA) in 1:1000 dilution at 4 °C overnight and subsequently incubated with Alexa-405 conjugated secondary antibody (1:200; Invitrogen, A-31556) for 2 h at room temperature. The larvae were washed with PBS-DTx and stored at 4°C until imaging.

LysoTracker Red staining

LysoTracker Red (LyTR; Invitrogen, L-7528) was used for visualization of acidic compartments. Larvae were incubated for 1 h in 10 μM LyTR solution (in egg water) at 28 °C and rinsed several times with fresh egg water before imaging by CLSM.

Confocal laser scanning microscopy

Fixed larvae were mounted in 1% low melting agarose (Sigma-Aldrich, A9414) and imaged with a Leica TCS SPE (Wetzlar, Germany) or Zeiss Exciter (Oberkochen, Germany) confocal laser scanning microscope using the 405, the 488 and the 641 laser lines with 20X (NA 0.7) and 63X (NA 1.2) objectives. Larvae shown in Figures 4 and 6 were imaged with the Nikon A1 confocal laser scanning microscope (Tokyo, Japan) using the 405, 488 and 561 laser lines with 20X (NA 0.75) and 60X objectives (NA 1.49). Images were analyzed using Fiji software,(Schindelin et al., 2012) and Imaris 5.5 software (Bitplane AG) was utilized in order to develop 3-dimensional models of the infected sites to quantify the number of GFP-Lc3-positive vesicles and their colocalization with LyTR signals. Amira 2.3 software (FEI, Visualization Sciences Group) was used for 3D rendering of CLSM images, segmentation of TEM images and aligning the 2 surfaces for correlative visualization.

Transmission electron microscopy

Before being used for electron microscopy the zebrafish larvae were anesthetized with 200 μg/ml tricaine, imaged alive by CLSM and afterwards immediately fixated in 2% glutaraldehyde and 2% paraformaldehyde in sodium *cacodylate buffer (*pH 7.2) *for 3 h at room temperature followed by fixation for 16 h at* 4 °C. Postfixation was performed in 1% osmium tetroxide in sodium *cacodylate buffer* for 1 h at room temperature. After dehydration through a graded series of ethanol all specimens were kept in epoxy resin (Agar Scientific, AGR1043) for 16 h before embedding. Ultrathin sections were collected on Formvar coated 200 mesh or one hole copper grids (Agar Scientific, AGS162) stained with 2% uranyl acetate in 50% ethanol and lead citrate for 10 min each. Electron microscopy images were obtained with a JEOL JEM-1010 transmission electron microscope (Tokyo, Japan) equipped with an

Olympus Megaview camera (Tokyo, Japan).

Statistical analysis

All data (mean ± SEM) were analysed (Prism 5.0) using paired, two-tailed student t tests for comparing 2 conditions.

Acknowledgements

We thank Dan Klionsky (University of Michigan) for providing the GFP-Lc3 zebrafish line and Ulrike Nehrdich, Laura van Hulst, and Davy de Witt for fish care. We thank Serge Mostowy (Imperial College London) for critical reading of the manuscript, and Bram Koster and Erik Bos (Leiden University Medical Center) for helpful discussion. Infectious disease research in our laboratory is supported by the SmartMix Program of the Netherlands Ministry of Economic Affairs and the Ministry of Education, Culture and Science, the European Commission 7th framework project ZF-HEALTH (HEALTH-F4-2010-242048) and the Cyttron II Program (LSH framework: FES0908).

References

Alonso, S., K. Pethe, D.G. Russell, and G.E. Purdy. 2007. Lysosomal killing of Mycobacterium mediated by ubiquitin-derived peptides is enhanced by autophagy. *In* Proc. Natl. Acad. Sci. U.S.A. Vol. 104. 6031-6036.

Armstrong, J.A., and P.D. Hart. 1971. Response of cultured macrophages to Mycobacterium tuberculosis, with observations on fusion of lysosomes with phagosomes. *J. Exp. Med.* 134:713–740. doi:10.1084/jem.134.3.713.

Benard, E.L., A.M. van der Sar, F. Ellett, G.J. Lieschke, H.P. Spaink, and A.H. Meijer. 2012. Infection of zebrafish embryos with intracellular bacterial pathogens. *In* J Vis Exp.

Benato, F., T. Skobo, G. Gioacchini, I. Moro, F. Ciccosanti, M. Piacentini, G.M. Fimia, O. Carnevali, and L.D. Valle. 2013. Ambra1 knockdown in zebrafish leads to incomplete development due to severe defects in organogenesis. *In* autophagy. Vol. 9.

Berg, R.D., and L. Ramakrishnan. 2012. Insights into tuberculosis from the zebrafish model. *In* Trends in Molecular Medicine. Vol. 18. 689-690.

Boglev, Y., A.P. Badrock, A.J. Trotter, Q. Du, E.J. Richardson, A.C. Parslow, S.J. Markmiller, N.E. Hall, T.A. de Jong-Curtain, A.Y. Ng, H. Verkade, E.A. Ober, H.A. Field, D. Shin, C.H. Shin, K.M. Hannan, R.D. Hannan, R.B. Pearson, S.-H. Kim, K.C. Ess, G.J. Lieschke, D.Y.R. Stainier, and J.K. Heath. 2013. Autophagy induction is a tor- and tp53-independent cell survival response in a zebrafish model of disrupted ribosome biogenesis. *In* PLoS Genet. Vol. 9. e1003279.

Bradfute, S.B., E.F. Castillo, J. Arko-Mensah, S. Chauhan, S. Jiang, M. Mandell, and V. Deretic. 2013a. Autophagy as an immune effector against tuberculosis. *Curr. Opin. Microbiol.* 16:355-365.

Bradfute, S.B., E.F. Castillo, J. Arko-Mensah, S. Chauhan, S. Jiang, M. Mandell, and V. Deretic. 2013b. Autophagy as an immune effector against tuberculosis. *In* Curr. Opin. Microbiol. Vol. 16. 355-365.

Cooper, M.S., D.P. Szeto, G. Sommers-Herivel, J. Topczewski, L. Solnica-Krezel, H.-C. Kang, I. Johnson, and D. Kimelman. 2005. Visualizing morphogenesis in transgenic zebrafish embryos using BODIPY TR methyl ester dye as a vital counterstain for GFP. *In* Dev. Dyn. Vol. 232. 359-368.

Deretic, V. 2009. Multiple regulatory and effector roles of autophagy in immunity. *In* Current Opinion in Immunology. Vol. 21. 53-62.

Dowling, J.J., S.E. Low, A.S. Busta, and E.L. Feldman. 2010. Zebrafish MTMR14 is required for excitation-contraction coupling, developmental motor function and the regulation of autophagy. *In* Hum. Mol. Genet. Vol. 19. 2668-2681.

Dunn, W.A. 1990a. Studies on the mechanisms of autophagy: formation of the autophagic vacuole. *In* The Journal of Cell Biology. Vol. 110. 1923-1933.

Dunn, W.A. 1990b. Studies on the mechanisms of autophagy: maturation of the autophagic vacuole. *In* The Journal of Cell Biology. Vol. 110. 1935-1945.

Eskelinen, E.-L. 2008. New insights into the mechanisms of macroautophagy in mammalian cells. *In* Int Rev Cell Mol Biol. Vol. 266. 207-247.

Fabri, M., S. Stenger, D.-M. Shin, J.-M. Yuk, P.T. Liu, S. Realegeno, H.-M. Lee, S.R. Krutzik, M. Schenk, P.A. Sieling, R. Teles, D. Montoya, S.S. Iyer, H. Bruns, D.M. Lewinsohn, B.W. Hollis, M. Hewison, J.S. Adams, A. Steinmeyer, U. Zügel, G. Cheng, E.-K. Jo, B.R. Bloom, and R.L. Modlin. 2011. Vitamin D is required for IFN-gamma-mediated antimicrobial activity of human macrophages. *In* Sci Transl Med. Vol. 3. 104ra102.

Fleming, A., and D.C. Rubinsztein. 2011. Zebrafish as a model to understand autophagy and its role in neurological disease. *In* Biochimica et Biophysica Acta (BBA) - Molecular Basis of Disease. Vol. 1812. 520-526.

Florey, O., S.E. Kim, C.P. Sandoval, C.M. Haynes, and M. Overholtzer. 2011. Autophagy machinery mediates macroendocytic processing and entotic cell death by targeting single membranes. *Nat. Cell Biol.* 13:1335-1343.

Gutierrez, M.G., S.S. Master, S.B. Singh, G.A. Taylor, M.I. Colombo, and V. Deretic. 2004a. Autophagy is a defense mechanism inhibiting BCG and Mycobacterium tuberculosis survival in infected macrophages. *Cell*. 119:753-766.

Gutierrez, M.G., S.S. Master, S.B. Singh, G.A. Taylor, M.I. Colombo, and V. Deretic. 2004b. Autophagy is a defense mechanism inhibiting BCG and Mycobacterium tuberculosis survival in infected macrophages. *In* Cell. Vol. 119. 753-766.

Hanson, H.H., S. Kang, M. Fernández-Monreal, T. Oung, M. Yildirim, R. Lee, K. Suyama, R.B. Hazan, and G.R. Phillips. 2010. LC3-dependent intracellular membrane tubules induced by gamma-protocadherins A3 and B2: a role for intraluminal interactions. *Journal of Biological Chemistry*. 285:20982-20992.

He, C., C.R. Bartholomew, W. Zhou, and D.J. Klionsky. 2009. Assaying autophagic activity in transgenic GFP-Lc3 and GFP-Gabarap zebrafish embryos. *In* autophagy. Vol. 5. 520-526.

Houben, D., C. Demangel, J. van Ingen, J. Perez, L. Baldeon, A.M. Abdallah, L. Caleechurn, D. Bottai, M. van Zon, K. de Punder, T. van der Laan, A. Kant, R. Bossers-de Vries, P. Willemsen, W. Bitter, D. van Soolingen, R. Brosch, N. van der Wel, and P.J. Peters. 2012. ESX-1-mediated translocation to the cytosol controls virulence of mycobacteria. *Cellular Microbiology*. 14:1287-1298.

Hu, Z., J. Zhang, and Q. Zhang. 2011. Expression pattern and functions of autophagy-related gene atg5 in zebrafish organogenesis. *In* autophagy. Vol. 7. 1514-1527.

Kabeya, Y. 2000. LC3, a mammalian homologue of yeast Apg8p, is localized in autophagosome membranes after processing. *In* The EMBO Journal. Vol. 19. 5720-5728.

Kimmel, C.B., W.W. Ballard, S.R. Kimmel, B. Ullmann, and T.F. Schilling. 1995. Stages of embryonic development of the zebrafish. *In* Dev. Dyn. Vol. 203. 253-310.

Klionsky, D.J., F.C. Abdalla, H. Abeliovich, R.T. Abraham, A. Acevedo-Arozena, K. Adeli, L. Agholme, M. Agnello, P. Agostinis, J.A. Aguirre-Ghiso, H.J. Ahn, O. Ait-Mohamed, S. Ait-Si-Ali, T. Akematsu, S. Akira, H.M. Al-Younes, M.A. Al-Zeer, M.L. Albert, R.L. Albin, J. Alegre-Abarrategui, M.F. Aleo, M. Alirezaei, A. Almasan, M. Almonte-Becerril, A. Amano, R. Amaravadi, S. Amarnath, A.O. Amer, N. Andrieu-Abadie, V. Anantharam, D.K. Ann, S. Anoopkumar-Dukie, H. Aoki, N. Apostolova, G. Arancia, J.P. Aris, K. Asanuma, N.Y.O. Asare, H. Ashida, V. Askanas, D.S. Askew, P. Auberger, M. Baba, S.K. Backues, E.H. Baehrecke, B.A. Bahr, X.-Y. Bai, Y. Bailly, R. Baiocchi, G. Baldini, W. Balduini, A. Ballabio, B.A. Bamber, E.T.W. Bampton, G. Bánhegyi, C.R. Bartholomew, D.C. Bassham, R.C. Bast, H. Batoko, B.-H. Bay, I. Beau, D.M. Béchet, T.J. Begley, C. Behl, C. Behrends, S. Bekri, B. Bellaire, L.J. Bendall, L. Benetti, L. Berliocchi, H. Bernardi, F. Bernassola, S. Besteiro, I. Bhatia-Kissova, X. Bi, M. Biard-Piechaczyk, J.S. Blum, L.H. Boise, P. Bonaldo, D.L. Boone, B.C. Bornhauser, K.R. Bortoluci, I. Bossis, F. Bost, J.-P. Bourquin, P. Boya, M. Boyer-Guittaut, P.V. Bozhkov, N.R. Brady, C. Brancolini, A. Brech, J.E. Brenman, A. Brennand, E.H. Bresnick, P. Brest, D. Bridges, M.L. Bristol, P.S. Brookes, E.J. Brown, J.H. Brumell, et al. 2012. Guidelines for the use and interpretation of assays for monitoring autophagy. *In* autophagy. Vol. 8. 445-544.

Kraft, C., M. Peter, and K. Hofmann. 2010. Selective autophagy: ubiquitin-mediated recognition and beyond. *In* Nat. Cell Biol. Vol. 12. 836-841.

Kuballa, P., W.M. Nolte, A.B. Castoreno, and R.J. Xavier. 2012. Autophagy and the Immune System. *In* Annu. Rev. Immunol. Vol. 30. 611-646.

Lai, S.-c., and R.J. Devenish. 2012. LC3-Associated Phagocytosis (LAP): Connections with Host Autophagy. *Cells*. 1:396-408.

Lerena, M.C., and M.I. Colombo. 2011. Mycobacterium marinum induces a marked LC3 recruitment to its containing phagosome that depends on a functional ESX-1 secretion system. *Cellular Microbiology*. 13:814-835.

Levine, B., N. Mizushima, and H.W. Virgin. 2011. Autophagy in immunity and inflammation. *In* Nature. Vol. 469. 323-335.

Mathias, J.R., M.E. Dodd, K.B. Walters, S.K. Yoo, E.A. Ranheim, and A. Huttenlocher. 2009. Characterization of zebrafish larval inflammatory macrophages. *In* Developmental & Comparative Immunology. Vol. 33. 1212-1217.

McLaughlin, B., J.S. Chon, J.A. MacGurn, F. Carlsson, T.L. Cheng, J.S. Cox, and E.J. Brown. 2007. A Mycobacterium ESX-1–Secreted Virulence Factor with Unique Requirements for Export. *In* PLoS Pathog. Vol. 3. Public Library of Science. e105.

Meeker, N.D., and N.S. Trede. 2008. Immunology and zebrafish: spawning new models of human disease. *In* Developmental & Comparative Immunology. Vol. 32. 745-757.

Meijer, A.H., and H.P. Spaink. 2011. Host-pathogen interactions made transparent with the zebrafish model. *In* Curr Drug Targets. Vol. 12. 1000-1017.

Mizushima, N., B. Levine, A.M. Cuervo, and D.J. Klionsky. 2008. Autophagy fights disease through cellular self-digestion. *In* Nature. Vol. 451. 1069-1075.

Mizushima, N., A. Yamamoto, M. Matsui, T. Yoshimori, and Y. Ohsumi. 2004. In Vivo Analysis of Autophagy in Response to Nutrient Starvation Using Transgenic Mice Expressing a Fluorescent Autophagosome Marker.

Mostowy, S. 2013. Autophagy and bacterial clearance: a not so clear picture. *Cellular Microbiology*. 15:395-402.

Mostowy, S., L. Boucontet, M.J. Mazon Moya, A. Sirianni, P. Boudinot, M. Hollinshead, P. Cossart, P. Herbomel, J.-P. Levraud, and E. Colucci-Guyon. 2013. The Zebrafish as a New Model for the In Vivo Study of Shigella flexneri Interaction with Phagocytes and Bacterial Autophagy. *In* PLoS Pathog. Vol. 9. e1003588.

Nakagawa, I. 2004. Autophagy Defends Cells Against Invading Group A Streptococcus. *In* Science. Vol. 306. 1037-1040.

Pfeifer, U. 1978. Inhibition by insulin of the formation of autophagic vacuoles in rat liver. A morphometric approach to the kinetics of intracellular degradation by autophagy. *The Journal of Cell Biology*. 78:152-167.

Ponpuak, M., A.S. Davis, E.A. Roberts, M.A. Delgado, C. Dinkins, Z. Zhao, H.W. Virgin IV, G.B. Kyei, T. Johansen, I. Vergne, and V. Deretic. 2010. Delivery of Cytosolic Components by Autophagic Adaptor Protein p62 Endows Autophagosomes with Unique Antimicrobial Properties. *In* Immunity. Vol. 32. 329-341.

Ponpuak, M., and V. Deretic. 2011. Autophagy and p62/sequestosome 1 generate neo-antimicrobial peptides (cryptides) from cytosolic proteins. *autophagy*. 7:336-337.

Pozos, T.C., L. Ramakrishnan, and L. Ramakrishan. 2004. New models for the study of Mycobacterium-host interactions. *Current Opinion in Immunology*. 16:499-505.

Renshaw, S.A., C.A. Loynes, D.M.I. Trushell, S. Elworthy, P.W. Ingham, and M.K.B. Whyte. 2006. A transgenic zebrafish model of neutrophilic inflammation. *In* Blood. Vol. 108. 3976-3978.

Rubinsztein, D.C., P. Codogno, and B. Levine. 2012. Autophagy modulation as a potential therapeutic target for diverse diseases. *In* Nat Rev Drug Discov. Vol. 11. 709-730.

Russell, D.G. 2007a. Who puts the tubercle in tuberculosis? *In* Nat. Rev. Microbiol. Vol. 5. 39-47.

Russell, D.G. 2007b. Who puts the tubercle in tuberculosis? *Nat. Rev. Microbiol.* 5:39-47.

Sanjuan, M.A., C.P. Dillon, S.W.G. Tait, S. Moshiach, F. Dorsey, S. Connell, M. Komatsu, K. Tanaka, J.L. Cleveland, S. Withoff, and D.R. Green. 2007. Toll-like receptor signalling in macrophages links the autophagy pathway to phagocytosis. *Nature*. 450:1253-1257.

Sanjuan, M.A., S. Milasta, and D.R. Green. 2009. Toll-like receptor signaling in the lysosomal pathways. *Immunological Reviews*. 227:203-220.

Schindelin, J., I. Arganda-Carreras, E. Frise, V. Kaynig, M. Longair, T. Pietzsch, S. Preibisch, C. Rueden, S. Saalfeld, B. Schmid, J.-Y. Tinevez, D.J. White, V. Hartenstein, K. Eliceiri, P. Tomancak, and A. Cardona. 2012. Fiji: an open-source platform for biological-image analysis. *In* Nat Meth. Vol. 9. 676-682.

Schworer, C.M., K.A. Shiffer, and G.E. Mortimore. 1981. Quantitative relationship between autophagy and proteolysis during graded amino acid deprivation in perfused rat liver. *J Biol Chem*. 256:7652-7658.

Stamm, L.M., and E.J. Brown. 2004. Mycobacterium marinum: the generalization and specialization of a pathogenic mycobacterium. *In* Microbes Infect. Vol. 6. 1418-1428.

Stamm, L.M., J.H. Morisaki, L.-Y. Gao, R.L. Jeng, K.L. McDonald, R. Roth, S. Takeshita, J. Heuser, M.D. Welch, and E.J. Brown. 2003a. Mycobacterium marinum escapes from phagosomes and is propelled by actin-based motility. *J. Exp. Med.* 198:1361-1368.

Stamm, L.M., J.H. Morisaki, L.-Y. Gao, R.L. Jeng, K.L. McDonald, R. Roth, S. Takeshita, J. Heuser, M.D. Welch, and E.J. Brown. 2003b. Mycobacterium marinum escapes from phagosomes and is propelled by actin-based motility. *In* J. Exp. Med. Vol. 198. 1361-1368.

Strack, R.L., B. Hein, D. Bhattacharyya, S.W. Hell, R.J. Keenan, and B.S. Glick. 2009. A rapidly maturing far-red derivative of DsRed-Express2 for whole-cell labeling. *In* Biochemistry. Vol. 48. 8279-8281.

Tobin, D.M., and L. Ramakrishnan. 2008. Comparative pathogenesis of Mycobacterium marinum and Mycobacterium tuberculosis. *In* Cellular Microbiology. Vol. 10. 1027-1039.

van der Vaart, M., H.P. Spaink, and A.H. Meijer. 2012. Pathogen recognition and activation of the innate immune response in zebrafish. *In* Adv Hematol. Vol. 2012. 159807.

van der Wel, N., D. Hava, D. Houben, D. Fluitsma, M. van Zon, J. Pierson, M. Brenner, and P.J. Peters. 2007. M. tuberculosis and M. leprae Translocate from the Phagolysosome to the Cytosol in Myeloid Cells. *In* Cell. Vol. 129. 1287-1298.

Wager, K., and C. Russell. 2013. Mitophagy and neurodegeneration: The zebrafish model system. *In* autophagy. Vol. 9.

Watson, R.O., P.S. Manzanillo, and J.S. Cox. 2012. Extracellular M. tuberculosis DNA targets bacteria for autophagy by activating the host DNA-sensing pathway. *In* Cell. Vol. 150. 803-815.

Yang, Z., and D.J. Klionsky. 2010. Eaten alive: a history of macroautophagy. *In* Nature Publishing Group. Vol. 12. Nature Publishing Group. 814-822.

Supplementary information

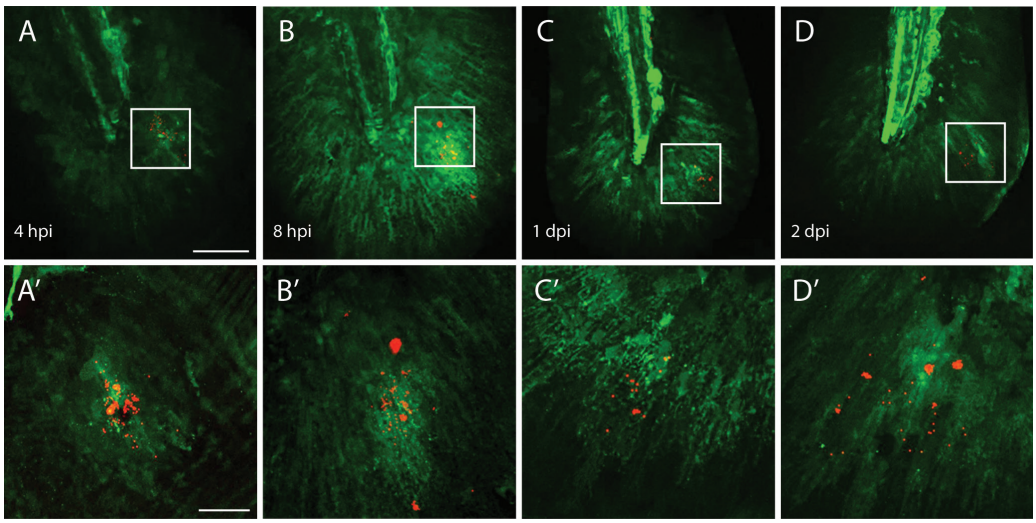

Figure S1. Autophagy is induced after injection of beads. *Tg(CMV:EGFP-map1lc3b)* larvae injected with polystyrene beads (Ø≈1.2 µm) were imaged at different time points. (**A and B**) GFP-Lc3-positive vesicles (green) were observed at 2 hpi and 8 hpi in response to the injection of the beads (red). (**C and D**) At the site of injection a similar number of GFP-Lc3-positive vesicles (green) were observed compared to the surrounding tissue. From these images it is not clear in which cell type these vesicles occur. (**A to D**) An overview of the entire tail fin imaged at a low magnification is shown in the top panels. (**A' to D'**) The indicated region in (**A to D**) imaged at higher magnification is presented in the bottom panels. Scale bars: 100 µm for the images in the top panels and 20 µm for images in the bottom panels. For each time point, approximately 15 larvae were imaged and representative images for each time point are shown.

Movie S1. GFP-Lc3 vesicle fusing with another compartment containing *M. marinum*. *Tg(CMV:EGFP-map1lc3b)* larvae infected with *M. marinum* were imaged alive every ~23 sec at 1 dpi by CLSM. A GFP-Lc3-positive (green) vesicle was observed in close vicinity of bacteria (indicated by the first arrow). This vesicle fuses with the *M. marinum* (red) containing compartment. This compartment may be phagosomal or autophagic in nature. This process was observed as a diffuse GFP-Lc3 signal surrounding the bacteria, which appears immediately after disappearance of the initial small GFP-Lc3-positive vesicle (indicated by the second arrow). Note that the GFP-Lc3 signal surrounding the bacterial compartment disappears again and that after the fusion process another GFP-Lc3 vesicle was observed. The maximum intensity projection from 9 CLSM images (step size in z-direction, 1.56 µm) is shown at 10 frames per second. Scale bar: 2 µm.

Movie S2. Fusion between GFP-Lc3-positive vesicles in vicinity of *M. marinum*. *Tg(CMV:EGFP-map1lc3b)* larvae infected with *M. marinum* were imaged alive every ~23 sec at 2 dpi by CLSM. The GFP-Lc3-positive (green) vesicles indicated by arrows were observed in close vicinity of bacteria. These vesicles fuse together and the relevance of this process to the infection process is unclear. The GFP-Lc3-positive vesicles could be involved in non-bacterial autophagy, and may play a role in the clearance of phagosomal membranes that have been damaged during the escape of *M. marinum*. Fusion with a compartment containing the bacterium (red) is not observed, which may be due to the fact that the bacterium is cytosolic. The maximum intensity projection from 9 CLSM images (step size in z-direction, 1.56 µm) is shown at 10 frames per second. Scale bar: 2 µm.

CHAPTER 3

DYNAMIC INTERACTION BETWEEN LEUKOCYTES DETERMINES THE PROGRESSION OF INFECTION DURING EARLY MYCOBACTERIAL PATHOGENESIS

Rohola Hosseini, Gerda E. M. Lamers, Hiwa M. Soltani, Annemarie H. Meijer, Herman P. Spaink, Marcel J. M. Schaaf

Submitted

Abstract

Macrophages and neutrophils are the first cellular responders against invading pathogens and contribute strongly to the host defense against intracellular pathogens. The collective interplay and dynamic interactions between these leukocytes are to a large extent uncomprehended, and in the present study we have investigated their role using a combination of confocal laser scanning and electron microscopy in a zebrafish model for tuberculosis, a local *Mycobacterium marinum* (*Mm*) infection in the tail fin. Our results show that neutrophils are efficient in phagocytosis of *Mm* and that they contribute largely to the dissemination of bacteria. Macrophages appear to play a major role in efferocytosis, phagocytosis of dead cells that contain bacterial content. Eventually, large bacterial aggregates inside phagocytic cells are formed due to continuous efferocytosis, and they can be extruded out of the tail fin. Alternatively, the macrophages containing these aggregates may undergo burst. Thus, here we show the specific key functions of macrophages and neutrophils during the progression of early *Mm* infection.

Introduction

Macrophages and neutrophils are the first cells responding to invading pathogens, and during the early stages of mycobacterial infection they are the main cell types to be infected (Silva et al., 1989; Eum et al., 2010). Although macrophages are the main cell type associated with mycobacterial infection, a growing body of evidence is showing that other phagocytic cells play a major role during mycobacterial infection as well (Berry et al., 2010; Nouailles et al., 2014; Srivastava et al., 2014; Eum et al., 2010). Especially neutrophils, which are often the first responders in the host defense towards invading pathogens, appear to play a crucial protective role during a mycobacterial infection, for example by producing reactive oxygen and nitrogen species (Elks et al., 2013; Yang et al., 2008; 2012). However, how macrophages and neutrophils collectively interplay and their specific dynamic interactions during the host response against intracellular pathogens is still unclear. The present study focuses on the quantification and high resolution imaging of macrophage and neutrophil function and dynamics and during mycobacterial infection. This is required for the understanding of the specific role of infected macrophages and neutrophils play during infection and their distinct contribution to the host-defense and bacterial dissemination.

Studying the early stages of mycobacterial infections in zebrafish has been an effective approach to study host-pathogen interactions. In the present study, we have used the fish pathogen *M. marinum* (*Mm*), a close relative of *M. tuberculosis* (*Mtb*), the causative agent of tuberculosis in humans, to investigate the complex dynamic response of leukocytes towards mycobacterial infection. *Mm* displays a similar pathogenesis in zebrafish as *Mtb* in humans, including the formation of granulomas (Swaim et al., 2006; Ramakrishnan, 2012), providing an interesting model system for studies on the pathogenesis of tuberculosis (Ramakrishnan, 2013; Cronan and Tobin, 2014; Torraca et al., 2014). We have utilized the previously described zebrafish tail fin infection model (Hosseini et al., 2014), which enables us to visualize the entire infection process from the first infected cells to the formation of early granuloma structures. For this purpose, time lapse confocal laser scanning microscopy (CLSM) in combination with advanced 3D block-face scanning electron microscopy (SBF-SEM) were used.

Results and discussion

Zebrafish larvae were infected with ~ 50 colony forming units (cfu) *M. marinum* (*Mm*) in the tail fin at 3 days post fertilization (dpf). We used larvae from a

transgenic line, *Tg(mpeg1:eGFP) X Tg(lys:DsRed)*, which displays green and red fluorescent of macrophages and neutrophils respectively (Ellett et al., 2011; Hall et al., 2007). Injection of *Mm* in the tail fin induces a localized infection, which attracts neutrophils and macrophages to the site of infection, and develops into a granuloma-like structure within 5 days post infection (dpi) (Fig. 1A) (Hosseini et al., 2014). Under basal conditions, the tail fin consists of two epithelial cell layers on both sides with mesenchyme cells in between and no leukocytes are normally found there (Kimmel et al., 1995). In order to provide a detailed description of the infection process and the host response, time-lapse imaging using confocal laser scanning microscopy (CLSM) was performed.

Bacterial burden and leukocyte recruitment

The bacterial burden and the number of macrophages and neutrophils recruited to the site of infection was quantified at 1, 6, 12 hours post infection (hpi) and at 1, 2, 3, 4 and 5 dpi (Fig. 1B-D). Representative images for these time points are shown in Fig. 1B. The bacterial burden does not change between 1 hpi and 1dpi, but increases significantly between 1 and 3 dpi after which it remains unchanged until 5 dpi (Fig. 1C). Upon infection, the number of recruited macrophages remains constant (at approximately 3) until 1 dpi, whereas the number of neutrophils decreases significantly from 4.2 (± 0.3) at 1 hpi to 1.1 (± 0.3) at 12 hpi (Fig. 1C). At this time point, the macrophages are the main type of leukocyte present at the site of infection and the majority of these macrophages (~72%) were infected with *Mm*. After this time point, both the number of macrophages and neutrophils increases dramatically and they remain constant after 4 dpi (Fig. 1C). Based on the bacterial burden at the site of infection, three different phases of the mycobacterial infection can be distinguished, the lag, exponential and stationary phase (Fig. 1E).

The lag phase of infection

To investigate the lag phase of infection, image sequences acquired using time-lapse microscopy were analyzed in detail focusing on leukocytes dynamics and cell death (Fig. 2, Suppl. Video 1). Figure 2A shows representative images of several time points during the lag phase of infection. These images show that during this lag phase the bacterial burden remains constant, the number of neutrophils decreases steadily and the number of macrophages remains constant but shows large fluctuations.

Using these image sequences the trajectories of the macrophages and neutrophils were analyzed until they had moved out of the image frame or had undergone cell death. The infected macrophages and neutrophils show short trajectories and the vast majority of these cells (~84%) remain local in the tail fin (Fig. 2B, 2C). A fraction of infected macrophages and neutrophils was observed to migrate away from the infection

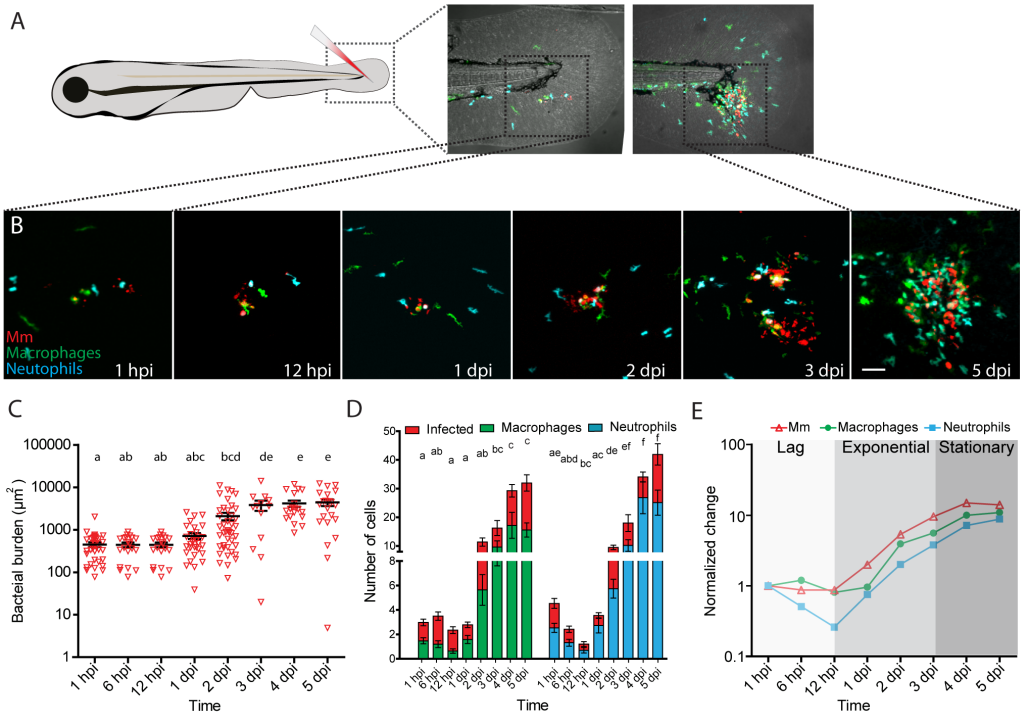

Fig. 1. Mycobacterium marinum infection in the zebrafish tail fin. A) Schematic image showing the location in the tail fin where Mm was injected into zebrafish larvae at 3 dpf. **B)** Representative CLSM images of the infection site in the tail fin at different time points. **C)** Quantification of the bacterial burden at different time points after Mm infection. **D)** Numbers of recruited macrophages (green) and neutrophils (blue) to the site of infection and their infected fractions (red) per larva. **E)** Normalized bacterial burden and numbers of recruited leukocytes (relative to 1 hpi). The analysis shows that based on the bacterial burden, the course of infection can be divided into three different phases: the lag, exponential and stationary phase. Error bars indicate standard error of the mean, n~20 larvae per timepoint. Means with the same letter do not differ significantly (Dunnett's post-test, $P<0.05$). Scale bar: 50 µm.

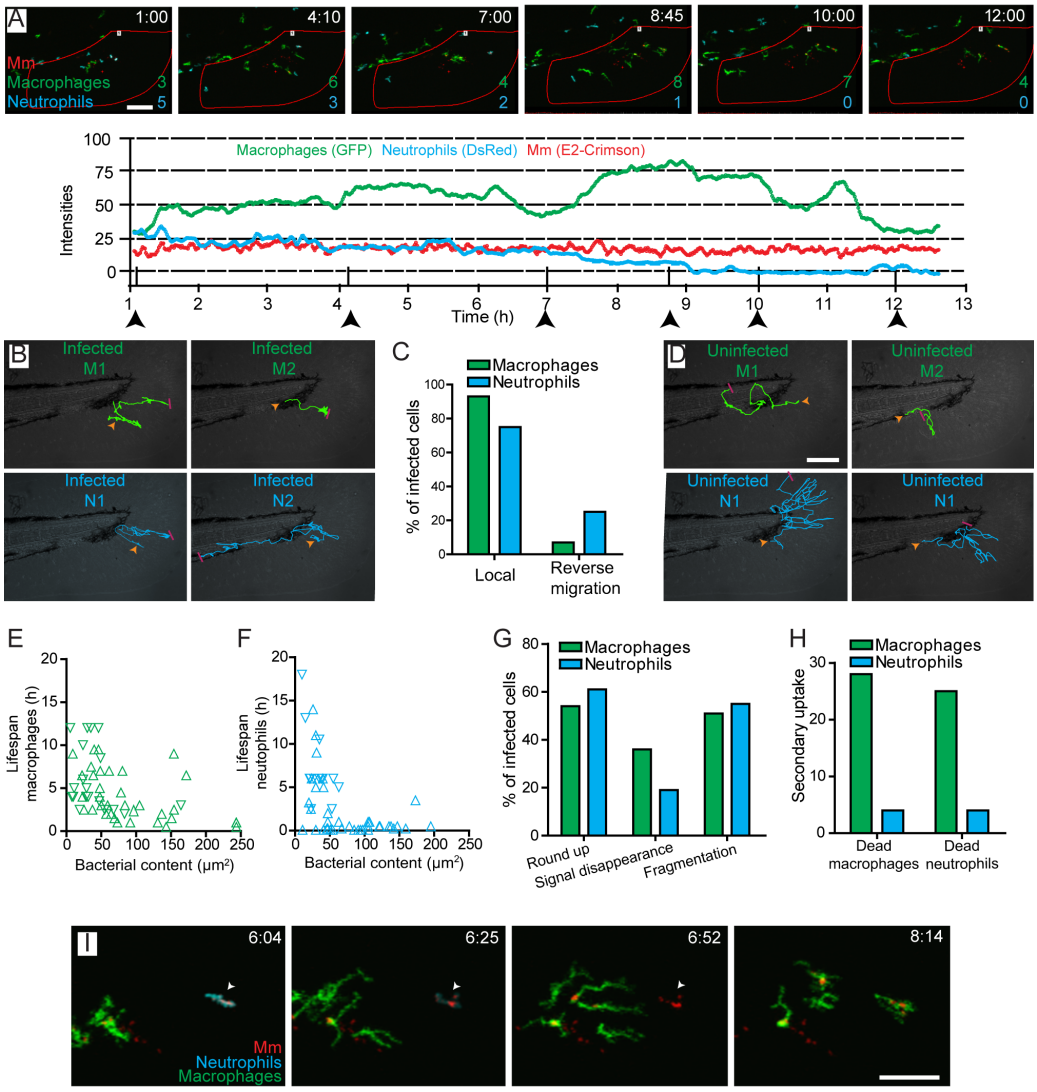

Fig. 2. Accumulation of Mm in macrophages occurs through cell death and secondary uptake by macrophages at the site of infection. A) Intensity profiles for macrophages (green), neutrophils (blue) and Mm (red) at the site of infection in a representative larva, showing dynamic recruitment and resolution of leukocytes. For time points indicated by the arrowheads corresponding images are shown, in which the numbers of leukocytes present within the region of interest (shown in red) are indicated . **B)** Representative trajectories of infected leukocytes. Macrophage 1 and neutrophil 1 show short local trajectories in the tail fin. Macrophage 2 was recruited to the site of infection and remains at the same position after phagocytosis of Mm. Neutrophil 2 showed reverse migration along the caudal vein. **C)** Percentages of leukocytes showing local and reverse migration. **D)** Representative trajectories of uninfected macrophages (green) and neutrophils (blue). The macrophages show short trajectories into and out of the tail fin, while the neutrophils show longer trajectories in the

tail fin before going out. **E and F)** Lifespan of infected leukocytes as a function of the infection size at the lag phase of infection. **G)** Percentages of infected leukocytes undergoing cell death showing different morphologies. **H)** Phagocytosis of bacterial content of leukocytes that have undergone cell death by macrophages and neutrophils. **I)** Representative frames from time-lapse imaging showing phagocytosis by a macrophage of bacterial content, which was initially sequestered inside a neutrophil. Scale bars: 50 μm.

site (Fig. 2C; infected N2). This reverse migration was observed for ~25% of all infected neutrophils compared to only ~7% of all infected macrophages (Fig 2C). Generally, these leukocytes migrate along the caudal vein (marked in Fig. 2C as infected N2) and were not observed to intravasate the caudal vein. Uninfected macrophages show short trajectories towards and away from the infection site, whereas neutrophils show longer trajectories covering a large area of the tail fin (Fig. 2D).

The role of macrophages in the dissemination of mycobacterial infections is well known, but the role of neutrophils is unclear (Davis and Ramakrishnan, 2009). A study in a murine infection model suggested that an attenuated *M. bovis* strain (BCG) after phagocytosis by neutrophil migrate via afferent lymphatics to lymphoid tissue and can spread bacterial infection (Abadie et al., 2005). Recent studies in a zebrafish larval infection model in which *E. coli* were injected subcutaneously, demonstrated phagocytosis of pathogens (including *Mm*) by neutrophils to be tissue-dependent,. (Colucci-Guyon et al., 2011; Belon et al., 2014). However, it was not observed upon injection of *Mm* into the bloodstream or the hindbrain of zebrafish larvae (Yang et al., 2012; Cui et al., 2011; Davis et al., 2002). Here we show that neutrophils can efficiently phagocytize mycobacteria at the initial infection site, and undergo reverse migration more frequent than macrophages. Due to their high mobility, neutrophils may disseminate bacteria further in the host than macrophages.

The lifespan of leukocytes is dependent on infection quantity

The image sequences were additionally used to determine the lifespan of neutrophils and macrophages after infection. Infected macrophages have an average lifespan of 4.8 (± 0.5) hours compared to 3.1 (± 0.6) for neutrophils. The bacterial content of these cells appears to correlate with their lifespan (Fig. 2E-F) showing that the higher the bacterial content the shorter their lifespan. For macrophages the lifespan shows a continuum, whereas for neutrophils we found a bimodal distribution. The majority of infected neutrophils have a very short lifespan (<1 h), and have a bacterial content larger than ~50 μm^2. Neutrophils with a smaller bacterial content have a longer lifespan.

Different morphologies of cell death

We show that infected leukocytes undergo massive cell death, which here is defined as a disappearance of the fluorescent signal. We could distinguish three different patterns for leukocytes undergo cell death, based on the fluorescent signal (Fig. 2G, Suppl. Fig. 1). The majority of leukocytes undergoing cell death display a round morphology before signal disappearance (54% macrophages, 61% neutrophils). The time between rounding up and signal disappearance varies from a few minutes to several hours. The second way of cell death we observed was fragmentation of the cell into several compartments, of which at least one contained bacteria. The fluorescent signal of these compartments disappeared at different rates, ranging from few minutes to hours. 51% of macrophages and 54% of neutrophils displayed this form of cell death. The third pattern of cell death was characterized by a rapid signal disappearance. In these leukocytes the fluorescent signal disappears within few minutes after ingestion of bacteria (suppl. Fig. 1B). 36% of macrophages and 19% of neutrophils underwent this form of cell death.

Phagocytosis of dead cells by macrophages

Regardless of the type of cell death of infected leukocytes, secondary uptake of the bacterial content was performed by the macrophages in most cases. This secondary uptake most likely includes phagocytosis of the remains of the dying or dead cells, which is called efferocytosis (Martin et al., 2014). The secondary uptake of bacterial content was observed to be phagocytized by macrophages in 87% of the cases, regardless of whether these bacteria had initially been sequestered by macrophages or neutrophils (Fig 2G). In the remaining ~13% of the cases this efferocytosis was carried out by neutrophils. In Figure 2I an example is shown of efferocytosis by a macrophage taking up an infected neutrophil which has undergone cell death (as shown by the rapid fluorescent signal disappearance).

Exponential phase of infection: 12 hours to 3 days post infection

At the beginning of this phase (12 hpi) the bacterial infection is mainly present in macrophages due to continuous neutrophilic cell death and efferocytosis during the lag phase. In order to study the progression of the infection from 12 hpi to 2 dpi, we analyzed time-lapse recordings for this period. Two events are characteristic for the infection process after 12 hpi: macrophage burst and extrusion of bacteria (Fig. 3).

Macrophage burst events

In our study, macrophage burst events were defined as large compacted bacterial aggregates inside macrophages that spread to the surrounding tissue, probably due to cell death-induced rupture of the membranes surrounding the bacteria (Repasy

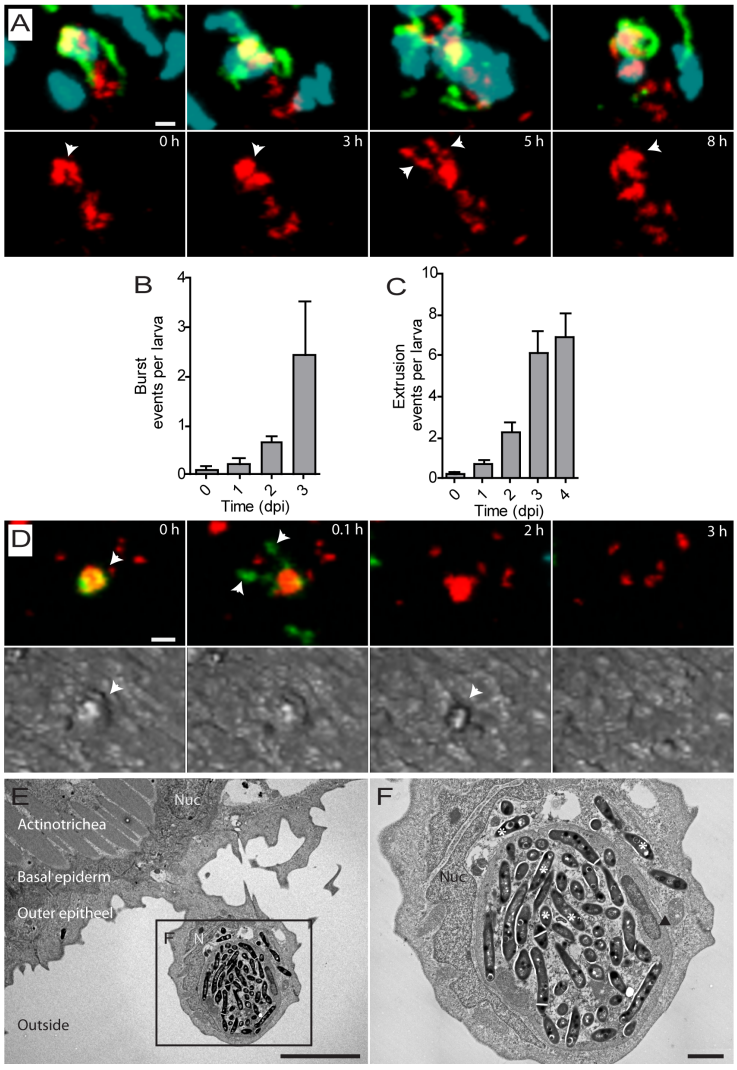

Fig. 3. Macrophages containing aggregates of Mm undergo burst or extrusion. A) Representative images from live cell imaging of a large aggregate of Mm (arrowhead) inside a macrophage (arrow) undergoing cell death at t=3h. Spreading of Mm was observed at t=5h. The aggregate was compacted again by newly recruited leukocytes at t=8h (see also Video 2.mov). **B)** Number of burst events observed at different time points after Mm infection in the tail fin. **C)** Number of extrusion events observed at different time points after Mm infection in the tail fin. **D)** Representative images from live cell imaging showing an extrusion event of accumulated Mm in a macrophage. First, the macrophage undergoes cell death and subsequently after 3 hours the bacterial content is extruded. **E)** TEM image of an extruding epithelial cell from the tail fin surrounding a dead cell containing a large aggregate of Mm. The two epithelial layers and actinotrichia collagens are indicated. **F)** Higher magnification of the region indicated in E, showing compact aggregates of Mm (asterisks) in the dead cell with a condensed nucleus (arrow head). Error bas indicate SEM. Scale bars in A, C and E: 10 µm; in F: 2 µm.

et al., 2013). Subsequently, the spread bacteria are taken up by neutrophils and macrophages. An example of such a burst event imaged using time-lapse CLSM is shown in Fig. 3A and Video 2. The number of burst events increases dramatically between 1 and 3 dpi, from 0.1 (±0.08) to 2.4 (±1.1) burst events per larva. This is probably due to the increased bacterial burden per cell.

Extrusion of *Mm* aggregates

Interestingly, large aggregates of bacteria were also observed to be extruded out of the tail fin. The frequency of these extrusion events had significantly increased between 1 and 3 dpi, from 0.8 (±0.1) to 6.9 (±1.1) extrusion events per larva (Fig. 3C). An example of an extrusion event imaged using time-lapse CLSM is shown in Fig. 3D and Video 3. As in most cases, in this example the bacterial content was initially present in a macrophage, and was extruded 2 to 3 hours after disappearance of the fluorescent signal of the macrophage. These extrusion events were not exclusively observed upon cell death of macrophages, but occur occasionally after neutrophil cell death as well. The extruded bacterial aggregate displays itself first as a protuberance on the outer epithelial layer of the tail fin, which could be observed using brightfield/DIC microscopy (Fig. 3D). The ultrastructure of such a protuberance was imaged using TEM (Fig. 3E-F). These images show a bacterial aggregate shortly before an extrusion event. A cell of the outer epithelial layer contains a dead cell with a large bacterial aggregate, and is in the process of being extruded from the epithelial layer.

Extrusion of dead or infected epithelial cells is important for the preservation of the epithelial barrier (Gu and Rosenblatt, 2012; Eisenhoffer et al., 2012). Apical extrusion of Salmonella-infected epithelial cells into the lumen has been observed in the gall bladder of infected mice (Knodler et al., 2010). To our knowledge this process has not been shown for mycobacterium infection. The role of extrusion by lung epithelium is still unclear. In the case of *Mtb* infection that primarily affects the lungs in humans, this process might represent an important mechanism in the clearance of *Mtb*. Alternatively, mycobacteria inside extruded cells could be used by the pathogen as a strategy for avoiding the pro-inflammatory response and dissemination from human to human.

Stationary phase of infection: 3 days post infection

The stationary phase of larval infection is characterized by granuloma-like structures containing a large number of macrophages and neutrophils at the site of infection. In addition, at this phase we observe secondary granuloma-like structures (suppl. Fig. 2), which are most often observed near the caudal vein. Additionally, at this phase extrusion occurs at a large scale and the bacterial content of several cells were observed to be simultaneously extruded.

Ultrastructure of infected macrophages and neutrophils

In order to get a deeper understanding of cellular processes ongoing in the infected leukocytes observed during time-lapses, infected larvae were analyzed using EM. We used 3D block-face SEM to obtain a 3D EM image of the region of the infected tail fin at 3 dpi (Video 4). In this technique, EM images are acquired from the surface of the tissue sample. Subsequently, a 100 nm layer is removed and a new image of the surface is acquired (Denk and Horstmann, 2004; Peddie and Collinson, 2014). To correlate these 3D EM images with the images obtained by CLSM, the bacteria observed in the EM images were aligned with the fluorescent signal of *Mm* acquired by CLSM (Suppl. Fig.2). By aligning the images acquired by the two techniques, the fluorescently labeled macrophages and neutrophils were identified in EM images (Fig. 4A-B). Using this approach the EM images of the infected macrophages and neutrophils could not only be correlated with the CLSM images, but could also be linked to the dynamic behavior of these cells in the previous hours (Video 5).

The images of two infected macrophages and two infected neutrophils were correlated (indicated in Fig. 4A-B). The EM image of the first macrophage shows clear chromatin condensation in the nucleus indicating that this cell is undergoing apoptosis (Fig. 4D). The confocal images show that this cell has phagocytized a large aggregate of bacteria ~30 minutes earlier (Fig.4C). Although mycobacteria are notorious for their ability to block apoptosis (Lee et al., 2006; Repasy et al., 2013), here we show that macrophages with a large bacterial content, most likely acquired by efferocytosis, may undergo apoptosis (Fig. 4D). In addition, infected macrophages showing clear fragmentation, another hallmark of apoptotic cell death, was observed using light microscopy (Fig. 2G, Suppl. Fig. 1D). The second imaged macrophage contains a single compartment containing a bacterial aggregate and remains of dead cells (Fig 4D). The confocal images show that this macrophage had phagocytized the aggregate ~1.5 hour earlier and no sign of cell death is shown yet in the EM image (Fig. 4C).

The first imaged neutrophil displays a necrotic morphology, characterized by a round nucleus and an irregularly shaped plasma membrane and no apoptotic features (Fink and Cookson, 2005). In the confocal images this neutrophil showed a compacted bacterial content at the start of the time-lapse and a disappearance of the fluorescent signal (within 1 min) approximately 30 minutes before fixation (Fig 4C). Based on light microscopy observations, the rapid signal disappearance of uninfected neutrophils was previously suggested to be apoptosis (Loynes et al., 2010). However, based on these correlated light and EM images, we suggest that the type of cell death characterized by a rapid disappearance of the fluorescent signal (<1 minute) is a form of necrotic cell death. By fusion of lysosomal compartments with the cytoplasm (Artal-Sanz et al., 2006) and probably the release of abundant peroxides present in neutrophils, necrotic cells may lose their fluorescence due to a rapid denaturation

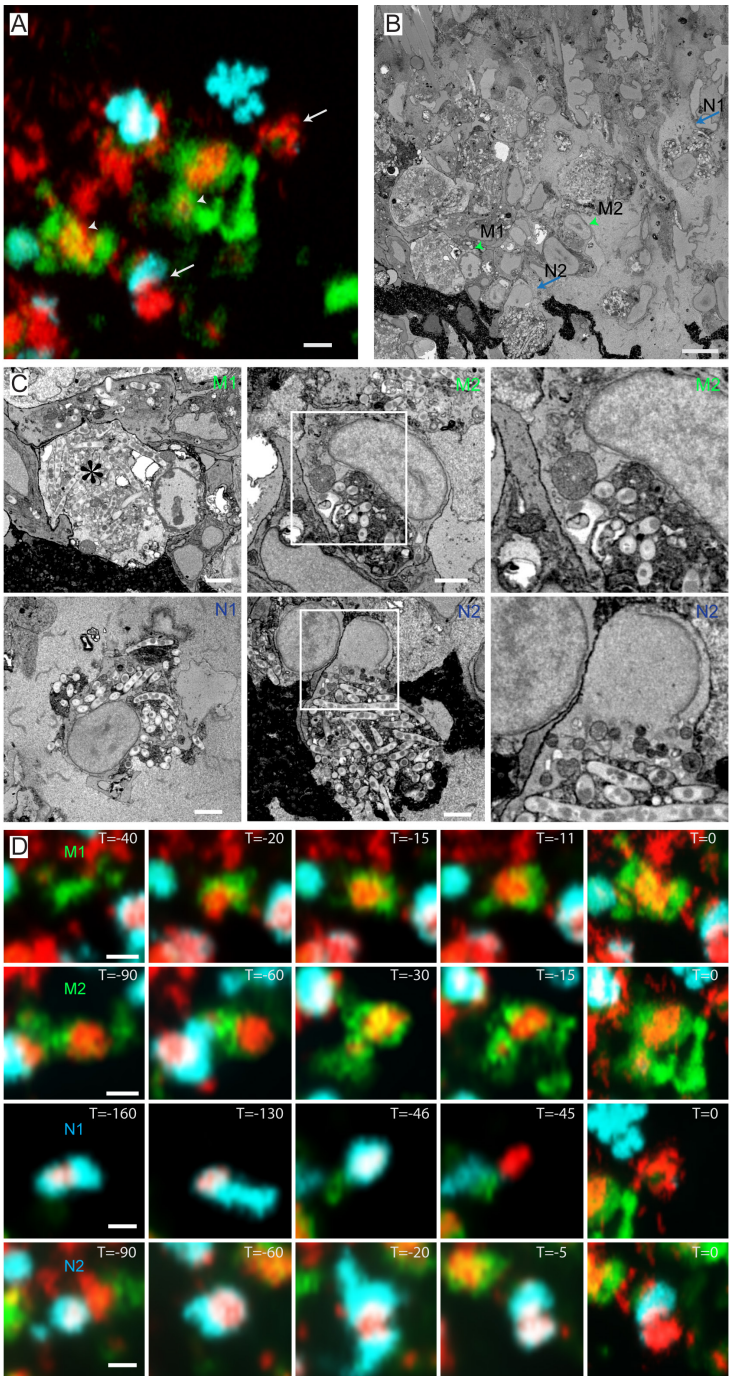

Fig. 4. Ultrastructure of correlated macrophages and neutrophils in 3D block-face SEM images. A) High resolution CLSM image of an infected tail fin after live cell imaging and fixation. **B)** BF-SEM image of the same region in (A) showing correlated macrophages (arrowheads) and neutrophils (arrows). **C)** Higher magnification BF-SEM images of the two macrophages and two neutrophils indicated in A and B. **D)** Frames from time-lapse imaging showing the macrophages and neutrophils in (C) at previous time points. The early stage apoptotic macrophage (M1) contains a high Mm content indicated by asterisk in (C). This macrophage phagocytized the bacterial content ~30 minutes before fixation. Macrophage (M2) contains a large aggregate of Mm which was phagocytized Mm ~1,5 hours before fixation. Neutrophil (N1) showed rapid signal disappearance ~45 minutes before the fixation (D). Neutrophil (N2) was recruited to the bacterial aggregate ~ 30 minutes before fixation (D). Scale bars: A-C, 10 µm; D, 2 µm.

of the fluorescent proteins. The second imaged neutrophil has not entirely engulfed the bacterial aggregate. Instead, this neutrophil seems to be in a process called netosis (Francis et al., 2014). It shows a nuclear membrane that is not intact and granules at the plasma membrane fusing with the extracellular space, in which a large aggregate of bacteria is located (Fig 4D and Video 6). In confocal images this cell was observed to be interacting with a large aggregate of *Mm* in the preceding 30 min, which was previously contained by another neutrophil (Fig 4C). Netosis is often associated with necrotic infected neutrophils (Francis et al., 2014). Neutrophils are able to sense microbe size and selectively release extracellular traps in response to large pathogens, such as *Candida albicans* hyphae and extracellular aggregates of *Mycobacterium bovis* (Branzk et al., 2014).

In the BF-SEM images we also observed *Mm* infected epithelial cells in the process of undergoing extrusion (Suppl. Fig.2D). These cells did not show a fluorescent signal associated with macrophages or neutrophils. Using 3D information provided by this method, we could observe that the bacterial aggregate was entirely contained within an epithelial cell. The presence of a bacterial aggregate inside an epithelial cell indicates bacterial uptake at the basal side of the cell (probably by efferocytosis), which subsequently undergoes extrusion at the apical side.

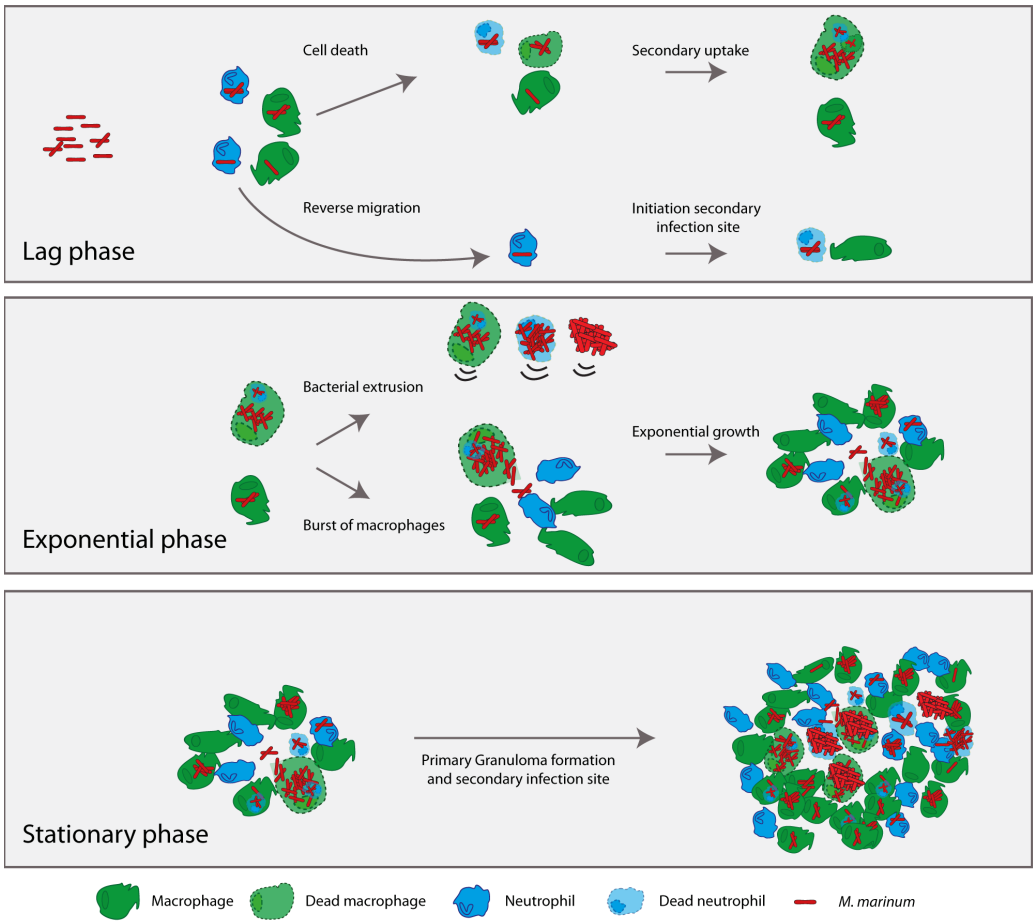

Fig. 5. Overview of Mm infection in the tail fin of zebrafish larvae. This overview summarizes the processes taking place during the course of infection.

Conclusions

In the present study we show the specific key functions of macrophages and neutrophils during the dynamic infection process of *Mm* in zebrafish larvae. In Figure 5 a schematic overview is shown of the cellular processes during the different phases of early granuloma development observed in this study.

Following the dynamics of the leukocytes during the course of infection, we found that many macrophages and neutrophils undergo cell death during the process of infection. As a result the number of leukocytes involved in the infection process will be underestimated when single time points are investigated. We show that the neutrophils are efficient in phagocytosis of *Mm* and contribute largely to

the dissemination of the bacteria. The macrophages appear to play a major role in efferocytosis of dead infected macrophages and neutrophils. Continuous efferocytosis by macrophages results in high bacterial contents in these cells, resulting in burst of macrophages when they are unable to retain the pathogen. Finally, epithelially mediated extrusion of the bacterial content after efferocytosis of infected leukocytes was observed to contribute to bacterial clearance.

Materials and Methods

Zebrafish strains and maintenance

Zebrafish were handled in compliance with the local animal welfare regulations and maintained according to standard protocols (www.zfin.org). The ABTL wild type zebrafish strain and the transgenic lines, *Tg(mpeg1:eGFP),* and *Tg(lys:DsRed),* strains were used for this study. All fish were raised and grown at 28.5 °C on a 14 h light : 10 h dark cycle. Embryos were obtained from natural spawning at the beginning of the light period and kept in egg water (60 µg/ml Instant Ocean sea salts).

Zebrafish tail fin infection

The *M. marinum* M strain fluorescently labeled with E2-crimson was used and prepared at ~500 colony-forming units per 1 nl as previously described (Benard et al., 2012). Borosilicate glass micro capillaries (Harvard Apparatus, 300038) were used with a micropipette puller device (Sutter Instruments Inc.) for preparing microinjection needles. Zebrafish larvae were injected in the tail fin at 3 dpf using the Eppendorf microinjection system with a fine (~5 to 10 micron) needle tip broken off with tweezers and mounted at a 30-degree angle. Larvae were anesthetized in egg water with 200 µg/mL 3-aminobenzoic acid (Tricaine; Sigma-Aldrich, E10521) and injected between the two epidermal layers at the ventral part of the tail fin (Fig. 1).

Confocal laser scanning microscopy

Larvae were anesthetized with 200 µg/ml tricane and mounted in 0.7% low melting agarose (Sigma-Aldrich, A9414) and imaged with the Nikon A1 confocal laser scanning microscope (Tokyo, Japan) using the 488, 561 and 641 laser lines with 20X (NA 0.75). Images were analyzed using NIS-Elements analysis software. The bacterial burden was analyzed on the max-projection images (12 bit), binary areas were created based on the *M. marinum* fluorescent signal using a threshold

above 900 for the larvae at 0 dpi to 2 dpi and threshold above 1700 for larvae from 3 dpi to 5 dpi. The number of macrophages and neutrophils and all the events were counted manually. The tracks were generated using Nis elements 4 (Nikon software) and manually corrected miss matched tracks. The macrophage and neutrophil interactions during infection 225 larvae were imaged at ~60 seconds per frame for 18 hours at 28.5 degrees. For the lag fase 33 larvae were analyzed (n= 70 macrophages and 70 neutrophils) between 6 and 18 hours, larvae moved out of view in less than 6 hours were removed from analyses. For the exponential phase 60 larvae and for the stationary phase 40 larvae were analyzed. The clearly observable macrophage burst events were counted manually and the bacterial extrusion events were scored manually to a maximum of 10 events per larva based on bacterial content released from the tissue.

Transmission electron microscopy

Before being used for electron microscopy the zebrafish larvae were anesthetized with 200 µg/ml tricaine and fixated in 2% glutaraldehyde and 2% paraformaldehyde in sodium cacodylate buffer (pH 7.2) for 3 h at room temperature followed by fixation for 16 h at 4 °C. Post fixation was performed in 1% osmium tetroxide in sodium cacodylate buffer for 1 h at room temperature. After dehydration through a graded series of ethanol all specimens were kept in epoxy resin (Agar Scientific, AGR1043) for 16 h before embedding. Ultrathin sections were collected on Formvar coated one hole copper grids (Agar Scientific, AGS162) stained with 2% uranyl acetate in 50% ethanol and lead citrate for 10 min each. Electron microscopy images were obtained with a JEOL JEM-1010 transmission electron microscope (Tokyo, Japan) equipped with an Olympus Megaview camera (Tokyo, Japan).

Block-Face scanning electron microscopy

The larvae were prepared using a protocol modified from (Deerinck et al., 2010). Before being used for block-face scanning electron microscopy the zebrafish larvae were anesthetized with 200 µg/ml tricaine, imaged alive by CLSM and afterwards immediately fixated in 0.5% glutaraldehyde and 2% paraformaldehyde in PHEM buffer (pH 6.9) for 2 h at room temperature followed by fixation in 2% glutaraldehyde and 2% paraformaldehyde in sodium cacodylate buffer (pH 7.2) for 16 h at 4 °C. Postfixation was performed in 1:1 4% Osmium tertroxide : 3% K Ferrocyanide in 0,3 M Na cacodylate buffer (pH 7,2), 20 min 1 % ThioCarboHydrazide (TCH), 30 min 2% Osmium tertroxide, 1 hr 1% Uranyl Acetate and 30 min Waltons Lead aspartate at 60°C. After dehydration through a graded series of ethanol all specimens were kept in epoxy resin (Agar Scientific, AGR1043) for 16 h before embedding. Blocks were trimmed and glued on a cryopin and examined in a Quanta FEG 250 with a Gatan 3View Ultramicrotome module using the BSE mode to perform 3D block-face

images by cutting 150 nm sections. The data was segmented and aligned with CLSM images using Amira 3.5 (FEI, USA) software.

Statistical analysis

All data were analyzed (Prism version 5.0, GraphPad Software) using one-way analysis of variance (ANOVA) with Dunnett's post-test for multiple groups. Error bars represent mean ± SEM, statistical significance was assumed at *p*-value below 0.05.

Acknowledgements

We thank Tobias Starborg (University of Manchester) for technical assistant and Bram Koster (LUMC) for helpful discussion. Infectious disease research in our laboratory is supported by the European Commission 7th framework project ZF-HEALTH (HEALTH-F4-2010-242048) and the Cyttron II Program (LSH framework: FES0908).

References

Abadie, V., E. Badell, P. Douillard, D. Ensergueix, P.J.M. Leenen, M. Tanguy, L. Fiette, S. Saeland, B. Gicquel, and N. Winter. 2005. Neutrophils rapidly migrate via lymphatics after Mycobacterium bovis BCG intradermal vaccination and shuttle live bacilli to the draining lymph nodes. *Blood*. 106:1843–1850. doi:10.1182/blood-2005-03-1281.

Artal-Sanz, M., C. Samara, P. Syntichaki, and N. Tavernarakis. 2006. Lysosomal biogenesis and function is critical for necrotic cell death in Caenorhabditis elegans. *The Journal of Cell Biology*. 173:231–239. doi:10.1083/jcb.200511103.

Benard, E.L., A.M. van der Sar, F. Ellett, G.J. Lieschke, H.P. Spaink, and A.H. Meijer. 2012. Infection of zebrafish embryos with intracellular bacterial pathogens. *J Vis Exp*. doi:10.3791/3781.

Berry, M.P.R., C.M. Graham, F.W. McNab, Z. Xu, S.A.A. Bloch, T. Oni, K.A. Wilkinson, R. Banchereau, J. Skinner, R.J. Wilkinson, C. Quinn, D. Blankenship, R. Dhawan, J.J. Cush, A. Mejias, O. Ramilo, O.M. Kon, V. Pascual, J. Banchereau, D. Chaussabel, and A. O'Garra. 2010. An interferon-inducible neutrophil-driven blood transcriptional signature in human tuberculosis. *Nature*. 466:973–977. doi:10.1038/nature09247.

Branzk, N., A. Lubojemska, S.E. Hardison, Q. Wang, M.G. Gutierrez, G.D. Brown, and V. Papayannopoulos. 2014. Neutrophils sense microbe size and selectively release neutrophil extracellular traps in response to large pathogens. *Nat. Immunol.* 15:1017–1025. doi:10.1038/ni.2987.

Colucci-Guyon, E., J.-Y. Tinevez, S.A. Renshaw, and P. Herbomel. 2011. Strategies of professional phagocytes in vivo: unlike macrophages, neutrophils engulf only surface-associated microbes. *Journal of Cell Science*. 124:3053–3059. doi:10.1242/jcs.082792.

Cronan, M.R., and D.M. Tobin. 2014. Fit for consumption: zebrafish as a model for tuberculosis. *Dis Model Mech*. 7:777–784. doi:10.1242/dmm.016089.

Cui, C., E.L. Benard, Z. Kanwal, O.W. Stockhammer, M. van der Vaart, A. Zakrzewska, H.P. Spaink, and A.H. Meijer. 2011. Infectious disease modeling and innate immune function in zebrafish embryos. *Methods Cell Biol.* 105:273–308. doi:10.1016/B978-0-12-381320-6.00012-6.

Davis, J.M., H. Clay, J.L. Lewis, N. Ghori, P. Herbomel, and L. Ramakrishnan. 2002. Real-time visualization of mycobacterium-macrophage interactions leading to initiation of granuloma formation in zebrafish embryos. *Immunity*. 17:693–702.

Deerinck, T.J., E.A. Bushong, A. Thor, and M.H. Ellisman. 2010. NCMIR methods for 3D EM: a new protocol for preparation of biological specimens for serial block face scanning electron microscopy. 1–3.

Denk, W., and H. Horstmann. 2004. Serial block-face scanning electron microscopy to reconstruct three-dimensional tissue nanostructure. *Plos Biol*. 2:e329. doi:10.1371/journal.pbio.0020329.

Eisenhoffer, G.T., P.D. Loftus, M. Yoshigi, H. Otsuna, C.-B. Chien, P.A. Morcos, and J. Rosenblatt. 2012. Crowding induces live cell extrusion to maintain homeostatic cell numbers in epithelia. *Nature*. 484:546–549. doi:10.1038/nature10999.

Elks, P.M., S. Brizee, M. van der Vaart, S.R. Walmsley, F.J. van Eeden, S.A. Renshaw, and A.H. Meijer. 2013. Hypoxia inducible factor signaling modulates susceptibility to mycobacterial infection via a nitric oxide dependent mechanism. *PLoS Pathog*. 9:e1003789. doi:10.1371/journal.ppat.1003789.

Ellett, F., L. Pase, J.W. Hayman, A. Andrianopoulos, and G.J. Lieschke. 2011. mpeg1 promoter transgenes direct macrophage-lineage expression in zebrafish. *Blood*. 117:e49–e56. doi:10.1182/blood-2010-10-314120.

Eum, S.-Y., J.-H. Kong, M.-S. Hong, Y.-J. Lee, J.-H. Kim, S.-H. Hwang, S.-N. Cho, L.E. Via, and C.E. Barry. 2010. Neutrophils are the predominant infected phagocytic cells in the airways of patients with active pulmonary TB. *Chest*. 137:122–128. doi:10.1378/chest.09-0903.

Fink, S.L., and B.T. Cookson. 2005. Apoptosis, Pyroptosis, and Necrosis: Mechanistic Description of Dead and Dying Eukaryotic Cells. *Infect. Immun.* 73:1907–1916. doi:10.1161/01.CIR.98.14.1422.

Francis, R.J., R.E. Butler, and G.R. Stewart. 2014. Mycobacterium tuberculosis ESAT-6 is a leukocidin causing Ca2+ influx, necrosis and neutrophil extracellular trap formation. *Cell Death Dis*. 5:e1474. doi:10.1038/cddis.2014.394.

Gu, Y., and J. Rosenblatt. 2012. New emerging roles for epithelial cell extrusion. *Current Opinion in Cell Biology*. 24:865–870. doi:10.1016/j.ceb.2012.09.003.

Hall, C., M.V. Flores, T. Storm, K. Crosier, and P. Crosier. 2007. The zebrafish lysozyme C promoter drives myeloid-specific expression in transgenic fish. *BMC Dev. Biol.* 7:42. doi:10.1186/1471-213X-7-42.

Hosseini, R., G.E. Lamers, Z. Hodzic, A.H. Meijer, M.J. Schaaf, and H.P. Spaink. 2014. Correlative light and electron microscopy imaging of autophagy in a zebrafish infection model. *autophagy*. 10:1844–1857. doi:10.4161/auto.29992.

Kimmel, C.B., W.W. Ballard, S.R. Kimmel, B. Ullmann, and T.F. Schilling. 1995. Stages of embryonic development of the zebrafish. *Dev. Dyn.* 203:253–310. doi:10.1002/aja.1002030302.

Knodler, L.A., B.A. Vallance, J. Celli, S. Winfree, B. Hansen, M. Montero, and O. Steele-Mortimer. 2010. Dissemination of invasive Salmonella via bacterial-induced extrusion of mucosal epithelia. *Proc. Natl. Acad. Sci. U.S.A.* 107:17733–17738. doi:10.1073/pnas.1006098107.

Lee, J., H.G. Remold, M.H. Ieong, and H. Kornfeld. 2006. Macrophage apoptosis in response to high intracellular burden of Mycobacterium tuberculosis is mediated by a novel caspase-independent pathway. *J Immunol*. 176:4267–4274.

Martin, C.J., K.N. Peters, and S.M. Behar. 2014. Macrophages clean up: efferocytosis and microbial control. *Curr. Opin. Microbiol.* 17:17–23. doi:10.1016/j.mib.2013.10.007.

Nouailles, G., A. Dorhoi, M. Koch, J. Zerrahn, J. Weiner, K.C. Faé, F. Arrey, S. Kuhlmann, S. Bandermann, D. Loewe, H.-J. Mollenkopf, A. Vogelzang, C. Meyer-Schwesinger, H.-W. Mittrücker, G. McEwen, and S.H.E. Kaufmann. 2014. CXCL5-secreting pulmonary epithelial cells drive destructive neutrophilic inflammation in tuberculosis. *J. Clin. Invest.* 124:1268–1282. doi:10.1172/JCI72030.

Peddie, C.J., and L.M. Collinson. 2014. Exploring the third dimension: volume electron microscopy comes of age. *Micron*. 61:9–19. doi:10.1016/j.micron.2014.01.009.

Ramakrishnan, L. 2012. Revisiting the role of the granuloma in tuberculosis. *Nat Rev Immunol*.

Ramakrishnan, L. 2013. An interview with Lalita Ramakrishnan. *Trends Pharmacol. Sci.* 34:197. doi:10.1016/j.tips.2013.02.005.

Renshaw, S.A., C.A. Loynes, D.M.I. Trushell, S. Elworthy, P.W. Ingham, and M.K.B. Whyte. 2006. A transgenic zebrafish model of neutrophilic inflammation. *Blood*. 108:3976–3978. doi:10.1182/blood-2006-05-024075.

Repasy, T., J. Lee, S. Marino, N. Martinez, D.E. Kirschner, G. Hendricks, S. Baker, A.A. Wilson, D.N. Kotton, and H. Kornfeld. 2013. Intracellular bacillary burden reflects a burst size for Mycobacterium tuberculosis in vivo. *PLoS Pathog*. 9:e1003190. doi:10.1371/journal.ppat.1003190.

Silva, M.T., M.N. Silva, and R. Appelberg. 1989. Neutrophil-macrophage cooperation in the host defence against mycobacterial infections. *Microb. Pathog.* 6:369–380.

Srivastava, S., J.D. Ernst, and L. Desvignes. 2014. Beyond macrophages: the diversity of mononuclear cells in tuberculosis. *Immunological Reviews*. 262:179–192. doi:10.1111/imr.12217.

Swaim, L.E., L.E. Connolly, H.E. Volkman, O. Humbert, D.E. Born, and L. Ramakrishnan. 2006. Mycobacterium marinum infection of adult zebrafish causes caseating granulomatous tuberculosis and is moderated by adaptive immunity. *Infect. Immun.* 74:6108–6117. doi:10.1128/IAI.00887-06.

Torraca, V., S. Masud, H.P. Spaink, and A.H. Meijer. 2014. Macrophage-pathogen interactions in infectious diseases: new therapeutic insights from the zebrafish host model. *Dis Model Mech*. 7:785–797. doi:10.1242/dmm.015594.

Volkman, H.E., H. Clay, D. Beery, J.C.W. Chang, D.R. Sherman, and L. Ramakrishnan. 2004. Tuberculous granuloma formation is enhanced by a mycobacterium virulence determinant. *Plos Biol*. 2:e367. doi:10.1371/journal.pbio.0020367.

Yang, C.-S., D.-M. Shin, H.-M. Lee, J.W. Son, S.J. Lee, S. Akira, M.-A. Gougerot-Pocidalo, J. El-Benna, H. Ichijo, and E.-K. Jo. 2008. ASK1-p38 MAPK-p47phox activation is essential for inflammatory responses during tuberculosis via TLR2-ROS signalling. *Cellular Microbiology*. 10:741–754. doi:10.1111/j.1462-5822.2007.01081.x.

Yang, C.-T., C.J. Cambier, J.M. Davis, C.J. Hall, P.S. Crosier, and L. Ramakrishnan. 2012. Neutrophils exert protection in the early tuberculous granuloma by oxidative killing of mycobacteria phagocytosed from infected macrophages. *Cell Host and Microbe*. 12:301–312. doi:10.1016/j.chom.2012.07.009.

Supplementary data

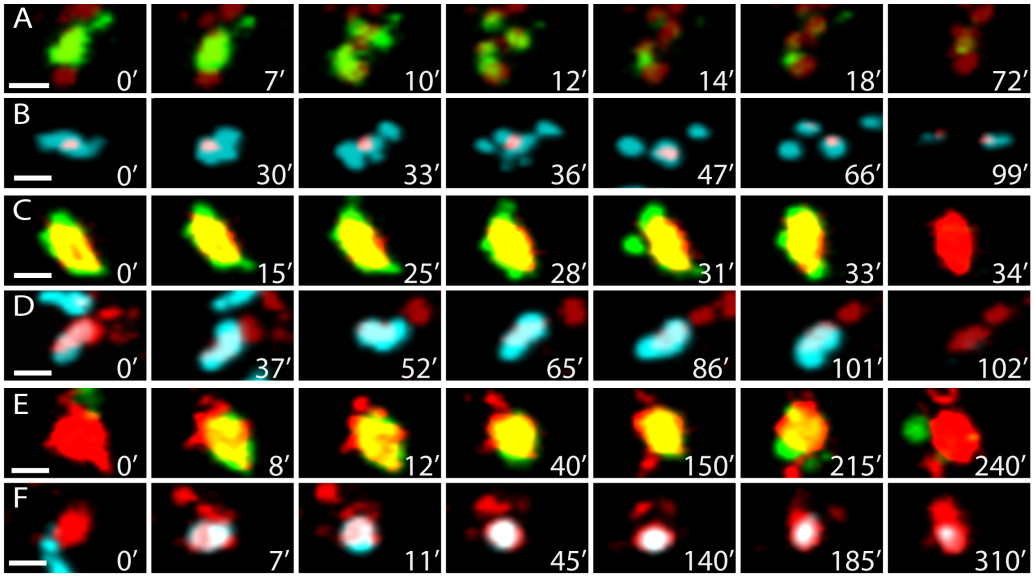

Suppl. Fig. 1. Different cell death morphologies of Mm infected macrophages and neutrophils. A and B) Selected frames taken from the image sequences of a macrophage **(A)** and a neutrophil **(B)** showing fragmentation of the cell in several compartment. **C and D)** Selected frames taken from the image sequences of a macrophage **(C)** and a neutrophil **(D)** showing rapid disappearance of the fluorescent signal. **E and F)** Selected frames taken from the image sequences of a macrophage (**E)** and a neutrophil **(F)** showing rounding up of the cell. Scale bars: 10 μm.

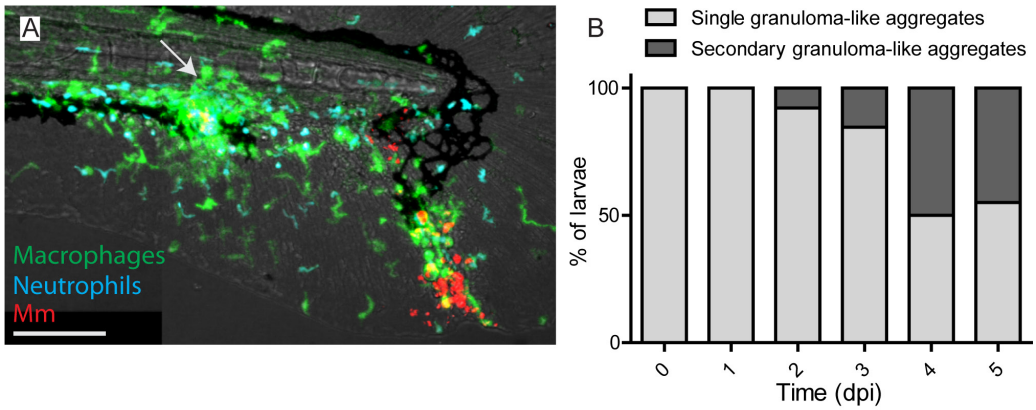

Suppl. Fig. 2. Secondary granulomas at stationary phase of infection. A) Representative image of an infected tail fin showing a secondary granuloma like aggregate (arrow) near the caudal vein. **B)** Percentage of larvae showing formation of a secondary granuloma like aggregate at different stages of infection. Scale bar: 100 μm.

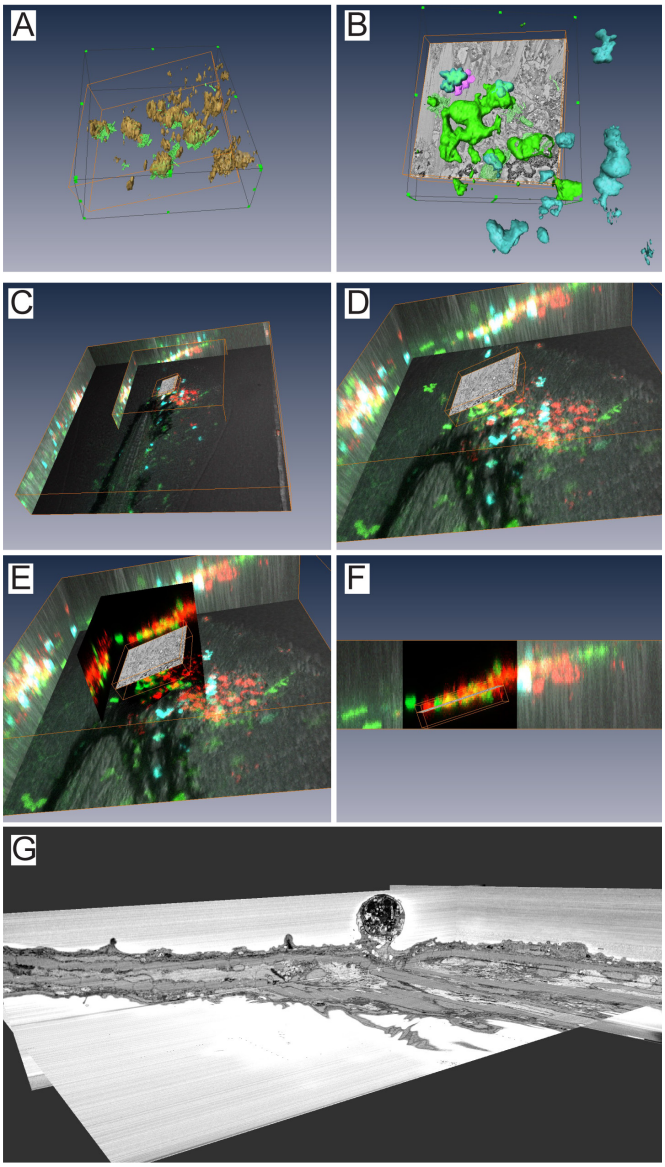

Suppl. Fig. 3. Correlation of the CLSM and 3D block-face SEM images. A) Alignment of Mm volumes imaged by CLSM and BF-SEM. The Mm in BF-SEM images were segmented and the 3D rendered surface of this segmentation is shown in green. The 3D rendered surface of the fluorescent signal obtained using CLSM is shown in yellow. B) Surface rendering of the macrophage (green) and neutrophil (blue) fluorescent signal was used after alignment to localize the macrophages and neutrophils in BF-SEM images. **C-F)** Aligned BF-SEM images projected in the 3D CLSM images shown from different angles. **G)** Orthogonal slices of BF-SEM images showing extrusion of a Mm aggregate from the outer epithelial layer.

Suppl. Fig. 1. Different cell death morphologies of *Mm* infected macrophages and neutrophils. A and B) Selected frames taken from the image sequences of a macrophage **(A)** and a neutrophil **(B)** showing fragmentation of the cell in several compartment. **C and D)** Selected frames taken from the image sequences of a macrophage **(C)** and a neutrophil **(D)** showing rapid disappearance of the fluorescent signal. **E and F)** Selected frames taken from the image sequences of a macrophage (**E)** and a neutrophil **(F)** showing rounding up of the cell. Scale bars: 10 μm.

Suppl. Fig. 2. Secondary granulomas at stationary phase of infection. A) Representative image of an infected tail fin showing a secondary granuloma like aggregate (arrow) near the caudal vein. **B)** Percentage of larvae showing formation of a secondary granuloma like aggregate at different stages of infection. Scale bar: 100 μm.

Suppl. Fig. 3. Correlation of the CLSM and 3D block-face SEM images. A) Alignment of *Mm* volumes imaged by CLSM and BF-SEM. The *Mm* in BF-SEM images were segmented and the 3D rendered surface of this segmentation is shown in green. The 3D rendered surface of the fluorescent signal obtained using CLSM is shown in yellow. B) Surface rendering of the macrophage (green) and neutrophil (blue) fluorescent signal was used after alignment to localize the macrophages and neutrophils in BF-SEM images. **C-F)** Aligned BF-SEM images projected in the 3D CLSM images shown from different angles. **G)** Orthogonal slices of BF-SEM images showing extrusion of a *Mm* aggregate from the outer epithelial layer.

Video 1. Macrophage and neutrophil behavior at the lag phase of *M. marinum* infection. Double transgenic *Tg(mpeg1:EGFP)* and *Tg(lys:DsRed)* larvae infected with *M. marinum* (red) were imaged alive every ~60 sec from 1 hpi to 12 hpi by CLSM (Nikon A1). In the top panel the dynamics of GFP-positive (green) macrophages and DsRed-positive (blue) neutrophils are shown, whereas in the bottom panels the trajectories for macrophages (left) and neutrophils (right) are indicated. The magenta and red lines represent infected macrophages and neutrophils, whereas the yellow and blue lines represent uninfected leukocytes. The infected cells remain in the tail fin, except for one of the neutrophils (red line), which undergoes reverse migration along the caudal vein. The uninfected macrophages show short trajectories in the tail fin and the neutrophils show longer tracks, of which one neutrophil (blue line) seems to be scanning a large area of the tail fin. The maximum intensity projection from 11 CLSM images (step size in z-direction, 5.56 μm) is shown at 10 frames per second. Scale bar: 100 μm.

Video 2. Macrophage burst at the exponantial phase of *M. marinum* infection. Double transgenic *Tg(mpeg1:EGFP)* and *Tg(lys:DsRed)* larvae infected with *Mm* were imaged alive every ~63 sec from 1 dpi to 2 dpi by CLSM (Nikon A1). Macrophage burst and spreading of *Mm* (red) are shown, followed by the recruitment of GFP-positive (green) macrophages and DsRed-positive (blue) neutrophils. In the left bottom the macrophages and *Mm* are visualized separately. In the right bottom only the *Mm* are visualized, and the burst event at t = 5h is indicated by arrowheads. A neutrophil phagocytized *Mm* after burst event indicated by an arrow in the upper panel at t= 8 is moving away from the infection site. The maximum intensity projection from 11 CLSM images (step size in z-direction, 5.56 μm) is shown at 10 frames per second. Scale bar: 50 μm.

Video 3. Extrusion of a *M. marinum* aggregate out of the tail fin. Double transgenic *Tg(mpeg1:EGFP)* and *Tg(lys:DsRed)* larvae infected with *M. marinum* were imaged alive every ~60 sec from 1 hpi to 17 hpi by CLSM (Nikon A1). The GFP-positive (green) macrophages containing a *M. marinum* (red) aggregate undergoes cell death showing fragmentation. The bacterial content is clearly extruded from the tail fin 3 hours after the macrophage showing fragmentation (Fig. 3D). The corresponding transmission channel is shown below, showing a protuberance on the outer epithelial layer, which is eventually shed off. The maximum intensity projection from 11 CLSM images (step size in z-direction, 5.56 μm) is shown at 10 frames per second. Scale bar: 20 μm.

Video 4. CLSM on macrophage and neutrophil behavior at the exponantial phase of *M. marinum* infection. Double transgenic *Tg(mpeg1:EGFP)* and *Tg(lys:DsRed)* larvae infected with *M. marinum* were imaged alive every ~60 sec at 3 dpi for 2.5 hours by CLSM (Nikon A1) before fixation. The two infected GFP-positive (green) macrophages and two infected DsRed-positive (blue) neutrophils that were correlated with 3D block-face SEM images are indicated by arrows. The indicated macrophages (MP1 and MP2) phagocytized *Mm* approximately 2 and 1.5 hours before fixation respectively and these cells remained GFP-positive after fixation. The neutrophil (NP1) containing *Mm* was observed 2.5 hours before fixation and undergoes cell death, observed as rapid (within ~1 min) disappearance of the fluorescent signal, ~30 min before fixation. The second neutrophil (NP2) was recruited to another infected neutrophil ~30 min before fixation. The maximum intensity projection from 11 CLSM images (step size in z-direction, 5.56 μm) is shown at 10 frames per second. Scale bar: right panel 100 μm and for the left panel 50 μm.

Video 5. Three-dimensional block-face SEM images of *Mm* infected tail fin. Double transgenic *Tg(mpeg1:EGFP)* and *Tg(lys:DsRed)* larvae infected with *M. marinum* was fixed and block face SEM imaging was performed on an 80 by 80 μm region of interest using a Quanta FEG 250 with a Gatan 3View Ultramicrotome. The video shows 154 images acquired every 150 nm step size in z-direction (103 nm pixel size) at 10 frames per second. Scale Bar: 10 μm.

Video 6. Three-dimensional block-face SEM images of necrotic neutrophil undergoing netosis. Double transgenic *Tg(mpeg1:EGFP)* and *Tg(lys:DsRed)* larva infected with *M. marinum* was fixed and block face SEM imaging was performed on an 80 by 80 μm region of interest using a Quanta FEG 250 with a Gatan 3View Ultramicrotome. The video shows 70 images in z-direction (23 nm pixel size) of the neutrophil (NF2, Fig. 4). Note the partial intact nuclear envelope (arrow) and the vesicles (arrowheads) showing the vesicles fusing with bacterial aggregate. The images were acquired with every 150 nm step size in z-direction and are in this video visualized at 10 frames per second. Scale Bar: 2 μm.

CHAPTER 4

ULTRASTRUCTURAL ANALYSIS OF THE EFFECT OF MYD88 DEFICIENCY ON GRANULOMA DEVELOPMENT DURING MYCOBACTERIUM MARINUM INFECTION

Rohola Hosseini, Gerda E. M. Lamers, Erik Bos, Abraham J. Koster, Annemarie H. Meijer, Herman P. Spaink, Marcel J. M. Schaaf

Manuscript in preparation

Summary

Myeloid differentiation factor 88 (Myd88) is the key adapter protein of Toll-like receptors (TLRs), which initiate the innate immune response upon activation. Myd88 deficiency during bacterial infection affects innate immune responses including production of cytokines and reactive oxygen species (ROS) and initiation of autophagic defence. Using a *myd88* zebrafish mutant, we investigated the morphology of granulomas during the course of *Mycobacterium marinum* (*Mm*) infection in a tail fin infection model. Light microscopy images show that *Mm* granulomas formed in the tail fin of *myd88* mutants have different morphological features compared to the infection in the wild type, including a more compact structure, a reduced recruitment of leukocytes and a reduced number of TUNEL-positive dead cells. These morphological differences were associated with an increased bacterial burden in the *myd88* mutant. Ultrastructural electron microscopy analysis showed that the majority of *Mm* in the *myd88* mutant is extracellular. The intracellular bacteria in the *myd88* mutant were mainly present in phagosomal compartments or occur as aggregates, which were not acidic. In contrast, in the granulomas of wild type larvae 46% of *Mm* are found in intracellular acidic compartments, including acidic aggregates, lysosomes and autophagic compartments. In *myd88* mutants only 13% of *Mm* is present is such acidic compartments. These observations suggest that the Myd88-dependent recruitment of leukocytes is necessary for reuptake of dead infected cells and that subsequent acidification of large bacterial aggregates taken up from dead cells restricts bacterial growth in the infected tissue.

Introduction

Pulmonary tuberculosis (TB) is a bacterial infection caused by *Mycobacterium tuberculosis* (*Mtb*), which is estimated to have infected one third of the global population. Currently, over a million people do not survive this infection each year (WHO, 2014: http://www.who.int/tb/publications/global_report/en/). Increasing occurrence of multi-drug resistant *Mtb* strains is wide spread, and in order to develop novel therapeutic strategies a better understanding of the *Mtb* pathogenesis is required (Koul et al., 2011; Goldberg et al., 2012).

During the pathogenesis of TB, *Mtb* displays a complex interaction with the immune system of the host. *Mtb* is phagocytized by macrophages, where it prevents lysosomal degradation by inhibiting phagosome-lysosome fusion (Armstron and Hart 1971; Russel, 2007). In addition, there is evidence that *Mtb* is able to escape from the phagosomes into the cytoplasm (van der Wel et al., 2007; Simeone et al., 2015). In these infected cells the *Mtb* bacteria create a niche, in which they can survive and replicate (Vergne et al., 2004; Russel et al., 2010).

Pro-inflammatory signals from infected macrophages initiate the recruitment of other innate and adaptive immune cells to the primary infection site, leading to the formation of highly organized granulomatous lesions. In these granulomas *Mtb* can persist for many years, forming a latent infection by minimizing its metabolic and replicative activity. However, *Mtb* can be reactivated resulting in an active TB infection (Gengenbacher et al., 2012).

Despite that *Mtb* exploits, macrophages to persist inside its host, macrophages are indispensable to keep *Mtb* infection under control. They recognize invading pathogens at the first stage of infection and initiate the immune response (Medzhitov and Janeway, 2000). Pathogen-associated molecular patterns (PAMPs) and endogenous danger-associated molecular patterns (DAMPs) are recognized by pattern recognition receptors (PRRs), of which the Toll-like receptors (TLR) are one of the major classes (Medzhitov and Janeway, 2000; Matzinger, 2002). Myeloid differentiation factor 88 (MYD88) is a key adaptor protein in the TLR signaling pathway since it is used by all TLRs (except for TLR3) to initiate a pro-inflammatory response (Takeda and Akira, 2004). Its C-terminal TIR domain enables interaction with TLRs or the interleukin-1 receptor (IL1R), and the N-terminal death domain enables the formation of a 'Myddosome' signaling complex, consisting of IL-1 receptor associated kinases (IRAKs). The Myddosome plays a central role in inflammation and host defense by activating the mitogen-activated protein kinase (MAPK) and the nuclear factor-κB (NF-κB) signaling pathways (Muzio et al., 1997;

Wesche et al., 1997; Lin et al., 2010; Gay et al., 2011).

Deficiency in MYD88 reduces the ability to induce an appropriate immune response and results in an increased susceptibility to pyogenic bacteria in humans (Netea et al., 2012). MyD88-deficient mice are hyporesponsive to lipopolysaccharide (LPS) and Il-1 stimulation and they are resistant to endotoxic shock (Adachi et al., 1998; Kawai et al., 1999; Akira and Takeda, 2004). In mice, it also resulted in susceptibility to various pathogens, among them *Mtb* (Ryffel et al., 2005).

The zebrafish is naturally susceptible to tuberculosis, caused by a variant of *Mycobacterium marinum* (*Mm*), which is genetically related to *Mtb*, and shows a similar pathogenesis to human disease, including the formation of granulomatous lesions (Swaim et al., 2006, Ramakrishana, 2013). The larval stage of the zebrafish enables detailed *in vivo* imaging and has been used to study host-pathogen interactions during *Mm* infection (Davis et al., 2002). The active recruitment of macrophages during *Mm* infection and the reverse migration of infected macrophages from infected sites, characterizes the dynamic nature of early granulomas (Davis and Ramakrishnan, 2009). In addition to macrophages, also neutrophils have been shown to play an important role during *Mm* infection. Neutrophils recruited to the infection site are able to actively kill the phagocytosed *Mm* by means of oxidative mechanisms (Yang et al., 2012).

In zebrafish larvae, the Myd88-signalling pathway has been shown to have a protective role during *Mm* infection (van der Vaart et al., 2013). Myd88-deficient larvae are shown to have an compromised innate immune response to bacterial infections, affecting the production of pro inflammatory cytokines (van der Vaart et al., 2013; Roca and Ramakrishnan, 2013), production of reactive nitrogen species by neutrophils (Elks et al., 2014) and the initiation of autophagic defence (van der Vaart et al., 2014), resulting in increased rates of infection. In the present study we have used this *myd88* mutant zebrafish line (*myd88*$^{-/-}$) to study the effect of Myd88 deficiency on granuloma development. To this end we used our previously reported tail fin injection model, where the formation of a single granuloma can be followed over time. Our combined results of light and electron microscopy show that *Mm* infection in *myd88* mutant larvae results in an increased bacterial burden associated with strongly reduced recruitment of leukocytes to granulomas and reduced cell death in the granuloma structures. Furthermore, we have found that in *myd88* mutants the majority of *Mm* was extracellular and that intracellular acidic compartments containing bacteria were less abundant.

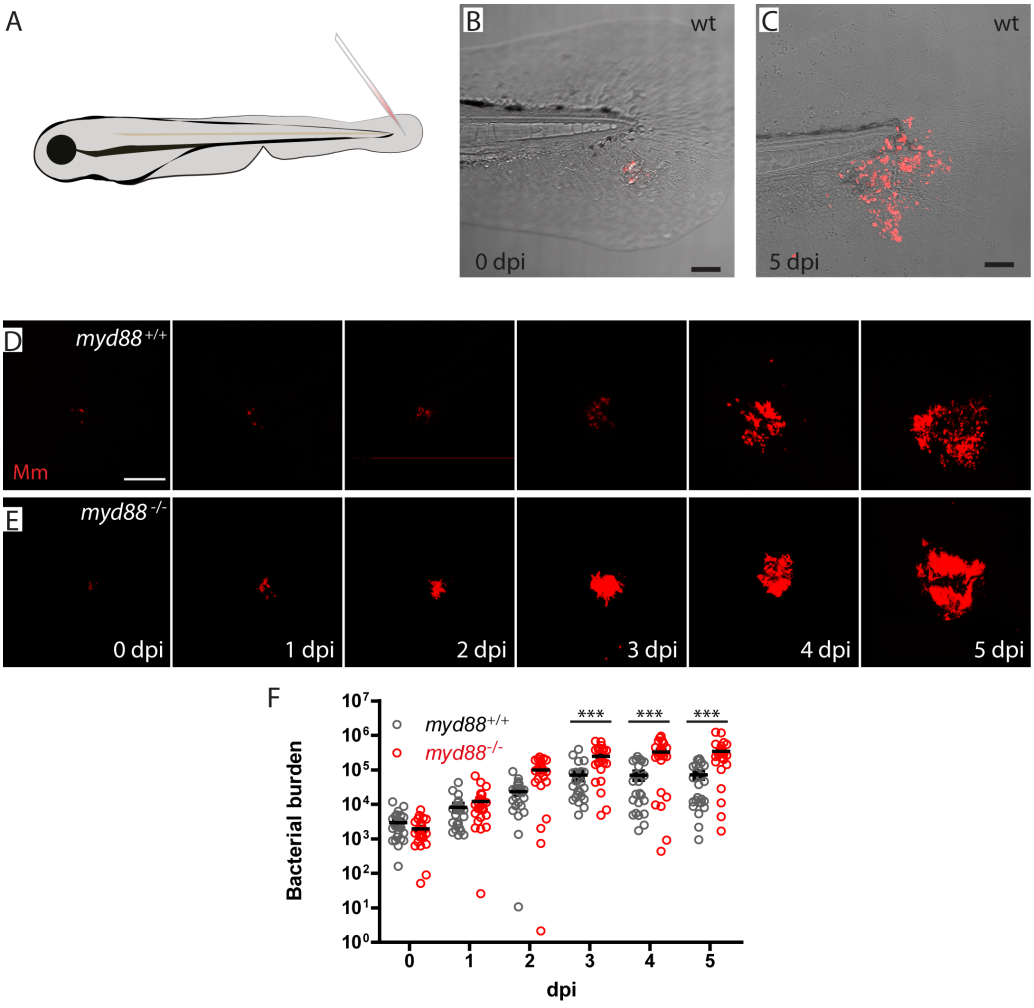

Figure 1. Granuloma development and morphology in the tail fin of zebrafish larvae. **A**) *Mm* injection in the tail fin generates single granuloma. **B and C**) Infected tail fin of the same larva with fluorescently labelled *Mm* (red) at 4 hours post infection (A) and at 4 days post infection (B) showing the localized development of the early granuloma structures. **D and E)** Representative images of larvae showing the increase of *Mm* infection (red) and development of granuloma structures in the wild type (D) and *myd88*$^{-/-}$ larvae (E). **F)** Bacterial burden in the *myd88*$^{+/+}$ (black) and *myd88*$^{-/-}$ (red) larvae. The data (mean ± SEM) were analysed using analysis of variance (ANOVA), Bonferroni's multi comparison post-test was performed on *myd88* wild type and mutant larvae at each timepoint (***, represents P<0.0001, n>20 larvae per time point). The scale bars represent 100 µm.

Results

In order to study the role of TLR/IL1R signalling during *M. marinum* (*Mm*) in zebrafish, larvae were used from a homozygous *myd88* mutant line (*myd88*$^{-/-}$) (van der Vaart et al., 2013). These larvae were infected with ~50 colony forming units (cfu) of fluorescently labelled *Mm* in the tail fin at 3 dpf. Injection of *Mm* in the tail fin induces a localized infection, which develops into a granuloma-like structure within 3 to 5 days post infection (dpi) (Figure 1A-C; Hosseini et al., 2014).

Granuloma development and bacterial burden

To provide a detailed description of the infection process and the development of the granuloma structure, confocal laser scanning microscopy (CLSM) was performed on the tail fin of infected *myd88*$^{-/-}$ and wild type (*myd88*$^{+/+}$) larvae. The bacterial burden in representative *myd88*$^{+/+}$ and *myd88*$^{-/-}$ larvae is shown in Figure 1. The infection in each of these larvae was imaged at 4 hours post infection (hpi) and at 1, 2, 3, 4 and 5 days post infection (dpi). From 2dpi onward we observed compacted bacterial aggregates in *myd88*$^{-/-}$ larvae (Figure 1E), while in the *myd88*$^{+/+}$ larvae these aggregates were much smaller and spread over the infected tissue (Figure 1D).

In a separate experiment the bacterial burden was quantified in the *myd88*$^{+/+}$ and *myd88*$^{-/-}$ larvae, based on fixed samples at 0 to 5 dpi (Figure 1F). The bacterial burden was measured as the total volume of the fluorescent signal of *Mm*. The infection size increased significantly between 0 and 3 dpi in the *myd88*$^{+/+}$ and the *myd88*$^{-/-}$ larvae. The infection size increased at a lower rate in the wild type larvae compared to the growth rate in the mutant. At 4dpi the difference in infection size between *myd88*$^{+/+}$ and *myd88*$^{-/-}$ larvae was maximal with 69 10^3 bacteria per μm^3(± 1.6 10^3) and 328 10^3 bacteria per μm^3(± 52 10^3), respectively.

Number of leukocytes at the infection site

In order to study the recruitment of leukocytes towards the infection in the tail fin in *myd88*$^{-/-}$ zebrafish, we performed Lcp1/L-plastin immunostaining at 4 dpi for visualization of all leukocytes (Figure 2). The larvae were imaged using CLSM and representative images are shown for *myd88*$^{+/+}$ and *myd88*$^{-/-}$ larvae (Figure 2A and 2B respectively). At 4 dpi the infection in the tail fin has resulted in formation of an initial stage granuloma, which in *myd88*$^{+/+}$ larvae was observed as a large local accumulation of L-plastin positive cells (35.4 ± 4.2) at the site of the infection in the tail fin (Figure 2A and 2C). In the *myd88*$^{-/-}$ larvae the number of L-plastin-positive

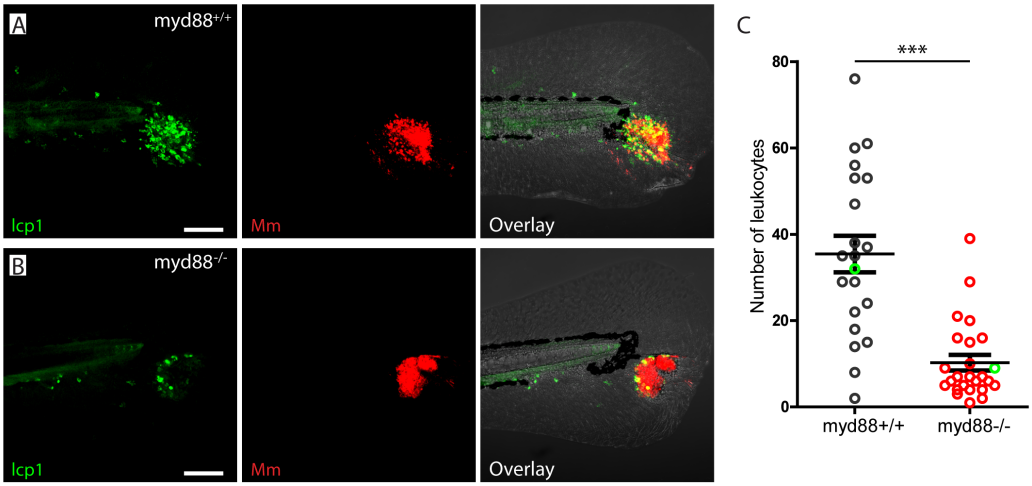

Figure 2. Number of leukocytes at the site of infection in *myd88*$^{+/+}$ and *myd88*$^{-/-}$ larvae. **A and B)** Representative images of a larva showing lcp1-positive cells (green) and *Mm* (red) in *myd88*$^{+/+}$ (A) and *myd88*$^{-/-}$ (B) larvae at 4 dpi. **C)** Quantification of lcp1-positive cell shows less leukocytes to be present at the site of infection in *myd88*$^{-/-}$ larvae. The data (mean ± SEM) were analyzed using a two-tailed student t test (*** indicates $P<0.001$, n>20 larvae per condition). Scale bar represents 100 µm.

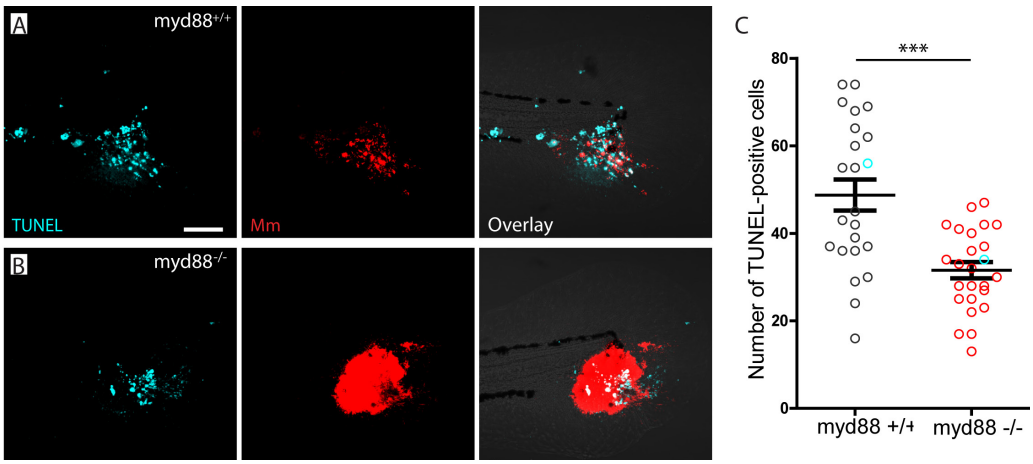

Figure 3. TUNEL-positive cells at the site of infection in *myd88*$^{+/+}$ and *myd88*$^{-/-}$ larvae. **A and B)** Representative images of a larva showing TUNEL-positive cells (green) and *Mm* (red) in *myd88*$^{+/+}$ (A) and *myd88*$^{-/-}$ (B) larvae at 4 dpi. **C)** Quantification of TUNEL-positive cell shows less dead cells to be present at the site of infection in *myd88*$^{-/-}$ larvae. The data (mean ± SEM) were analyzed using a two-tailed student t test (*** indicates $P<0.001$, n>20 larvae per condition). Scale bar represents 100 µm.

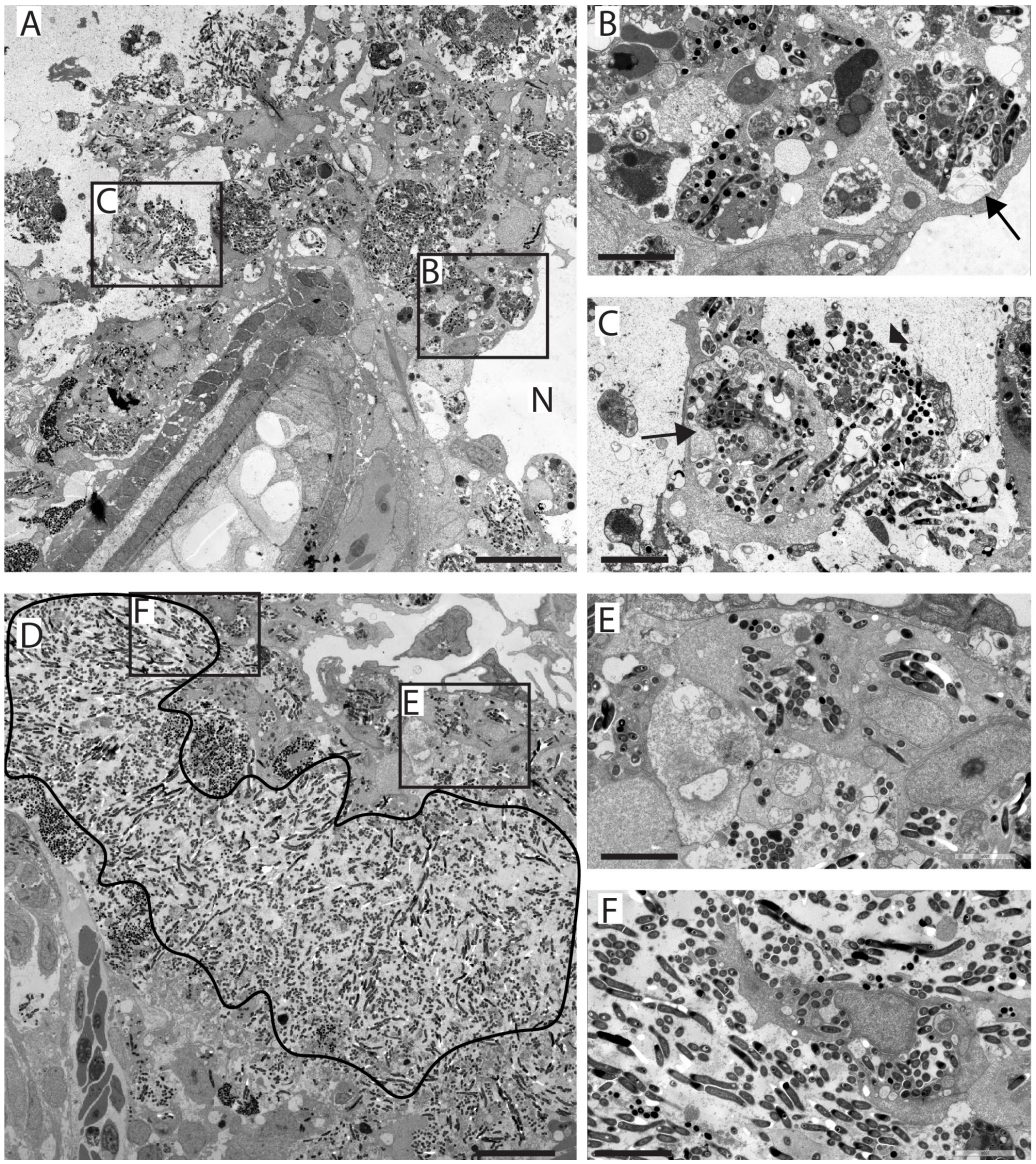

Figure 4. Granuloma structures in *myd88*$^{-/-}$ consist mainly of extracellular *Mm*. **A)** TEM image of a granuloma in representative *myd88*$^{+/+}$ larvae, showing the necrotic centre (N) and aggregates of *Mm* in the immune cells. **B and C)** Higher magnification of regions indicated in **A**, showing infected cells (arrowheads) and extracellular *Mm* (arrows). **D)** TEM image of a granuloma in representative *myd88*$^{-/-}$ larvae showing the area with extracellular *Mm* (black line). **E and F)** Higher magnification of region indicated in **D**, showing extracellular bacteria and infected cells (arrowheads). n=3 per group, the scale bars in A-D; 20 μm and in B-C and E-F; 10 μm.

cells at the site of infection was significantly lower (10.2 ± 1.8). The leukocytes in the *myd88*$^{-/-}$ larvae were mainly observed surrounding the site of infection, while in the wild type larvae the leukocytes were observed within the infected area (Figure 2A and 2B).

Number of dead cells at the infection site

The lower number of leukocytes observed at the site of infection in *myd88*$^{-/-}$ larvae could either be due to a lower number of leukocytes recruited to the infected area or to a higher rate of cell death of these cells. To address this issue we performed a fluorescent Terminal deoxynucleotidyl transferase dUTP nick end labelling (TUNEL) assay on *myd88*$^{+/+}$ and *myd88*$^{-/-}$ larvae at 4 dpi, which visualizes double stranded DNA breaks, thereby labelling apoptotic as well as necrotic cells (Figure 3). The *myd88*$^{+/+}$ larvae show a high number of TUNEL positive cells (48.7 ± 3.6) throughout the site of infection (Figure 3A). The *myd88*$^{-/-}$ larvae show a lower number of TUNEL positive cells (31.6 ± 1.8; Figure 3B and 3C), which were mainly located at the centre of the infected area. Therefore, it can be concluded that the lower number of leukocytes at infection sites in *myd88*$^{-/-}$ is a consequence of reduced recruitment rather than increased cell death.

Transmission electron microscopy of *Mm* infection in *myd88*$^{-/-}$ larvae

Transmission electron microscopy (TEM) was performed on the tail fin granulomas of *Mm* infected *myd88*$^{+/+}$ larvae and *myd88*$^{-/-}$ larvae, in order to analyze the ultrastructural effects of Myd88 deficiency (Figure 4). At 5dpi, the *myd88*$^{+/+}$ larvae show a necrotic center in the infected area, visible as a hole in the tail fin, which is surrounded by a large number of cells containing bacteria (Figure 4A and 4B). In the *myd88*$^{-/-}$ larvae the majority of bacteria were found to be extracellular (Figure 4C and 4D), and the large area containing these extracellular bacteria was surrounded by infected cells (Figure 4D).

To determine the nature and frequency of different cell-bacterium interactions in *myd88*$^{+/+}$ and *myd88*$^{-/-}$ larvae, we quantified the occurrence of intracellular *Mm* in the cytoplasm without any membrane structures surrounding it, or in different types of intracellular compartments. The analysis of this quantification and representative images of each type of interaction are shown in Figure 5. The majority of intracellular bacteria was found in aggregates (5> bacteria per compartment), ~64% in *myd88*$^{+/+}$ compared to ~50% in *myd88*$^{-/-}$ larvae (Fig. 5 A and B). However, acidic aggregates, characterized by a lysosomal morphology with uniform electron dense content in the compartment, were less abundant in mutant larvae (~8%) compared to wild type (~ 39%, Figure 5 B). Individual bacteria were present in phagosomes, characterized by a single membrane with

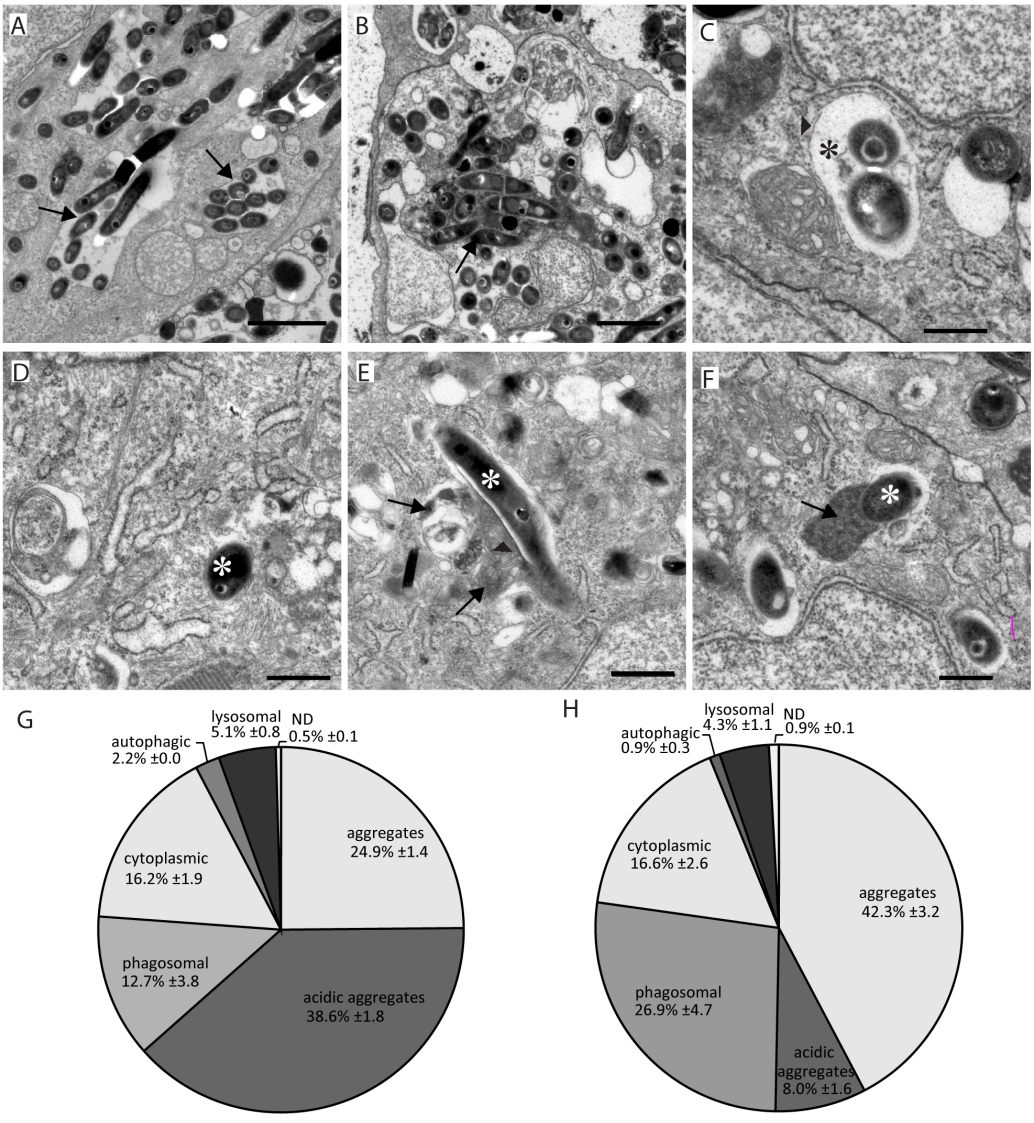

Figure 5. Quantification of intracellular *Mm* shows altered distribution of bacteria in different compartments in Myd88$^{-/-}$. **A to F)** Representative TEM images of *Mm* in different compartments. **A)** Aggregates were observed as a compact cluster of bacteria (<5) without any electron dense areas (arrows). **B)** Acidic aggregates were observed as a compact number of bacteria in a compartment having a uniform electron density between the bacteria (arrowhead) and/or electron dense regions (arrow). **C)** Phagosomal compartment containing bacteria surrounded by a single membrane (arrowhead) with an electron-transparent zone (asterisk), without any cytoplasmic material in the compartment. **D)** Cytoplasmic bacteria are shown not enclosed by any membrane, indicated by a white asterisk. **E)** Autophagic vacuoles containing bacteria (asterisk), with partially degraded content (arrowhead) and other fused vacuoles (arrows). **F)** Lysosomal compartment containing bacteria (asterisk) with

uniform electron dense content (arrow). **G and H)** The fractions (± SEM) of intracellular *Mm* found in different compartments or free in the cytoplasm are presented in a pie chart for *myd88*$^{+/+}$ (G) and *myd88*$^{-/-}$ (H). n=3 per group, the scale bars in A-B; 2 μm and in C-F; 500 nm.

an electron-transparent zone or tightly surrounding the bacteria without any cytoplasmic material (Figure 5C). In mutant larvae ~27% of bacteria were found in those phagosomal compartments compared to ~13% in the wild types. A similar number of bacteria was found in the cytoplasm, not enclosed by any membrane, in the wild type and mutant larvae (respectively, ~16% and ~17%, Figure 5D). In addition, bacteria were found in autophagic compartments, in the *myd88*$^{+/+}$ (~2%) and *myd88*$^{-/-}$ (~1%) larvae. These compartments are characterized by partially degraded cytoplasmic content and organelles as a result of engulfment by or fusion with autophagosomes (Figure 5E, Hosseini et al., 2014). Finally, some bacteria were located inside lysosomal compartments (<5 bacteria per compartment) with regular electron dense content in the wild type and *myd88*$^{-/-}$ larvae, at a frequency of respectively ~5% and ~4% (Figure 5F). In conclusion, the reduced presence of acidic aggregates is the most notable difference between *myd88*$^{-/-}$ and wild type larvae.

Discussion

In this paper we provide new insight in the early stages of granuloma development and structure during *Mm* infection by both light and electron microscopy using the tail fin infection model in zebrafish larvae. We show that localized infection develops in the tail fin of both *myd88*$^{+/+}$ and *myd88*$^{-/-}$ larvae. In the *myd88*$^{-/-}$ larvae the infection developed much faster and showed an increased infection size at 4 dpi. This is consistent with the data shown in a blood island infection model, showing an increased infection size and susceptibility to mycobacterium infection in *myd88*$^{-/-}$ larvae (van der Vaart et al., 2013). In addition, using the tail fin infection model we observed a clear different phenotype of infection in the mutant compared to the wild type larvae (Figure 1D and 1E). The mutant shows more compacted *Mm* in a large aggregated growth spot at the site of infection and electron microscopy showed that the majority of bacteria in this location were extracellular.

The number of leukocytes at the site of infection was significantly lower in the mutant at 4dpi (Figure 2C). This lower number of leukocytes was not due to higher cell death rate of these cells in the mutant larvae, since significantly less TUNEL-positive cells were observed at the site of infection (Figure 3C). This indicated that the low presence of leukocytes is due to reduced recruitment towards the pathogen

in *myd88*$^{-/-}$ larvae. However, the recruitment of leukocytes towards *Mm* infection is not dependent on *myd88* mediated signalling at initial stages of infection (Cambier et al., 2014), as shown in hindbrain infection upon morpholino knock down of *myd88*. Apparently, there is a difference in Myd88 dependency between initial and long-term leukocyte response to *Mm* infection. The long term recruitment is likely to be dependent on the induction of genes for pro-inflammatory mediators including cytokines and leukotrienes and genes encoding tissue remodelling factors like matrix metalloproteinases. These genes are strongly induced along with the expansion of granulomas in zebrafish larvae and the induction of these genes is dependent on *myd88* (van der Vaart et al., 2013). The increased extracellular growth of *Mm* in *myd88*$^{-/-}$ larvae is consisted with results in other systems in which the immune system is compromised, for example knock down of the TNF receptor, (Roach et al., 2002, Tobin et al., 2012). Additionally, we studied the intracellular bacteria that resided in the immune cells of the mutant and the wild type. We already showed that the largest fraction of *Mm* in the wild type larvae were observed in acidic aggregates (Hosseini et al., 2014). Interestingly, a distinct difference was observed in the nature of compartments in which intracellular *Mm* was present. In mutant larvae a much smaller fraction was found in these acidic aggregates and a larger fraction in non-acidic aggregates and phagosomal compartments. It seems that acidification of these larger aggregates is highly Myd88 dependent and helps to restrict bacterial growth, since *myd88* mutants developed severely increased bacterial burden. Alternatively, the differences could be explained by presence of *Mm* in different cell types than leukocytes in the mutant. However, we favour the interpretation that the large acidic bacterial aggregates in the granulomas of wild type larvae result from the efferocytosis of dead infected cells by leukocytes that are recruited to the infection site in a Myd88-dependent manner.

In summary, we have identified a low level of recruitment of leukocytes towards infection at the later stage of *Mm* infection in *myd88* mutants. This is probably due to the decrease in inflammatory responses induced by the *myd88*-NFκB pathway, which results in an increased infection due to uncontrolled mycobacterial growth in non-acidifying compartments of infected cells as well as extracellular growth of bacteria.

Materials and Methods

Zebrafish strains and maintenance

Zebrafish were handled in compliance with the local animal welfare regulations and maintained according to standard protocols (www.zfin.org). The *myd88*$^{+/+}$ and

the *myd88*$^{-/-}$ zebrafish strains were used for this study. All fish were raised and grown at 28.5 °C on a 14 h light : 10 h dark cycle. Embryos were obtained from natural spawning at the beginning of the light period and kept in egg water (60 µg/ml Instant Ocean sea salts).

Zebrafish tail fin infection

The *M. marinum* M strain fluorescently labelled with E2-crimson was used and prepared at ~500 colony-forming units per 1 nl as previously described (Benard et al., 2013). Borosilicate glass microcapillaries (Harvard Apparatus, 300038) were used with a micropipette puller device (Sutter Instruments Inc.) for preparing microinjection needles. Zebrafish larvae were injected in the tail fin at 3 dpf using the Eppendorf microinjection system with a fine (~5 to 10 micron) needle tip broken off with tweezers and mounted at a 30-degree angle. Larvae were anesthetized in egg water with 200 µg/mL 3-aminobenzoic acid (Tricaine; Sigma-Aldrich, E10521) and injected between the 2 epidermal layers at the ventral part of the tail fin (Fig. 1), as previously described (Hosseini et al., 2014). Larvae were fixed at desired time points after infection with 4% paraformaldehyde in PBS-T (phosphate-buffered saline; NaCl 150 mM, K_2HPO_4 15 mM, KH_2PO_4 5 mM) with 0.05% Tween 20 (Merck Millipore, 8221840500) with gentle agitation for 18 h at 4 °C. The larvae were washed the next day with PBS-T and stored at 4 °C for further staining or until imaging.

TUNEL assay

The TUNEL experiments were performed using Millipore ApopTag Peroxidase In Situ Apoptosis detection kit and Roche Anti-Digoxigenin-POD Fab fragments using a protocol adapted for use in Zebrafish embryos (Ref). For fluorescent detection Perkin Elmer TSA Fluorescence kits Cy5 and Fluorescein were used.

Confocal laser scanning microscopy

Fixed larvae were mounted in 1% low melting agarose (Sigma-Aldrich, A9414) and imaged with a Leica TCS SPE (Wetzlar, Germany) confocal laser scanning microscope using the 488 and the 633 laser lines with 20X (NA 0.7) and 63X (NA 1.2) objectives. Images were analysed using Fiji software.

Transmission electron microscopy

Before being used for electron microscopy the zebrafish larvae were anesthetized with 200 µg/ml tricaine and afterwards immediately fixated in 2% glutaraldehyde and 2% paraformaldehyde in sodium cacodylate buffer (pH 7.2) for 3 h at room temperature followed by fixation for 16 h at 4 °C. Postfixation was performed in

1% osmium tetroxide in sodium cacodylate buffer for 1 h at room temperature. After dehydration through a graded series of ethanol all specimens were kept in epoxy resin (Agar Scientific, AGR1043) for 16 h before embedding. Ultrathin sections were collected on Formvar coated 200 mesh or one hole copper grids (Agar Scientific, AGS162) stained with 2% uranyl acetate in 50% ethanol and lead citrate for 10 min each. Electron microscopy images were obtained with a JEOL JEM-1010 transmission electron microscope (Tokyo, Japan) equipped with an Olympus Megaview camera (Tokyo, Japan).

Statistical analysis

All data (mean ± SEM) were analyzed (Prism version 5.0, GraphPad Software) using one-way analysis of variance (ANOVA) with Bonferroni's multi comparison post-test for multiple groups. Two-tailed student t tests was used for comparing 2 conditions.

References

Adachi, O., T. Kawai, K. Takeda, M. Matsumoto, H. Tsutsui, M. Sakagami, K. Nakanishi, and S. Akira. 1998. Targeted disruption of the MyD88 gene results in loss of IL-1- and IL-18-mediated function. *Immunity*. 9:143–150.

Akira, S., and K. Takeda. 2004. Toll-like receptor signalling. *Nat Rev Immunol*. 4:499–511. doi:10.1038/nri1391.

Alonso, S., K. Pethe, D.G. Russell, and G.E. Purdy. 2007. Lysosomal killing of Mycobacterium mediated by ubiquitin-derived peptides is enhanced by autophagy. *Proc. Natl. Acad. Sci. U.S.A.* 104:6031–6036. doi:10.1073/pnas.0700036104.

Armstrong, J.A., and P.D. Hart. 1971. Response of cultured macrophages to Mycobacterium tuberculosis, with observations on fusion of lysosomes with phagosomes. *J. Exp. Med.* 134:713–740. doi:10.1084/jem.134.3.713.

Benard, E.L., A.M. van der Sar, F. Ellett, G.J. Lieschke, H.P. Spaink, and A.H. Meijer. 2012. Infection of zebrafish embryos with intracellular bacterial pathogens. *J Vis Exp*. doi:10.3791/3781.

Bortoluci, K.R., and R. Medzhitov. 2010. Control of infection by pyroptosis and autophagy: role of TLR and NLR. *Cell. Mol. Life Sci.* 67:1643–1651. doi:10.1007/s00018-010-0335-5.

Cambier, C.J., K.K. Takaki, R.P. Larson, R.E. Hernandez, D.M. Tobin, K.B. Urdahl, C.L. Cosma, and L. Ramakrishnan. 2014. Mycobacteria manipulate macrophage recruitment through coordinated use of membrane lipids. *Nature*. 505:218–222. doi:10.1038/nature12799.

Davis, J.M., and L. Ramakrishnan. 2009. The role of the granuloma in expansion and dissemination of early tuberculous infection. *Cell*. 136:37–49. doi:10.1016/j.cell.2008.11.014.

Davis, J.M., H. Clay, J.L. Lewis, N. Ghori, P. Herbomel, and L. Ramakrishnan. 2002. Real-time visualization of mycobacterium-macrophage interactions leading to initiation of granuloma formation in zebrafish embryos. *Immunity*. 17:693–702.

Deng, Q., E.A. Harvie, and A. Huttenlocher. 2012. Distinct signalling mechanisms mediate neutrophil attraction to bacterial infection and tissue injury. *Cellular Microbiology*. 14:517–528. doi:10.1111/j.1462-5822.2011.01738.x.

Elks, P.M., M. van der Vaart, V. van Hensbergen, E. Schutz, M.J. Redd, E. Murayama, H.P. Spaink, and A.H. Meijer. 2014. Mycobacteria counteract a TLR-mediated nitrosative defense mechanism in a zebrafish infection model. *PLoS ONE*. 9:e100928. doi:10.1371/journal.pone.0100928.

Gay, N.J., M. Gangloff, and L.A.J. O'Neill. 2011. What the Myddosome structure tells us about the initiation of innate immunity. *Trends in Immunology*. 32:104–109. doi:10.1016/j.it.2010.12.005.

Gengenbacher, M., and S.H.E. Kaufmann. 2012. Mycobacterium tuberculosis: success through dormancy. *FEMS Microbiology Reviews*. 36:514–532. doi:10.1111/j.1574-6976.2012.00331.x.

Goldberg, D.E., R.F. Siliciano, and W.R. Jacobs. 2012. Outwitting evolution: fighting drug-resistant TB, malaria, and HIV. *Cell*. 148:1271–1283. doi:10.1016/j.cell.2012.02.021.

Hosseini, R., G.E. Lamers, Z. Hodzic, A.H. Meijer, M.J. Schaaf, and H.P. Spaink. 2014. Correlative light and electron microscopy imaging of autophagy in a zebrafish infection model. *autophagy*. 10:1844–1857. doi:10.4161/auto.29992.

Kawai, T., O. Adachi, T. Ogawa, K. Takeda, and S. Akira. 1999. Unresponsiveness of MyD88-deficient mice to endotoxin. *Immunity*. 11:115–122.

Koul, A., E. Arnoult, N. Lounis, J. Guillemont, and K. Andries. 2011. The challenge of new drug discovery for tuberculosis. *Nature*. 469:483–490. doi:10.1038/nature09657.

Lin, P.L., C.B. Ford, M.T. Coleman, A.J. Myers, R. Gawande, T. Ioerger, J. Sacchettini, S.M. Fortune, and J.L. Flynn. 2014. Sterilization of granulomas is common in active and latent tuberculosis despite within-host variability in bacterial killing. *Nat. Med.* 20:75–79. doi:10.1038/nm.3412.

Lin, S.-C., Y.-C. Lo, and H. Wu. 2010. Helical assembly in the MyD88-IRAK4-IRAK2 complex in TLR/IL-1R signalling. *Nature*. 465:885–890. doi:10.1038/nature09121.

Matzinger, P. 2002. The danger model: a renewed sense of self. *Science*. 296:301–305. doi:10.1126/science.1071059.

Medzhitov, R., and C. Janeway. 2000. The Toll receptor family and microbial recognition. *Trends Microbiol.* 8:452–456.

Muzio, M., J. Ni, P. Feng, and V.M. Dixit. 1997. IRAK (Pelle) family member IRAK-2 and MyD88 as proximal mediators of IL-1 signaling. *Science*. 278:1612–1615.

Netea, M.G., C. Wijmenga, and L.A.J. O'Neill. 2012. Genetic variation in Toll-like receptors and disease susceptibility. *Nat. Immunol.* 13:535–542. doi:10.1038/ni.2284.

Ramakrishnan, L. 2013. Looking within the zebrafish to understand the tuberculous granuloma. *Adv. Exp. Med. Biol.* 783:251–266. doi:10.1007/978-1-4614-6111-1_13.

Roach, S.K., and J.S. Schorey. 2002. Differential regulation of the mitogen-activated protein kinases by pathogenic and nonpathogenic mycobacteria. *Infect. Immun.* 70:3040–3052.

Roach, S.K., S.-B. Lee, and J.S. Schorey. 2005. Differential activation of the transcription factor cyclic AMP response element binding protein (CREB) in macrophages following infection with pathogenic and nonpathogenic mycobacteria and role for CREB in tumor necrosis factor alpha production. *Infect. Immun.* 73:514–522. doi:10.1128/IAI.73.1.514-522.2005.

Roca, F.J., and L. Ramakrishnan. 2013. TNF dually mediates resistance and susceptibility to mycobacteria via mitochondrial reactive oxygen species. *Cell*. 153:521–534. doi:10.1016/j.cell.2013.03.022.

Russell, D.G. 2007. Who puts the tubercle in tuberculosis? *Nat. Rev. Microbiol.* 5:39–47. doi:10.1038/nrmicro1538.

Russell, D.G., C.E. Barry, and J.L. Flynn. 2010. Tuberculosis: what we don't know can, and does, hurt us. *Science*. 328:852–856. doi:10.1126/science.1184784.

Ryffel, B., C. Fremond, M. Jacobs, S. Parida, T. Botha, B. Schnyder, and V. Quesniaux. 2005. Innate immunity to mycobacterial infection in mice: critical role for toll-like receptors. *Tuberculosis*. 85:395–405. doi:10.1016/j.tube.2005.08.021.

Sasindran, S.J., and J.B. Torrelles. 2011. Mycobacterium Tuberculosis Infection and Inflammation: what is Beneficial for the Host and for the Bacterium? *Front. Microbio.* 2:2. doi:10.3389/fmicb.2011.00002.

Simeone, R., F. Sayes, O. Song, M.I. Gröschel, P. Brodin, R. Brosch, and L. Majlessi. 2015. Cytosolic access of Mycobacterium tuberculosis: critical impact of phagosomal acidification control and demonstration of occurrence in vivo. *PLoS Pathog*. 11:e1004650. doi:10.1371/journal.ppat.1004650.

Swaim, L.E., L.E. Connolly, H.E. Volkman, O. Humbert, D.E. Born, and L. Ramakrishnan. 2006. Mycobacterium marinum infection of adult zebrafish causes caseating granulomatous tuberculosis and is moderated by adaptive immunity. *Infect. Immun.* 74:6108–6117. doi:10.1128/IAI.00887-06.

Takeda, K., and S. Akira. 2004. Microbial recognition by Toll-like receptors. *J. Dermatol. Sci.* 34:73–82. doi:10.1016/j.jdermsci.2003.10.002.

Tobin, D.M., F.J. Roca, S.F. Oh, R. McFarland, T.W. Vickery, J.P. Ray, D.C. Ko, Y. Zou, N.D. Bang, T.T.H. Chau, J.C. Vary, T.R. Hawn, S.J. Dunstan, J.J. Farrar, G.E. Thwaites, M.-C. King, C.N. Serhan, and L. Ramakrishnan. 2012. Host genotype-specific therapies can optimize the inflammatory response to mycobacterial infections. *Cell*. 148:434–446. doi:10.1016/j.cell.2011.12.023.

van der Vaart, M., C.J. Korbee, G.E.M. Lamers, A.C. Tengeler, R. Hosseini, M.C. Haks, T.H.M. Ottenhoff, H.P. Spaink, and A.H. Meijer. 2014. The DNA damage-regulated autophagy modulator DRAM1 links mycobacterial recognition via TLP-MYD88 to authophagic defense. *Cell Host and Microbe*. 15:753–767. doi:10.1016/j.chom.2014.05.005.

van der Vaart, M., J.J. van Soest, H.P. Spaink, and A.H. Meijer. 2013. Functional analysis of a zebrafish myd88 mutant identifies key transcriptional components of the innate immune system. *Dis Model Mech*. 6:841–854. doi:10.1242/dmm.010843.

van der Wel, N., D. Hava, D. Houben, D. Fluitsma, M. van Zon, J. Pierson, M. Brenner, and P.J. Peters. 2007. M. tuberculosis and M. leprae Translocate from the Phagolysosome to the Cytosol in Myeloid Cells. *Cell*. 129:1287–1298. doi:10.1016/j.cell.2007.05.059.

Vergne, I., R.A. Fratti, P.J. Hill, J. Chua, J. Belisle, and V. Deretic. 2004. Mycobacterium tuberculosis phagosome maturation arrest: mycobacterial phosphatidylinositol analog phosphatidylinositol mannoside stimulates early endosomal fusion. *Molecular Biology of the Cell*. 15:751–760. doi:10.1091/mbc.E03-05-0307.

Wesche, H., C. Korherr, M. Kracht, W. Falk, K. Resch, and M.U. Martin. 1997. The interleukin-1 receptor accessory protein (IL-1RAcP) is essential for IL-1-induced activation of interleukin-1 receptor-associated kinase (IRAK) and stress-activated protein kinases (SAP kinases). *J. Biol. Chem.* 272:7727–7731.

Yang, C.-T., C.J. Cambier, J.M. Davis, C.J. Hall, P.S. Crosier, and L. Ramakrishnan. 2012. Neutrophils exert protection in the early tuberculous granuloma by oxidative killing of mycobacteria phagocytosed from infected macrophages. *Cell Host and Microbe*. 12:301–312. doi:10.1016/j.chom.2012.07.009.

Zhang, J., S. Liu, K.V. Rajendran, L. Sun, Y. Zhang, F. Sun, H. Kucuktas, H. Liu, and Z. Liu. 2013. Pathogen recognition receptors in channel catfish: III phylogeny and expression analysis of Toll-like receptors. *Developmental & Comparative Immunology*. 40:185–194. doi:10.1016/j.dci.2013.01.009.

CHAPTER 5

SUMMARY AND DISCUSSION

The immune response towards (myco)bacterial infection consists of complex intracellular signaling for the activation of effector molecules to eliminate the pathogen, and intercellular signaling that alerts other immune cells to the presence of infectious agents (Philips and Ernst, 2012; Berg and Ramakrishnan, 2012; Repasy et al., 2013). This work aimed to study both of these responses simultaneously using the zebrafish model. In this chapter the major findings of this study are summarized and discussed and perspectives for future studies are described.

The tail fin infection model

In this thesis the development of a novel infection method using the zebrafish as an animal model is described that enables *in vivo* visualization of intracellular structures by both light and electron microscopy. This tail fin infection model is introduced in **Chapter 2**. In this model, pathogens are injected directly in the tail fin of zebrafish larvae, resulting in a local infection in the tail fin in the case of a *M. marinum* (*Mm*) infection, which leads to the formation of single early granuloma structure. The tail fin is very suitable for high-resolution light microscopy imaging, because the tissue consists of only a few cell layers (Kimmel et al., 1995), and the infected cells are therefore located at a relatively short distance from the objective of the microscope. The relatively low amount of out of focus light enhances the contrast and the resolution of images of this tissue. For transmission electron microscopy this localized infection model has the major advantage that only a small tissue volume needs to be investigated in order to find and image the site of infection. When the larvae are imaged using light microscopy before fixation and TEM imaging, the images obtained by these two different techniques can be correlated. In our experiments, this correlation was performed based on the localization of the bacteria, which were fluorescently labelled and their morphology could easily be recognized in TEM images.

In future studies, the tail fin of zebrafish larvae may be suitable for super-resolution light microscopy techniques, because of the low level of out-of-focus light and the relatively small tissue volume that needs to be investigated. Advances in electron microscopy have been made, which enable studying cellular structures in their native state (i.e. cryo-genic conditions) using cryo-electron microscopy (Studer et al., 2008; Koning et al., 2014). Since zebrafish larvae are too large for cryo-fixation (high-pressure freezing), limited cryo-EM studies have been performed on zebrafish samples. However, high pressure freezing of just the tail fin would be a very interesting approach in future experiments.

The tail fin infection model offers new opportunities for studying host-pathogen interactions in zebrafish larvae. The interaction between the pathogen and the host immune system in vivo is complex as the host cell initially induces an intracellular response towards the pathogen, and subsequently cells migrate and signal to other immune cells, and eventually a collective immune response from different cell types takes place. Thus far multiple infection models were required to study these different aspects of infection. In this thesis, the tail fin infection model is presented, which provides opportunities for future studies on the role of host-pathogen interactions to be performed within the same infection model. This model can for example be valuable for screening of different knock-out zebrafish lines. The introduction of the CRISPR/Cas9 technology for generating knock-out lines is expected to revolutionize the field of zebrafish research, and the tail fin infection model may be instrumental in providing a valuable assay to study the phenotype of these lines.

Autophagy as an intracellular immune response against *Mm*

The autophagic response against *Mm* was investigated in transgenic zebrafish larvae expressing a GFP-Lc3 fusion protein, using LM and TEM in **Chapter 2**. Lc3 is a ubiquitin-like protein involved in the biogenesis of autophagosomal structures, and often used as a marker for autophagic compartments (Kabeya et al., 2000; Klionsky et al., 2012). Two types of GFP-Lc3-positive structures appeared upon infection of *Mm* in the tail fin. First, numerous relatively small vesicles (~1 µm) were observed that did not contain bacteria. These small vesicles are highly dynamic and can fuse with other compartments containing bacteria. Correlation of light and electron microscopy images showed that these small GFP-Lc3-positive vesicles in the vicinity of bacteria indeed had the appearance of an initial autophagic vacuole (Eskelinen, 2008). Second, larger GFP-Lc3 structures (~3 µm) were present that often contained phagocytized bacteria. The GFP-Lc3 signal of these larger structures could either originate from an autophagosome, which had taken up cytosolic bacteria, or from an autophagosome/autolysosome after fusion with a phagosomal compartment containing bacteria (as has been shown in cell culture studies). The autophagosomal nature of these vesicles was supported by correlative light and electron microscopy data showing that the larger GFP-Lc3 vesicle containing bacteria had the morphology of a degradative autophagic vacuole. The advantage of studying the infection process in a whole animal model was demonstrated by showing different autophagic responses in the immune cells compared to the other cell types. The larger bacteria-containing GFP-Lc3 vesicles were observed more often in leukocytes than in other cell types (mainly epithelial cells in the tail fin).

The tail fin infection model could be used to visualize different autophagic adaptor proteins to understand the basic mechanisms underlying autophagic response during infection. Alternatively, this model can be used for other pathogens than *Mm* to investigate their interaction with the autophagic machinery.

Quantification of intracellular structures containing *Mm* in early granulomas

In **chapter 2** transmission electron microscopy was performed on early granuloma structures to quantify intracellular structures sequestering bacteria. It was confirmed that at this stage the bacteria resided in different cell types and that they could occur in the extracellular matrix. We quantified the number of intracellular bacteria residing individually in phagosomes, the cytoplasm, autophagic vacuoles, or lysosomes, or residing in aggregates or acidic aggregates. Only a very small fraction (~0.4%) of bacteria was found inside an initial autophagic vacuole with a double membrane, which is most likely due to the highly transient nature of these structures. These autophagosomes generally contain a single bacterium. The fraction of bacteria in degradative autophagic vacuoles is considerably larger (~4.5%). Another population of bacteria resides in phagosomal compartments and this fraction of bacteria (~11%) has been taken up most recently from the extracellular space or has succeeded in blocking lysosomal fusion. For *Mm* it has been shown in cell cultures that they are able to escape the phagosomal compartment, which most likely explains the ~13% of bacteria residing freely in the cytoplasm. This fraction of bacteria is an obvious target for autophagy. These data were confirmed in larvae in chapter 4.

Macrophage and neutrophil dynamics and function during the course of a *Mm* infection

Macrophages and neutrophils contribute strongly to the host defence against intracellular pathogens, including *Mm* (Eum et al., 2010; Yang et al., 2012; Srivastava et al., 2014). These phagocytic cells are the first responders against invading mycobacteria and their specific dynamic interaction with the pathogen is to a large extent uncomprehended (Srivastava et al., 2014; Cronan and Tobin, 2014). We used the tail fin infection model to study the complex interactions of macrophages and neutrophils with each other and *Mm* during the course of an infection using confocal imaging in **chapter 3**. We show that initially both macrophages and neutrophils are recruited to the infection site. Unlike previously reported for systemic infection models, we observed that neutrophils are efficient in phagocytosis of *Mm* and that they also play a role in the dissemination of

Mm in the host, similarly to macrophages Actually, at the initial stages of infection, neutrophils were observed to have even a higher contribution to dissemination of bacteria than macrophages. In addition to phagocytosis of *Mm* by neutrophils, we have also observed their association with unphagocytized bacteria. This type of interaction of neutrophils with the pathogen (or with infected macrophages) occurs for a few minutes without engulfment of the bacteria. We observed neutrophils undergoing netosis when the bacterial aggregate was too large for phagocytosis.

The macrophages appear to play a major role in efferocytosis, a process that is defined as phagocytosis of dead cells, in this case containing bacterial content. As a result, during the course of infection large bacterial aggregates accumulate within macrophages that are unable to contain the *Mm* aggregates and eventually undergo a burst event. Upon such a burst event, other macrophages and neutrophils are recruited that take up the bacterial content. This sequence of events results in the dissemination of *Mm* through the host and an increase in the bacterial burden in the tail fin. Alternatively, macrophages (also neutrophils) containing high bacterial content can be extruded out of the tail fin, and this process is mediated by epithelial cells.

Correlating cellular dynamics and ultrastructure

Visualizing the interactions between the phagocytic cells and *Mm* is complicated by the highly dynamic nature of simultaneous intercellular and intracellular responses. To visualize intercellular interactions time-lapse imaging was performed using confocal microscopy and for the visualization of intracellular structures serial block face scanning electron microscopy (SBF-SEM) was performed on the same samples in **chapter 3**. We used SBF-SEM to image the region of interest in the infected tail fin in 3D at EM resolution. The alignment of the 3D EM images with the images obtained by confocal microscopy was performed using the localization of the bacteria. After alignment the fluorescently labelled macrophages and neutrophils that had been observed in the confocal images were identified in the EM images. Using this approach the EM images of the infected macrophages and neutrophils could not only be correlated with the confocal images but the dynamic behaviour of these cells in the previous hours was known as well.

Although mycobacteria are notorious for their ability to block apoptosis of their host cell (Repasy et al., 2013), our EM images showed macrophages containing a large bacterial content showing early apoptotic morphology with clear chromatin condensation in the nucleus. The confocal images show that this cell had phagocytized a large aggregate of bacteria ~ 30 minutes earlier. One macrophage appeared in the EM

images to contain bacteria in a single compartment together with dead cell remains, as a result of efferocytosis. This cell showed no sign of cell death, which was surprising since the confocal images show that this macrophage phagocytized the aggregate ~1.5 hour earlier.

Based on light microscopy observations, the rapid signal disappearance of neutrophils was previously suggested to be a characteristic of apoptotic cell death (Loynes et al., 2010). However, based on our correlated light and EM images, we suggest that the type of cell death characterized by a rapid disappearance of the fluorescent signal (<1 minute) is a form of necrotic cell death. Interestingly, necrotic cell death appears to be very efficient in protein denaturation as observed for fluorescent proteins, probably as a result of fusion of lysosomal compartments with the cytoplasm and the release of abundant peroxides. One necrotic neutrophil we observed in our EM images showed a round nucleus and an irregularly shaped plasma membrane and no apoptotic features. In the confocal images this neutrophil showed a compacted bacterial content and the disappearance of the fluorescent signal was observed within a time period of 1 min, approximately 30 minutes before fixation. Finally, a neutrophil was observed in the EM images that instead of phagocytosis was undergoing netosis, a process previously observed in cell culture studies in which neutrophils selectively release extracellular traps in response to large pathogens (Francis et al., 2014). In the confocal time-lapse images this neutrophil was observed to be interacting with a large aggregate of *Mm,* which had previously been sequestered by another neutrophil, over the last 30 min before fixation. In future studies it will be interesting to investigate how these mechanisms are regulated and initiated and which cell death mechanism reflects the most adequate response against mycobacterial infections.

Additionally, in the BF-SEM images we observed *Mm* infected epithelial cells in the process of undergoing extrusion. These cells did not show a fluorescent signal associated with macrophages or neutrophils. Instead, using the 3D information provided by this method, we could observe that the bacterial aggregate was entirely engulfed by an epithelial cell. The process of extrusion by epithelial cells in lungs is still unexplored. Since TB infection is spread through the air and typically encounters the lungs of humans, extrusion of bacterial content via the lung epithelium might have an important role in the innate immune defence against mycobacterial infection. On the other hand, extrusion may be advantageous to the mycobacteria, since after extrusion they still reside inside epithelial cells, thereby avoiding recognition and the subsequent inflammatory response. Further studies could shed a light on the contribution of extrusion to the progression of infection within the host as well as the dissemination of mycobacteria from human to human.

Mm early granuloma development and ultrastructural analysis in MyD88-deficient zebrafish larvae

Myd88-mediated signalling plays an important role during *Mm* infection (van der Vaart et al., 2014; Cambier et al., 2014). The early granuloma development and its ultrastructure in MyD88-deficient mutant larvae were investigated by both light and electron microscopy using the tail fin infection model in **chapter 4**. The mutants showed an increased bacterial burden, which is consistent with previous studies in Myd88-deficient larvae using other infection models (van der Vaart et al., 2013). Additionally, a clearly different phenotype of infection was observed in the tail fin of the mutant compared to the wild type larvae. The mutant showed more compacted growth of *Mm* in large aggregates at the site of infection. Furthermore, a lower number of leukocytes were observed at the site of infection compared to wild type. This was most likely due to a reduced recruitment towards the pathogen in *myd88*$^{-/-}$ larvae, and not to increased cell death because less TUNEL-positive cells were found in the mutant. However, the recruitment of leukocytes towards *Mm* infection is not dependent on *myd88*-mediated signalling at the initial stages of infection, as shown in *Mm* infection in the hindbrain. Apparently, there is a difference in MyD88 dependency between the initial and the long-term leukocyte response to *Mm* infection. The long term recruitment has been shown to be dependent on pro-inflammatory mediators like mmp9, TNF and other cytokine signalling, while the initial rapid recruitment of leukocytes towards *Mm* is not MyD88-dependent (Cambier et al., 2014).

TEM images of the infection sites in wild type and mutant larvae revealed that the majority of bacteria were located extracellularly in the mutant. This extracellular growth may be due to the lower level of recruitment of phagocytic cells to the site of infection. In other experimental approaches in which the immune system is compromised, for example knockdown of TNFα, increased extra cellular growth of *Mm* was observed as well (Roca and Ramakrishnan, 2013). Additionally, we studied the intracellular bacteria that resided in the immune cells of the mutant and the wild type. We already showed in chapter 2 that the largest fraction of *Mm* in wild type larvae was observed in acidic aggregates. Interestingly, a distinct difference was observed in the nature of compartments in which intracellular *Mm* was present in the mutant larvae. In mutant larvae a much smaller fraction was found in these acidic aggregates and a larger fraction in non-acidic aggregates and phagosomal compartments. It seems that acidification of these larger aggregates is highly MyD88 dependent. Alternatively, the differences could be explained by the presence of *Mm* in different cell types than leukocytes in the mutant.

Conclusion

In this thesis the zebrafish tail fin infection model is presented, which enables the study of a complex immune response towards (myco)bacterial infection using a combination of light and electron microscopy. The induction of autophagy upon a mycobacterial infection as an important innate immune response was visualized using correlative light and electron microscopy. Studying the role of leukocyte dynamics and function during the course of infection provided new insights into the complex host-pathogen interactions. Using a *myd88* mutant zebrafish line it was shown that the recruitment of leukocytes towards the site of infection and subsequent phagocytosis of bacteria is dependent on MyD88-mediated signaling. With the advancement of medical translational studies using zebrafish disease models, the tail fin infection model may provide new opportunities to develop novel therapies against pathogenic infections like tuberculosis.

References

Berg, R.D., and L. Ramakrishnan. 2012. Insights into tuberculosis from the zebrafish model. *Trends in Molecular Medicine*. 18:689–690. doi:10.1016/j.molmed.2012.10.002.

Bradfute, S.B., E.F. Castillo, J. Arko-Mensah, S. Chauhan, S. Jiang, M. Mandell, and V. Deretic. 2013. Autophagy as an immune effector against tuberculosis. *Curr. Opin. Microbiol.* 16:355–365. doi:10.1016/j.mib.2013.05.003.

Cambier, C.J., K.K. Takaki, R.P. Larson, R.E. Hernandez, D.M. Tobin, K.B. Urdahl, C.L. Cosma, and L. Ramakrishnan. 2014. Mycobacteria manipulate macrophage recruitment through coordinated use of membrane lipids. *Nature*. 505:218–222. doi:10.1038/nature12799.

Cronan, M.R., and D.M. Tobin. 2014. Fit for consumption: zebrafish as a model for tuberculosis. *Dis Model Mech*. 7:777–784. doi:10.1242/dmm.016089.

Eskelinen, E.-L. 2008. New insights into the mechanisms of macroautophagy in mammalian cells. *Int Rev Cell Mol Biol*. 266:207–247. doi:10.1016/S1937-6448(07)66005-5.

Eum, S.-Y., J.-H. Kong, M.-S. Hong, Y.-J. Lee, J.-H. Kim, S.-H. Hwang, S.-N. Cho, L.E. Via, and C.E. Barry. 2010. Neutrophils are the predominant infected phagocytic cells in the airways of patients with active pulmonary TB. *Chest*. 137:122–128. doi:10.1378/chest.09-0903.

Francis, R.J., R.E. Butler, and G.R. Stewart. 2014. Mycobacterium tuberculosis ESAT-6 is a leukocidin causing Ca2+ influx, necrosis and neutrophil extracellular trap formation. *Cell Death Dis*. 5:e1474. doi:10.1038/cddis.2014.394.

Gay, N.J., M. Gangloff, and L.A.J. O'Neill. 2011. What the Myddosome structure tells us about the initiation of innate immunity. *Trends in Immunology*. 32:104–109. doi:10.1016/j.it.2010.12.005.

Kabeya, Y., N. Mizushima, T. Ueno, A. Yamamoto, T. Kirisako, T. Noda, E. Kominami, Y. Ohsumi, and T. Yoshimori. 2000. LC3, a mammalian homologue of yeast Apg8p, is localized in autophagosome membranes after processing. *The EMBO Journal*. 19:5720–5728. doi:10.1093/emboj/19.21.5720.

Kimmel, C.B., W.W. Ballard, S.R. Kimmel, B. Ullmann, and T.F. Schilling. 1995. Stages of embryonic development of the zebrafish. *Dev. Dyn.* 203:253–310. doi:10.1002/aja.1002030302.

Klionsky, D.J., F.C. Abdalla, H. Abeliovich, R.T. Abraham, A. Acevedo-Arozena, K. Adeli, L. Agholme, M. Agnello, P. Agostinis, J.A. Aguirre-Ghiso, H.J. Ahn, O. Ait-Mohamed, S. Ait-Si-Ali, T. Akematsu, S. Akira, H.M. Al-Younes, M.A. Al-Zeer, M.L. Albert, R.L. Albin, J. Alegre-Abarrategui, M.F. Aleo, M. Alirezaei, A. Almasan, M. Almonte-Becerril, A. Amano, R. Amaravadi, S. Amarnath, A.O. Amer, N. Andrieu-Abadie, V. Anantharam, D.K. Ann, S. Anoopkumar-Dukie, H. Aoki, N. Apostolova, G. Arancia, J.P. Aris, K. Asanuma, N.Y.O. Asare, H. Ashida, V. Askanas, D.S. Askew, P. Auberger, M. Baba, S.K. Backues, E.H. Baehrecke, B.A. Bahr, X.-Y. Bai, Y. Bailly, R. Baiocchi, G. Baldini, W. Balduini, A. Ballabio, B.A. Bamber, E.T.W. Bampton, G. Bánhegyi, C.R. Bartholomew, D.C. Bassham, R.C. Bast, H. Batoko, B.-H. Bay, I. Beau, D.M. Béchet, T.J. Begley, C. Behl, C. Behrends, S. Bekri, B. Bellaire, L.J. Bendall, L. Benetti, L. Berliocchi, H. Bernardi, F. Bernassola, S. Besteiro, I. Bhatia-Kissova, X. Bi, M. Biard-Piechaczyk, J.S. Blum, L.H. Boise, P. Bonaldo, D.L. Boone, B.C. Bornhauser, K.R. Bortoluci, I. Bossis, F. Bost, J.-P. Bourquin, P. Boya, M. Boyer-Guittaut, P.V. Bozhkov, N.R. Brady, C. Brancolini, A. Brech, J.E. Brenman, A. Brennand, E.H. Bresnick, P. Brest, D. Bridges, M.L. Bristol, P.S. Brookes, et al. 2012. Guidelines for the use and interpretation of assays for monitoring autophagy. *autophagy*. 8:445–544.

Koning, R.I., F.G. Faas, M. Boonekamp, B. de Visser, J. Janse, J.C. Wiegant, A. de Breij, J. Willemse, P.H. Nibbering, H.J. Tanke, and A.J. Koster. 2014. MAVIS: an integrated system for live microscopy and vitrification. *Ultramicroscopy*. 143:67–76. doi:10.1016/j.ultramic.2013.10.007.

Loynes, C.A., J.S. Martin, A. Robertson, D.M.I. Trushell, P.W. Ingham, M.K.B. Whyte, and S.A. Renshaw. 2010. Pivotal Advance: Pharmacological manipulation of inflammation resolution during spontaneously resolving tissue neutrophilia in the zebrafish. *J. Leukoc. Biol.* 87:203–212. doi:10.1189/jlb.0409255.

Philips, J.A., and J.D. Ernst. 2012. Tuberculosis pathogenesis and immunity. *Annu Rev Pathol*. 7:353–384. doi:10.1146/annurev-pathol-011811-132458.

Renshaw, S.A., C.A. Loynes, D.M.I. Trushell, S. Elworthy, P.W. Ingham, and M.K.B. Whyte. 2006. A transgenic zebrafish model of neutrophilic inflammation. *Blood*. 108:3976–3978. doi:10.1182/blood-2006-05-024075.

Repasy, T., J. Lee, S. Marino, N. Martinez, D.E. Kirschner, G. Hendricks, S. Baker, A.A. Wilson, D.N. Kotton, and H. Kornfeld. 2013. Intracellular bacillary burden reflects a burst size for Mycobacterium tuberculosis in vivo. *PLoS Pathog*. 9:e1003190. doi:10.1371/journal.ppat.1003190.

Roca, F.J., and L. Ramakrishnan. 2013. TNF dually mediates resistance and susceptibility to mycobacteria via mitochondrial reactive oxygen species. *Cell*. 153:521–534. doi:10.1016/j.cell.2013.03.022.

Srivastava, S., J.D. Ernst, and L. Desvignes. 2014. Beyond macrophages: the diversity of mononuclear cells in tuberculosis. *Immunological Reviews*. 262:179–192. doi:10.1111/imr.12217.

Studer, D., B.M. Humbel, and M. Chiquet. 2008. Electron microscopy of high pressure frozen samples: bridging the gap between cellular ultrastructure and atomic resolution. *Histochem. Cell Biol.* 130:877–889. doi:10.1007/s00418-008-0500-1.

van der Vaart, M., J.J. van Soest, H.P. Spaink, and A.H. Meijer. 2013. Functional analysis of a zebrafish myd88 mutant identifies key transcriptional components of the innate immune system. *Dis Model Mech*. 6:841–854. doi:10.1242/dmm.010843.

Yang, C.-T., C.J. Cambier, J.M. Davis, C.J. Hall, P.S. Crosier, and L. Ramakrishnan. 2012. Neutrophils exert protection in the early tuberculous granuloma by oxidative killing of mycobacteria phagocytosed from infected macrophages. *Cell Host and Microbe*. 12:301–312. doi:10.1016/j.chom.2012.07.009.

APPENDIX

SAMENVATTING
CURCULUM VITAE
LIST OF PUBLICATIONS

Samenvatting

De immuunreactie tegen een infectie met (myco)bacteriën bestaat uit een complexe intracellulaire signaaltransductie die leidt tot de activering van effector-moleculen met als doel de pathogeen te elimineren. Daarnaast worden intercellulaire signalen doorgegeven aan andere immuuncellen over de aanwezigheid van de infectie. Om deze activiteiten gericht te bestuderen kan de zebravis als model worden gebruikt. In dit proefschrift is onderzoek beschreven dat erop gericht is om deze beide reacties van het immuunsysteem tegelijkertijd in beeld te brengen en te bestuderen.

In dit onderzoek hebben we een nieuw zebravis-infectiemodel ontwikkeld, waarmee intracellulaire structuren met licht- en elektronenmicroscopie gevisualiseerd kunnen worden **(hoofdstuk 2)**. In dit model worden pathogenen direct geïnjecteerd in de staartvin van een zebravis larve, waardoor hier een lokale infectie ontstaat. In het geval van een infectie met Mycobacterium marinum (Mm) leidt dit tot de lokale vorming van enkele vroege granuloma-structuren, die kenmerkend zijn voor infecties van deze pathogeen. De staartvin is zeer geschikt voor het in beeld brengen van de infectie met hoge-resolutie lichtmicroscopie (LM), omdat het weefsel uit slechts enkele cellagen bestaat en de geïnfecteerde cellen zich op een relatief korte afstand van het objectief van de microscoop bevinden. De relatief lage hoeveelheid diffuus licht verbetert het contrast en de resolutie van de beelden gemaakt in dit weefsel. Voor transmissie-elektronenmicroscopie (TEM) heeft het lokale-infectiemodel het grote voordeel dat slechts een kleine hoeveelheid weefsel onderzocht hoeft te worden om het geïnfecteerde gebied in beeld te brengen.

Wanneer we larven in beeld brengen met behulp van LM, en ze daarna fixeren voor TEM, kunnen de beelden die worden verkregen door middel van deze twee verschillende microscopietechnieken worden gecorreleerd. In onze experimenten werd deze correlatie uitgevoerd op basis van de lokalisatie van de bacteriën, die zichtbaar zijn in lichtmicroscopie-opnames doordat ze fluorescent zijn en op basis van hun morfologie makkelijk kunnen worden herkend in de TEM beelden. Het visualiseren van intercellulaire interacties door middel van tijdsreeks-opnames (time-lapsing) werd uitgevoerd met behulp van confocale microscopie **(hoofdstuk 3)**. De visualisatie van intracellulaire structuren werd op dezelfde monsters uitgevoerd met behulp van serial block face scanning elektronenmicroscopie (SBF-SEM) in hoofdstuk 3. We gebruikten SBF-SEM om de regio van onze interesse in de geïnfecteerde staartvin in 3D te visualiseren met hoge resolutie. Het vergelijken van de zelfde beeldregio's in de EM 3D foto's en beelden verkregen door confocale

microscopie werden ook gecorreleerd door de locatie van de bacteriën als referentiepunt te gebruiken. Na dit proces werden de fluorescente macrofagen en neutrofielen die waargenomen waren in de confocale beelden teruggezocht in de EM afbeeldingen. Met deze aanpak konden niet alleen de EM beelden gecorreleerd worden met de confocale beelden, maar kon ook het dynamisch gedrag van deze zelfde individuele leukocyten in de voorafgaande uren bepaald worden.

Autofagie is een proces dat letterlijk vertaald "zelfconsumering" betekent. In dit proces, dat in vrijwel alle cellen van hogere organismen voorkomt, worden beschadigde organellen of intact celmateriaal afgebroken, om brandstof vrij te maken in tijden van een te lage energie-aanvoer. Bij autofagie wordt een deel van het cytoplasma omsloten door een dubbele membraan, en deze structuur wordt een autofagosoom genoemd als het helemaal gesloten is. De autofagosomen die op deze manier ontstaan smelten vervolgens samen met lysosomen, die het lytische vermogen bezitten om de inhoud te verteren. In samengesmolten vorm worden deze blaasjes autolysosomen genoemd. Aanvankelijk beschouwde men dit proces alleen als een afbraakmechanisme van de cel, maar recent onderzoek ondersteunt de hypothese dat autofagie een belangrijke rol speelt in veel ziektebeelden zoals kanker, neurodegeneratieve aandoeningen en in de afweer tegen bacteriële infecties.

In dit proefschrift is autofagie tegen Mm onderzocht met behulp van LM en TEM door gebruik te maken van transgene zebravis larven, waarin een GFP-Lc3 fusie-eiwit tot expressie is gebracht **(hoofdstuk 2)**. Lc3 is een ubiquitine-achtig eiwit dat betrokken is bij de opbouw van autofagosomen en vaak wordt gebruikt als een marker voor autofagocytotische compartimenten. Twee soorten GFP-Lc3-positieve structuren werden geobserveerd na de infectie met Mm in de staartvin. Ten eerste, talrijke relatief kleine blaasjes (~1 micrometer) werden waargenomen die geen bacteriën bevatten. Deze kleine blaasjes bleken zeer dynamisch en kunnen samensmelten met andere compartimenten die wel bacteriën bevatten. Correlatie van licht- en elektronenmicroscopieplaatjes hebben laten zien dat deze kleine GFP-Lc3-positieve blaasjes in de nabijheid van bacteriën inderdaad de morfologische kenmerken hebben van een autofagosoom. Ten tweede waren er, in mindere mate, grotere GFP-Lc3 blaasjes aanwezig (~3 micrometer) die vaak bacteriën geheel omsloten hadden. De autofagosomale aard van deze blaasjes werd ondersteund door correlatieve licht- en elektronenmicroscopie plaatjes waaruit bleek dat de grotere GFP-Lc3 blaasje de bacteriën geheel hadden omsloten en daarnaast de morfologische kenmerken van een autolysosoom hadden. Het voordeel van het bestuderen van het infectieproces in een diermodel, in vergelijking met in vitro modellen, werd duidelijk toen deze verschillende autofagie reacties werden

vergeleken tussen immuuncellen en andere celtypen. De grotere bacterie-bevattende GFP-Lc3 positieve blaasje werden vaker waargenomen in leukocyten (witte bloedcellen) dan in andere celtypes (hoofdzakelijk epitheelcellen in de staartvin).

Over het algemeen komen bacteriën in een cel terecht door fagocytose, een proces waarin de celmembraan zich om de pathogeen stulpt en waarin na het insluiten de pathogeen zich omgeven door de membraan van fagosoom in een ruimte binnen in de cel bevindt. Na het samensmelten van het fagosoom met lysosomen kan de inhoud hiervan afgebroken worden. Bepaalde bacteriën, waaronder Mm, kunnen deze samensmelting voorkomen en ontsnappen uit de het fagosoom naar het cytoplasma van de cel. De Mm die ontsnapt naar het cytoplasma kan vervolgens opgeruimd worden door autofagie. Door gebruik te maken van het staartvin-infectiemodel, waren we in staat om voor het eerst door middel van TEM de bacteriën-bevattende intracellulaire structuren te kwantificeren in een vroeg granuloom **(hoofdstuk 2)**. Er werd bevestigd dat in dit stadium de bacteriën verbleven in verschillende celtypes en dat ze daarnaast aangetroffen kunnen worden in de extracellulaire matrix. We hebben het aantal intracellulaire bacteriën gekwantificeerd die zich individueel in de fagosomen, het cytoplasma, autofagocytische blaasjes of lysosomen bevonden, of zich als een groep bacteriën in aggregaten of zure aggregaten bevonden. Slechts een zeer kleine fractie (~0,4%) bacteriën werd waargenomen in een autofagosoom met een dubbele membraan, hetgeen waarschijnlijk te wijten is aan de zeer korte levensduur van deze structuren. De fractie bacteriën in autolysosomen was aanzienlijk groter (~4,5%). Een andere populatie van bacteriën bevond zich in fagosomen en deze fractie van de bacteriën (~11%) is óf zeer recent opgenomen uit de extracellulaire ruimte óf de bacteriën zijn erin geslaagd de lysosomale fusie te voorkomen. Voor Mm is in celculturen aangetoond dat de bacteriën in staat zijn uit fagosomen te ontsnappen, wat waarschijnlijk de ~13% vrije bacteriën in het cytoplasma verklaart. Deze fractie van bacteriën is een voor de hand liggend doelwit voor autofagie.

Macrofagen en neutrofielen dragen sterk bij aan de afweer tegen intracellulaire pathogenen, waaronder Mm. Deze fagocytotische cellen zijn de eerste strijders tegen binnendringende mycobacteriën en hun specifieke dynamische interacties met de pathogeen zijn grotendeels onbekend. We hebben het staartvin-infectiemodel gebruikt om de complexe interacties van macrofagen en neutrofielen onderling en met Mm te bestuderen tijdens een infectie met behulp van confocale microscopie en correlatieve licht- en elektronenmicroscopie **(hoofdstuk 3)**. We zien dat in het begin van het infectieproces zowel macrofagen

als neutrofielen worden aangetrokken naar de locatie van de infectie. Anders dan eerder gerapporteerd in systemische-infectiemodellen, vonden we dat neutrofielen efficiënt zijn in het fagocyteren van Mm en dat ze met name in de initiële fase van de infectie verantwoordelijk zijn voor de verspreiding van Mm in de gastheer. Naast het fagocyteren van Mm door neutrofielen, hebben we ook associaties van neutrofielen met niet-gefagocyteerde bacteriën waargenomen. Dit soort interacties van neutrofielen met de pathogeen (of geïnfecteerde macrofagen) traden op gedurende enkele minuten zonder opname van bacteriën. We hebben neutrofielen waargenomen die dood gaan door netosis, een verdedigingsmechanisme waarbij DNA en antimicrobiële stoffen op de pathogeen vrijkomen, in gevallen waarin de bacteriële aggregaten waarschijnlijk te groot waren voor fagocytose. De macrofagen lijken een belangrijke rol te spelen in continu plaatsvindende efferocytosis, een proces dat wordt gedefinieerd als fagocytose van dode cellen met bacteriële inhoud. Hierdoor resulteert de infectie in de ophoping van bacteriën in macrofagen als grote aggregaten, waardoor de macrofagen uiteindelijk open barsten. Bij een dergelijke uitbarsting worden andere macrofagen en neutrofielen aangetrokken die de bacteriële inhoud opnemen. Deze opeenvolging van gebeurtenissen resulteert in de verspreiding van Mm door de gastheer en een toename in de bacteriële groei in de staartvin. Een oplossing van de gastheer om van de infectie af te komen is om de macrofagen (en neutrofielen) met veel bacteriën te extruderen uit de staartvin, en dit proces wordt gefaciliteerd door epitheelcellen.

Door Myd88 aangestuurde signaling speelt een belangrijke rol tijdens Mm infectie. In **hoofdstuk 4** zijn de vroege granuloomontwikkeling en de ultrastructuur van deze structuren in het staartvin-infectiemodel onderzocht in MyD88-deficiënte larven met behulp van zowel licht- als elektronenmicroscopie. De mutanten vertoonden een snellere toename van de bacteriële infectie, wat in overeenstemming is met eerdere studies die gedaan zijn met andere Mm infectiemodellen in larven met een Myd88 deficiëntie. Daarnaast observeerden wij een duidelijk verschillend fenotype van de infectie in de staartvin van de mutant in vergelijking tot de wild type larven. De Myd88-deficiënte larven vertoonden een compactere groei van Mm in grote extracellulaire aggregaten op de plaats van de infectie in vergelijking met de wild-types. Verder werd er een lager aantal leukocyten waargenomen op de plaats van infectie in vergelijking met de wild type. Dit is waarschijnlijk te wijten aan een verminderde rekrutering van leukocyten naar de pathogeen in MyD88-/- larven door defecte signaling, en niet aan verhoogde celdood, aangezien er minder TUNEL-positieve cellen werden gevonden in de mutant.

In dit proefschrift wordt het zebravis staartvin-infectiemodel gepresenteerd, dat het onderzoek van een complexe immuunrespons tegen (myco)bacteriële infectie met behulp van een combinatie van licht- en elektronenmicroscopie mogelijk maakt. De inductie van autofagie bij een mycobacteriële infectie als een belangrijke aangeboren immuunrespons werd gevisualiseerd met deze technologie. Het bestuderen van de rol van de functie en dynamiek van leukocyten in de loop van de infectie brengt ons nieuwe inzichten in de complexe interacties tussen een gastheer en een pathogeen. Binnen de vooruitgang in medisch translationeel onderzoek met behulp van zebravis ziektemodellen kan het gebruik van het staartvin-infectiemodel bijdragen aan het ontwikkelen van nieuwe therapieën tegen pathogene infecties zoals tuberculose.v

Curriculum vitae

Rohola Hosseini was born on August 1st, 1983 in Qandahar, Afghanistan. After graduating from highschool in 2002 (Carolus Clusius College, Zwolle), he started a year later the study Life Science and Technology at TU Delft and Leiden University. During his bachelor and master education he became very fascinated by different imaging techniques that allow studying the intracellular cell dynamics and protein structures. He finalized his study, specializing in structural biology, with an internship in the group of Biophysical Structural Chemistry in Leiden. During his internship he developed methods for protein nanocrystallization that are suitable for electron diffraction. After completing his Master's program in October 2010, he joined the Institute of Biology (University of Leiden) as a PhD student. In his research project, he focused on the development of methods for the visualization of host-pathogen interactions in zebrafish larvae that allowed using both light and electron microscopy. Subsequently, he applied these methods to study intracellular and intercellular processes during the course of a mycobacterial infection. He is currently working as a postdoctoral fellow in the Institute of Biology on solvent tolerance in Pseudomonas species.

List of publications

Rohola Hosseini, Gerda E. M. Lamers, Zlatan Hodzic, Annemarie H. Meijer, Marcel J. M. Schaaf and Herman P. Spaink, Correlative Light and Electron Microscopy Imaging of Autophagy in a Zebrafish Infection Model, Autophagy 2014, Volume 11, Issue 10, 130-143

Michiel van der Vaart, Cornelis J. Korbee, Gerda E.M. Lamers, Anouk C. Tengeler, Rohola Hosseini, Mariëlle C. Haks, Tom H.M. Ottenhoff, Herman P. Spaink and Annemarie H. Meijer, The DNA Damage-Regulated Autophagy Modulator DRAM1 Links Mycobacterial Recognition via TLR-MYD88 to Autophagic Defense, Cell Host & Microbe 2014, Volume 15, Issue 6 , 753 – 767

Igor Nederlof, Rohola Hosseini, Dilyana Georgieva, Jinghui Luo, Dianfan Li, and Jan Pieter Abrahams, A Straightforward and Robust Method for Introducing Human Hair as a Nucleant into High Throughput Crystallization Trials, Crystal Growth & Design 2011, Volume 11, Issue 4, 1170-1176